Modelling the dynamic response of overhead line conductors subjected to shock-induced ice shedding

by

Farshad Mirshafiei

August 2010

Department of Civil Engineering and Applied Mechanics
McGill University, Montreal

A Thesis submitted to the Faculty of Graduate Studies and Research in partial fulfillment of the requirements of the degree of Master of Engineering

“Life is like riding a bicycle. To keep your balance you must keep moving.”

Albert Einstein

In a letter to his son Eduard, 1930

Abstract

In cold climate regions, overhead transmission lines are prone to atmospheric icing which can be a source of several dynamic effects. The work presented in this study is concerned with accurate numerical modelling of the propagation or progression of ice shedding phenomena following an initial trigger such as a controlled shock load applied locally with a cable de-icing device, or uncontrolled shocks due to cable rupture or random ice dropping.

An improved ice failure model for glaze ice cylindrical deposits on a stranded wire is proposed to study ice shedding effects. The model is verified with the results of forced ice shedding experiments on a reduced-scale single-span model tested by Kálmán (2007) at CIGELE Laboratory of Université du Québec at Chicoutimi (UQAC). The physical model is a 4 m span of a 4.1 mm diameter flexible stainless cable with an initial sag-to-span ratio of 6%. In the present study, the ice deposit is assumed elastic-plastic and the failure criterion is based on maximum normal strains; the numerical results are in better agreement with the experimental data as compared to the previous study by Kálmán (2007) who assumed a maximum normal stress failure criterion. The challenge is to predict not only the fracture of the ice deposits but also whether the fractured deposits will remain attached to the conductor or will fall off. In the tests, iced spans (loaded with different ice thicknesses) were subjected to a concentrated shock load applied at the mid span. Commercial software ADINA is used to simulate the nonlinear dynamic response of the iced cable to the shock load and subsequent ice-shedding transient effects.

This new iced cable model and failure criterion is implemented to conduct numerical simulations of real-scale single spans subjected to shock loads, and the results are compared with previous work by Kálmán (2007).

Following the improved performance of the new ice failure model, it has been applied to the case study of a Hydro-Québec 120 kV two-circuit line section that failed during an ice storm event in the spring of 1997. This line has suffered two conductor ruptures that initiated the subsequent failure of two suspension structures. A nonlinear dynamic analysis is performed which considers ice-shedding effects following the conductor ruptures. The results are compared with those of Lapointe (2003) who considered only conductor rupture effects on the fully iced line section.

Sommaire

En régions froides, les lignes aériennes de transport sont exposées au givrage atmosphérique qui peut devenir la source de plusieurs effets dynamiques. Cette étude porte sur la modélisation numérique de la progression des phénomènes de délestage de glace des conducteurs de ligne suivant l'application d'un choc mécanique local généré par un dispositif de dégivrage de câble, ou l'effet des chocs non contrôlés dus à la rupture de câbles ou au délestage aléatoire naturel de la glace.

Un modèle amélioré pour simuler la rupture du manchon cylindrique de glace accumulé sur un câble est proposé dans cette étude et vérifié à l'aide de résultats expérimentaux obtenus par Kálmán (2007) sur un modèle réduit d'une portée unique au laboratoire CIGELE de l'Université du Québec à Chicoutimi (UQAC). Le modèle physique a une portée de 4 m et est composé d'un câble en acier inoxydable flexible de 4.1 mm de diamètre avec un rapport flèche/portée de 6%. Dans le modèle proposé, le dépôt de glace est supposé élastique-plastique et le critère de rupture est basé sur les déformations normales; les résultats des simulations numériques sont en meilleur accord avec les données expérimentales que celles de l'étude précédente de Kálmán (2007) qui utilisait un critère de rupture basé sur les contraintes normales. Le défi des simulations numériques du délestage de glace est de prévoir non seulement la fissuration des dépôts de glace mais également si leur détachement est complet du conducteur. Lors des essais, des portées de câble glacé (chargées avec différentes épaisseurs de glace) ont été soumises à un choc appliqué à mi-portée. L'étude utilise le logiciel commercial ADINA

AUI 8.5 pour simuler la réponse dynamique non linéaire du câble glacé suite au choc appliqué.

Le nouveau critère proposé pour la rupture du dépôt de glace est ensuite utilisé pour simuler la réponse de portées uniques à l'échelle réelle soumises à des chocs appliqués à mi-portée, et les résultats sont comparés à ceux de l'étude de Kálmán (2007).

Finalement, le modèle amélioré a été appliqué à l'étude du cas d'une section de ligne biterne à 120 kV d'Hydro-Québec qui a été endommagée lors d'une tempête de verglas en 1997. Cette ligne de ligne a subi deux ruptures de conducteur qui ont causé l'effondrement de deux pylônes de suspension. Cet événement avait été déjà été modélisé par Lapointe (2003) mais sans la possibilité de tenir compte du délestage de glace suite aux chocs de rupture des conducteurs.

Acknowledgments

The author is grateful for the financial support provided by the Fonds québécois de la recherche sur la nature et les technologies (FQRNT) for this study.

There are many people who have helped me throughout the course of my graduate studies. I would like to thank my advisor Professor Ghyslaine McClure, for her guidance, encouragement and support throughout my graduate career. The opportunities for growth and the excitement of working in our group are deeply appreciated; I am honoured to have had the chance to be part of it. I would also like to thank my co-advisor, Professor Masoud Farzaneh of Université du Québec at Chicoutimi.

Many thanks to my colleague Ali, and my friends who encouraged and helped me during this research program.

My deepest appreciation goes to my family for their sustained encouragements and supports in all and every stage of my life; to my mother, Afsaneh, for her endless love; to my father, Aliakbar, one of the greatest Iranian architects who inspired me to pursue the structural engineering profession; to my brothers, Mehrdad and Farzad, especially my older brother Mehrdad, a true friend, who has had a great influence on my life.

Table of contents

List of Figures

List of Tables

List of symbols

A	cross-sectional area (m^2)
C	viscous damping constant (Ns/m)
d	cable sag at the mid span (m)
E	elastic modulus (Pa)
g	acceleration of gravity (m/s^2)
H	horizontal component of the cable tension (N)
I_t	second moment of area (m4)
l	span length (m)
m, μ	mass per unit length (kg/m)
t	time (s)
T_{ice}	radial ice thickness (m)
T_H	horizontal component of the cable end-tension (N)
r, s, t	element local coordinate axes
X, Y, Z	global coordinate axes
LWC	liquid water content of the air
α	Newmark integration operator parameter
δ	Newmark integration operator parameter
$\varepsilon_{initial}$	cable initial strain
ρ	density (kg/m^3)

ε_p	maximum allowable effective plastic strain
ε_y	yield strain
W	Width (mm)
D	Height (mm)
RIS	rate of ice shedding
ETOL	energy tolerance
DTOL	displacement tolerance
FTOL	force tolerance
c	wave speed (m/s)
t_d	time delay (ms)
Sp	suspension point
T_{max}	peak wire tension (kN)

1. Introduction

1.1 General

In cold climate regions, overhead transmission lines are prone to atmospheric icing. The ice accretions on line conductors can take many shapes (Figure 1.1), densities and have wide-ranging mechanical properties. Ice shedding from conductors may happen naturally, or by intentional melting, by propagation of a shock wave due to impact, or by any other external ice-removal scheme.

A typical transmission line is composed of four major components: Conductors, towers and/or poles, insulators and foundations, as shown schematically in Figure 1.2. In addition, from a mechanical perspective, a transmission line is consisted of a series of line sections that respond independently from each other, as each line section is made of successive spans supported by suspension towers and anchored on a dead-end structure at each extremity. Most of the times, the use of such dead-end structures (also called straining towers) is governed by the characteristics of the terrain or land usage; i.e. a change in the line direction is needed when the geographic profile is mountains or when an obstacle needs to be crossed.

Figure 1.1 Glaze icing on overhead distribution line (source: Brownstown Electrical Supply Co., Inc.)

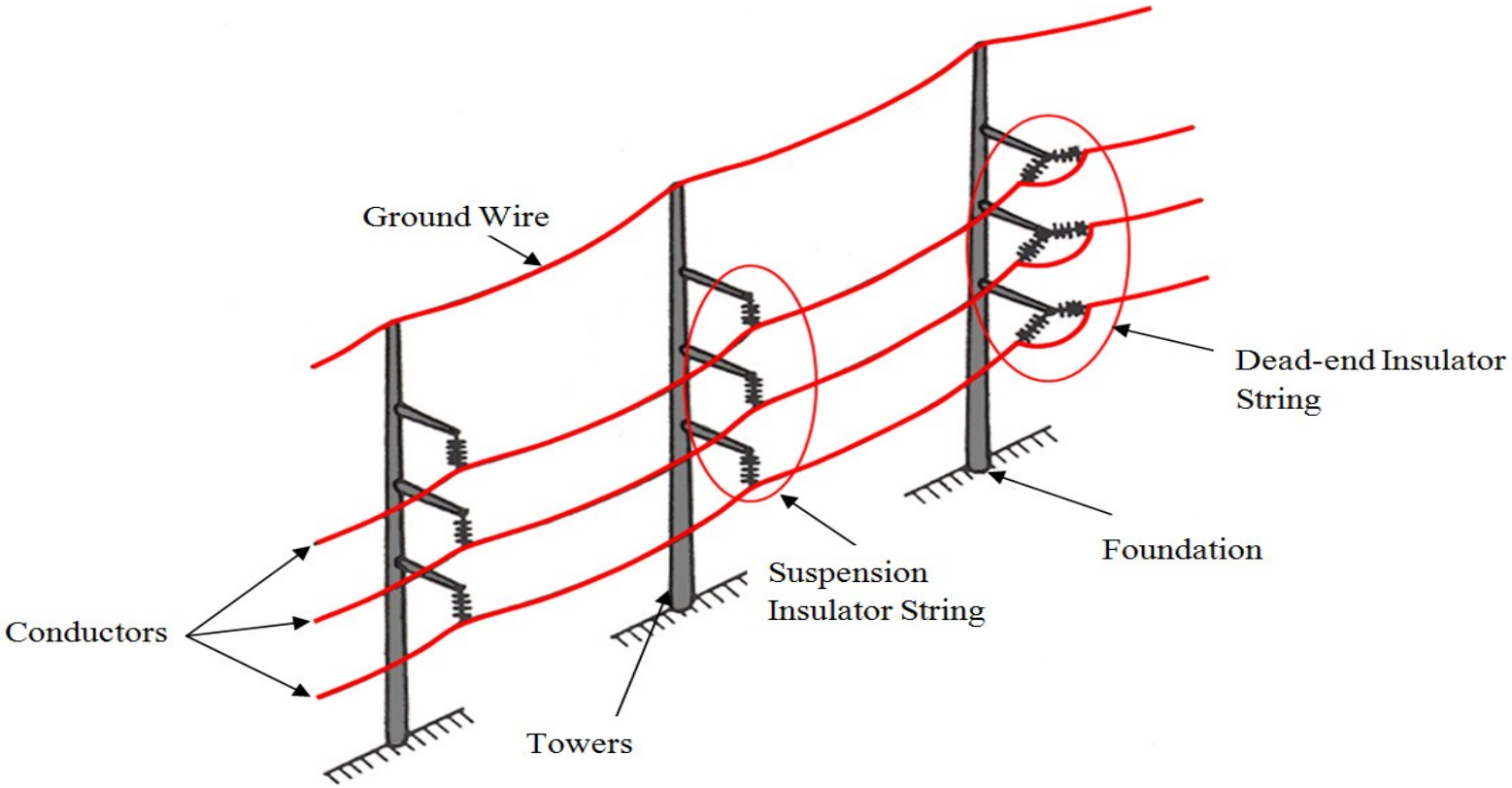

Figure 1.2 Schematic of components of a single-circuit Electric Overhead Transmissions Line System.

(Adapted from McClure and Tinawi (1987))

Atmospheric icing can be the source of several dynamic effects. Although most line design procedures are based on static analysis, more advanced dynamic analysis is necessary to understand and predict the line transient response to complex dynamic loads. The interest of numerical modelling of the effects of ice shedding phenomena is to assess the possible dynamic amplifications of cable tensions in the line, which are eventually transferred to supports, and to check whether the amplitude of the induced motion is within design limits of electrical clearances with the ground or with other conductors.

Another situation for which dynamic effects need to be examined is when a line section is subjected to a sudden component rupture such as conductor rupture. Some of these ruptures, as it was observed in 1998 storm in Québec, Canada (Commission 1999) may lead to cascading failures of transmission line towers. Moreover, when the line is iced the component rupture and ice shedding phenomena could occur at the same time. In all these cases relying on static analysis procedures is not sufficient to assess the response of the line section and account for the interaction of all line components in the section.

Therefore, this study focuses on the dynamic behaviour of iced overhead line subjected to in-span shock loads induced by forced ice shedding. An example where conductor ruptures are simulated is considered in the last part of the study, to investigate whether rupture shocks are sufficient to shed accumulated ice on the conductors.

1.2 Objectives

The goal of this research is to better understand the dynamic behaviour of shock-load-induced ice shedding on overhead lines by implementing a new ice failure criterion. After validation, the new criterion is applied to various single span examples and finally to a real scale transmission line which has suffered two conductor ruptures during an icing event.

The specific research objectives are:

1) To develop a new ice failure criterion which yields more realistic prediction of ice fracture rates and rate of ice shedding than the criterion used in earlier studies by Kálmán (2007), in comparison to experimental results. To implement this criterion in a finite element model of a single span cable.
2) To compare the simulated dynamic response of an iced cable exposed to impact loads with some results measured in reduced-scale laboratory tests conducted by Kálmán (2007) in CIGELE Laboratory of Université du Québec at Chicoutimi.
3) To further validate this new iced cable model and failure criterion with numerical simulations of real-scale spans subjected to shock loads, and compare the results with previous work.
4) To implement the new failure criterion to study ice shedding on a 120 kV line section owned by Hydro-Québec. This line has suffered two conductor ruptures that initiated the subsequent failure of two suspension structures in 1997. A nonlinear dynamic analysis is performed which considers ice-shedding effects following conductor ruptures. This line section had been studied by Lapointe (2003) but had considered only conductor rupture effects.

1.3 Thesis organization

This research is divided into the following chapters:

Chapter 2 introduces different aspects and characteristics of atmospheric icing, and summarizes previous research on numerical modeling of ice shedding and line sections suffered from conductor rupture.

Chapter 3 introduces the new ice failure criterion and an improved ice shedding model of iced cables. Detailed modeling aspects related to static and dynamic parameters are presented in this chapter and the results are compared with the previous work by Kálmán (2007) on a reduced-span physical model of an iced cable.

The new ice failure criterion model is then applied to a single 300-m span of real conductor, and the results are compared to the previous numerical simulation work by Kálmán (2007) in Chapter 4. Also parametric studies leading to the selection of an optimum mesh size for real-scale problems are discussed in this Chapter.

Chapter 5 presents the case study of the 120 kV line section subjected to iced cable ruptures. Ice shedding modeling is also considered in some spans of this line section subjected to instantaneous cable ruptures. Results are compared with previous work by Lapointe (2003) which did not include the possibility of ice shedding.

Although specific discussion and conclusions are presented at the end of each chapter, the general conclusions of this study and suggestions for future work are presented in Chapter 6.

2. Literature review

2.1 Atmospheric icing

Atmospheric icing is a complex phenomenon that comes either from precipitation icing or from in-cloud icing. It may happen at ambient air temperature between -10ºC and 0ºC, or occasionally, at lower temperature under particular conditions. In-cloud icing occurs when super-cooled droplets freeze without delay upon impact on an object exposed to airflow. Precipitation icing can take the form of freezing precipitation and frozen precipitation. Freezing precipitation takes place when any form of precipitation freezes upon impact on or contact with an exposed object. Frozen precipitation is any form of precipitation that reaches the ground in the frozen form (Huschke 1959).

Mainly five types of ice accretion may deposit on structures: glaze, soft rime, hard rime, wet snow, dry snow, and hoar frost (Poots 1996). Glaze ice, which is the focus of this research, forms on exposed objects by the freezing of a thin layer of super-cooled water deposited by rain, drizzle, or fog. It produces the densest form of atmospheric icing and on transmission lines in particular, very large loads are reached within hours (Figure 1.1) (CIGRE 2006).

Ice accretion on transmission lines could lead to several mechanical problems. The gravity loads due to heavy ice accretion on overhead lines coupled with wind on ice loads and also ice shedding from the conductors could be a source of structural damages, failure or even cascading collapse of towers. Ice shedding occurs when accreted ice on the overhead conductors is detached from the cables and falls down.

As discussed previously, ice related load could have severe consequences on transmission lines. Therefore, various mitigation methods (anti-icing and de-icing techniques) are used. The methods that are used after the line is covered by ice are called de-icing techniques. On the other hand, methods that are applied before an ice storm to prevent the formation of ice deposits on the line are called anti-icing techniques. The two most effective de-icing methods are thermal and mechanical ones (Volat *et al.* 2005). One of the mechanical methods developed for line de-icing is based on applying mechanical shocks on iced conductors, taking advantage of the brittle behavior of ice at high strain rates. This method is subject of interest for Chapter 3 of this study. One of these mechanical de-icing devices is called DAC (De-icer Actuated by Cartridge) and is illustrated in Figure 2.1 (Leblond *et al.* 2002 and 2005). This device would be installed under the iced cable and a piston exerts an impact load that generates a transverse wave along the span that fractures the accreted ice and forces it to detach and fall down. It is an interesting device for *ad hoc* intervention on a limited number of spans.

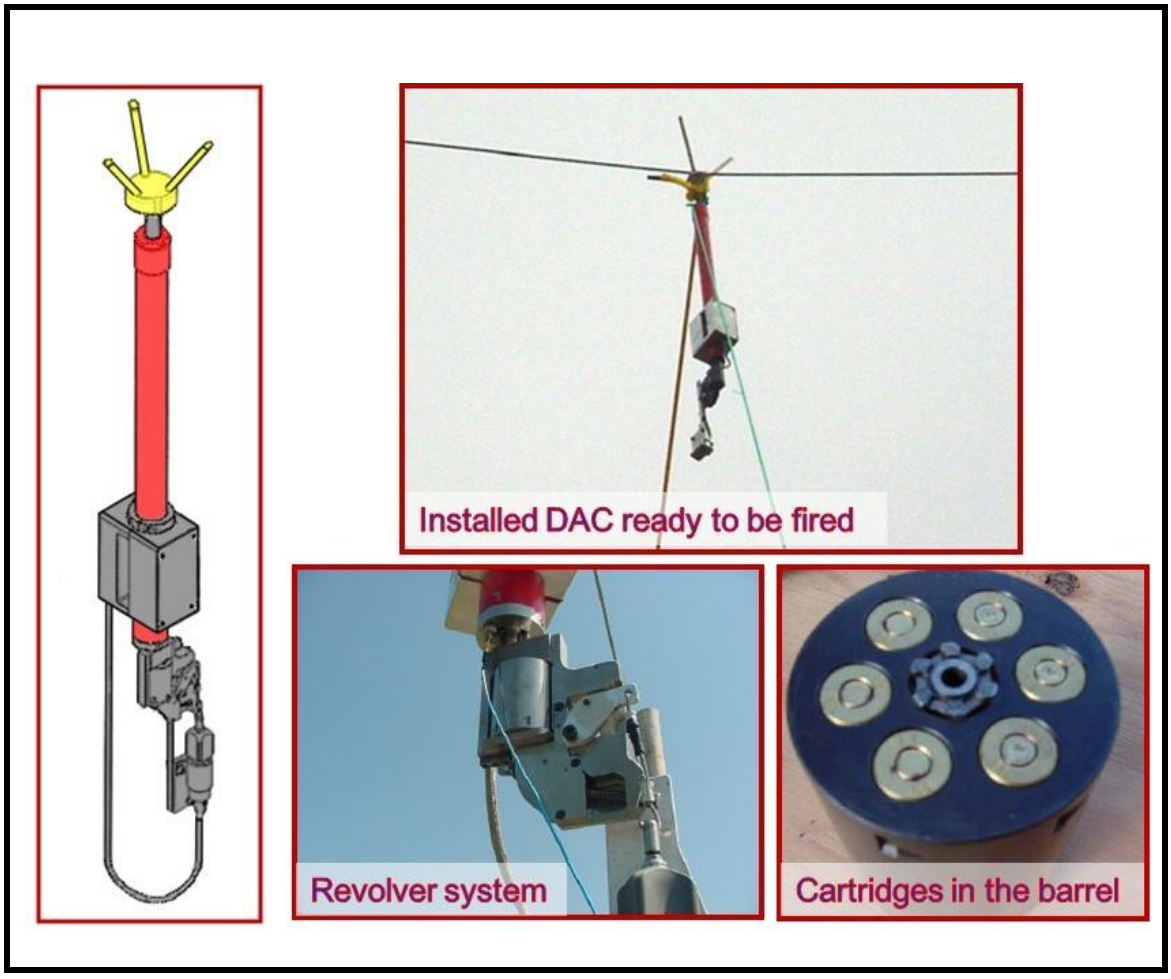

Figure 2.1 Sketch of DAC device (adapted from Leblond *et al.* 2005)

Mechanical properties of atmospheric ice

Relatively few studies on the mechanical properties of atmospheric ice have been reported to date. The mechanical properties of atmospheric ice depend on ambient temperature, load type and magnitude, strain rate, and type and micro-structure of the ice. The type of ice is mainly determined by the meteorological conditions prevailing during ice formation. One of the first studies on the properties of atmospheric icing has been done by Druez *et al.* (1986) who measured the compressive and adhesive strength of glaze ice at various temperatures, wind speeds and strain rates. Their main conclusions

were as follows: 1) Compressive and adhesive strengths of atmospheric ice increase while the air temperature decreases during ice accretion; 2) Compressive strength of atmospheric ice increases with increasing wind speed during accretion; 3) Maximum values of compressive strength measured at the low speed deformation (0.76 mm/min) and high speed deformation (26 mm/min) were 17395 kPa and 10745 kPa, respectively, and 4) the maximum adhesive strength from an axial shear test (Druez et al. (1979)) was reported 181 kPa at −10 °C . The glaze icing was formed by water droplets of 40 μm mean diameter and air liquid water content of 0.8 g/m^3.

Most of recent studies on atmospheric icing have been done at CIGELE laboratory (Industrial Research Chair on Atmospheric Icing of Power Network Equipment at Université du Québec à Chicoutimi). Kermani *et al.* (2007) performed more than 180 tests at three different temperatures (−6, −10 and −20 °C) and liquid water content value of 2.5 g/m^3. Each type of glaze ice (distinguished by its accumulation temperature) was tested at the same temperature at which it had been accumulated in wind tunnel, to measure the behaviour of atmospheric ice under pure compression. The reported results showed that the compressive strength of atmospheric ice increases when test ambient temperature decreases (the same result as Druez *et al.* (1986)). In addition, it was shown that the dependency of strength on temperature is strongest in the mid range of the strain rates that were tested, i.e. at around 3×10^{-3}/s.

Figure 2.2 shows the comparison between the Kermani's results and those of other investigators for fresh water ice as reported in Hawkes and Mellor (1972), Schulson and Cannon (1984), Schulson (1990) and Jones (1982). For all fresh water ice tests, the average grain size has been reported as approximately 1 mm and test temperature was

−10 °C. These conditions approximately correspond to the ice accumulated at −10 °C and tested at −10 °C in Kermani *et al.* (2007). The results of the only published report on the compressive strength of atmospheric ice before Kermani by Druez *et al.* (1986) are also included in Figure 2.2.

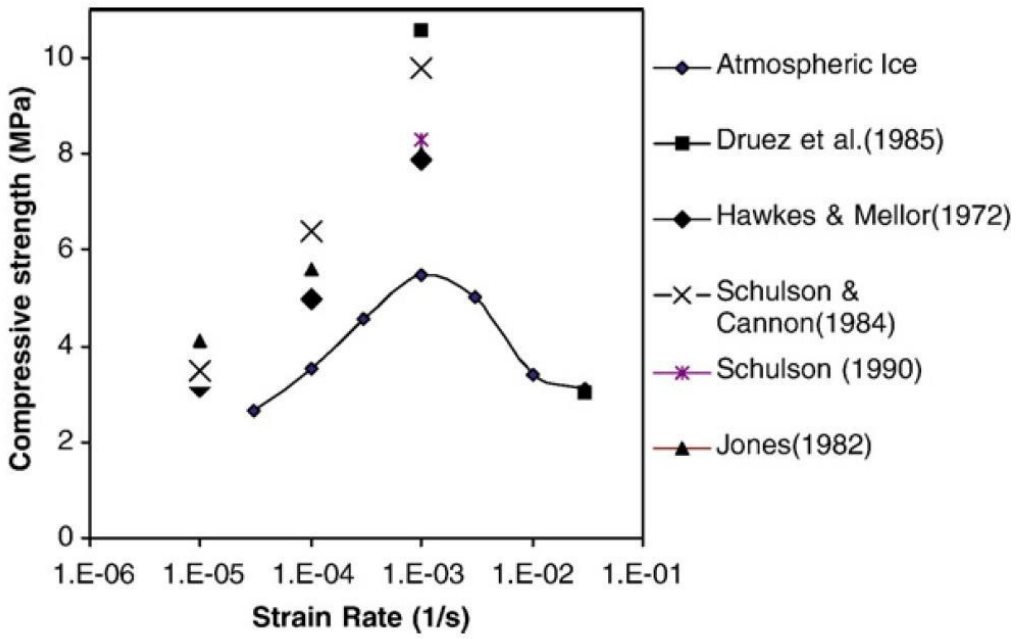

Figure 2.2 Comparison of compressive strength data of atmospheric icing with results from other studies on fresh water ice (source: Kermani *et al.* (2007))

Several discrepancies in the results of the compressive strength are observed in Figure 2.2. These differences have been attributed to the differences between liquid water content and wind speed during accumulation and the direction of loading in the tests. The other contributing causes of the discrepancies between the results of the investigators are the size and geometry of the tested specimens. Despite the differences between the reported data, the trend of increasing strength with strain rate up to 10^{-3}/s is confirmed by all data (Kermani *et al.* (2007).

Kermani *et al.* (2008) also performed 120 tests to measure the bending strength and effective modulus of elasticity of atmospheric glaze ice in the CIGELE atmospheric icing wind tunnel at temperatures of −6 °C, −10 °C and −20 °C with a liquid water content of 2.5 g/m3 and at different strain rates. Figure 2.3 shows the results of bending strength tests. The average flexural strength of atmospheric ice accumulated at −10 °C and tested at the same temperature at a strain rate of 10^{-4}/s has been calculated to be 2.92±0.26MPa. These tests showed a clear dependency of bending strength of atmospheric ice on test temperature at low strain rates. Figure 2.4 shows the results of effective modulus of elasticity obtained from bending tests. At a test temperature of −10 °C and strain rate of $2\times10-3s^{-1}$, the average effective modulus of atmospheric ice accumulated at −10 °C has been found to be 1.06±0.17GPa. The results revealed that, in most cases, the effective modulus of elasticity of atmospheric ice increases with increasing strain rate (Kermani *et al.* (2008)).

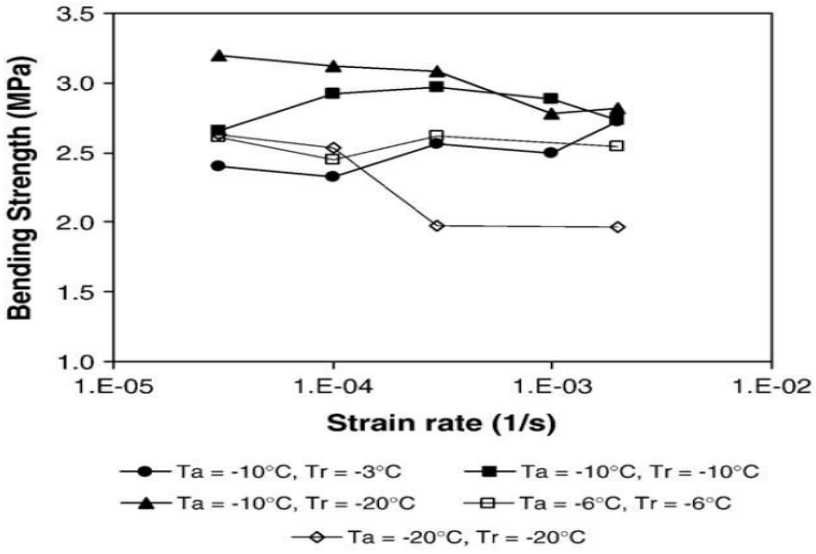

Figure 2.3 Bending strength of atmospheric ice accumulated and tested at various temperatures. (Ta=Accumulation temperature; Tr=Test temperature) (Source: Kermani et al. (2008)).

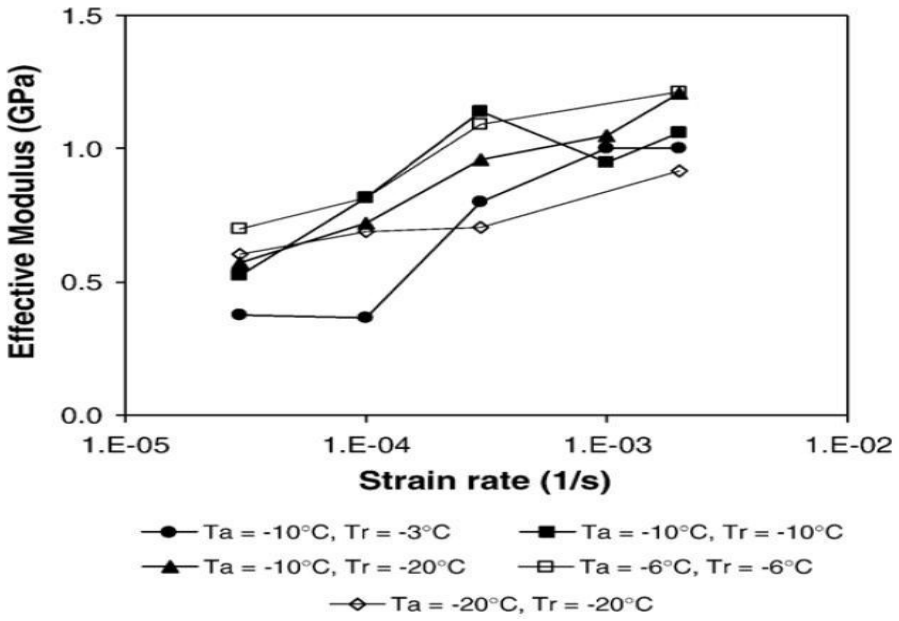

Figure 2.4 Effective modulus of atmospheric ice accumulated and tested at various temperatures (Source: Kermani *et al.* (2008)).

Despite the recent and ongoing research effort at CIGELE laboratory, reliable information on the mechanical properties of atmospheric ice in natural conditions is still lacking. Precise information on the properties of the ice formed in Kálmán's experimental study is not available, which makes it difficult to compare numerical simulation results with experimental results. Consequently, the mechanical properties of fine-grained fresh water ice (Kálmán 2007) are used throughout in all the numerical simulations presented in Chapter 3.

Ice adhesion strength

While efforts to develop mechanical ice removal techniques have received the most attention, few studies have focused on the fundamental mechanism of ice adhesion. The mechanism is very difficult to characterize because of its high sensitivity to test conditions, i.e. ice type (Petrenko and Whitworth, 1999) and material structure, ice–substrate interface, temperature and test techniques (Sayward, 1979). The adhesive strength is determined from the applied force (stress resultant) needed to separate the ice from the substrate. Ice adhesion has been measured in a variety of ways but the results are relatively scattered and difficult to compare because adhesion strength is highly sensible to differences in test conditions. One of the first attempts to develop a new technique for the determination of the adhesive strength of atmospheric glaze ice was performed by Javan-Mashmool (2005; Javan-Mashmool *et al*. 2006). The method was based on the bending vibrations of a composite beam composed of an aluminum beam and an ice layer deposited on this beam substrate. The mean value of four tests for the adhesive strength of the ice on the aluminum was 0.285±0.067 MPa, and resulted from the contribution of bending and shear forces generated at the ice–beam interface. Another test which has been recently developed at Université du Québec à Chicoutimi is called centrifugal adhesive test. In this method each composite beam (composed of an aluminum beam and an ice layer) is placed into the centrifuge specially adapted to measure ice adhesion. The centrifugal body force applied at the centroid of the ice deposit is reacted by a direct shear force at the ice-substrate interface. The body force is controlled by the angular velocity of the centrifuge and the mass of the ice deposit, and it can be measured precisely when the ice layer detaches from the aluminum surface. The adhesive strength is then calculated by

dividing this force at rupture by the dimension of the contact surface. The mean value reported for the adhesive strength of a heavy rime ice of 0.88 g/cm^3 and at a temperature of -10 ºC on the aluminum surface from three tests was 0.64 ± 0.04 MPa (Lima and Amil 2006).

2.2 Numerical modelling of ice shedding

Dynamic analysis of line conductors subjected to ice shedding induced by shock load is complex. (Kálmán, 2007) Prior to Kálmán's work, most studies had either considered the line response to instantaneous shedding or assumed the ice failure propagation along the span. The first study that used advanced FEM to simulate ice shedding phenomena was performed by Jamaleddine *et al.* (1993) with ADINA (Adina R&D Inc 2008). Their numerical results were compared to experimental results obtained on a reduced-scale model. In the main set of results, ice shedding effects were simulated by the sudden drop of small dead weights suspended to the cable. A second series of results related to random shedding by melting (gradual warming) of wet glaze ice deposits formed on the same suspended span in cold chamber.

After Jamaleddine's work, Roshan Fekr and McClure (1998) improved the modeling approach and applied it to simulate instantaneous ice shedding from a two-span line section with real-scale parameters. Such models were quite demanding on computational resources and further developments had to wait technological progress.

Further progress occurred ten years later, when Kálmán developed a numerical model where the ice deposit is explicitly considered so that modeling of ice failure propagation

along the span became possible. This new approach was applied to study the dynamic effects of shock-load-induced ice shedding on a single level-span. The numerical study considered several ice shedding scenarios with variables including: glaze ice thickness, cable diameter, span length, cable tension and axial rigidity, and pulse-load characteristics. To compare analytical results with experimental results, a reduced-scale span was tested in CIGELE Laboratory at Université du Québec at Chicoutimi. The proposed ice failure model was based on the maximum bending stress of an elastic beam ice deposit defined in parallel with each cable finite element; the maximum yield stress of glaze ice was taken as 2.0 MPa in the numerical simulations (Kálmán 2007; Kálmán *et al*. 2005 and 2007).

2.3 Modeling of realistic line sections subjected to cable ruptures

In early 1900's, researchers showed interest in longitudinal loads coming from broken conductor phenomena in transmission lines (Peabody 2001) and it was recognized that suspension structures were not strong enough to resist these loads. In fact, in particular cases the cable rupture event could lead to progressive collapse of the structures which is known as cascading failure phenomenon.

Numerical methods using finite element software have been used to find the maximum cable tension and longitudinal loads at suspension structures in recent years.

Numerical simulations

Use of finite element analysis to simulate line sections subjected to cable breakage began near 1980 (McClure 1989). Baenziger (1981) developed software named CABLE7.

The finite element models studied by Baenziger were two-dimensional and were able to provide fundamental understanding of the dynamic behaviour of line sections. Different line parameters were investigated including: span length, insulator string length, tower stiffness, and initial conductor tension. It was reported that time histories of ruptured conductor tensions are characterized by two distinct peaks. The first peak is attributed to recoil of the conductor while the second peak is caused by bottoming down of the conductor.

McClure *et al.* (1987, 1989, 1991) were the first to use commercial finite element software to perform large kinematics nonlinear dynamic studies of cable breakage problems in both two- and three-dimensional line section models to investigate the contribution of intact spans, shield wires, and flexural rigidities of the structures to the dynamic behaviour of line sections. Consideration of intact wires was proven to be essential as they reduced the maximum load amplitudes and the magnitude of the calculated displacements. Also shield wires were found to participate in the dynamic behaviour of the line sections. In the early 1990s, constructing more detailed 3D models was still quite demanding on computational resources and further developments had to wait for more technological progress in computer hardware.

Lapointe (2003) and McClure (2002, 2003) were able to construct more detailed 3D finite element models where the torsional flexibility of suspension structures could also been taken into the account in simulations of line response to cable rupture. Cable rupture was simulated by instantaneous removal of all cable elements in the suffered spans at once. It was confirmed that the dynamic loads induced by a conductor breakage act along the longitudinal direction of the line section and transverse loads could be neglected.

Also, it was reported that suspension structures adjacent to the broken span and dead-end structures are subjected to the highest longitudinal loads.

It is important to note that the model developed by Lapointe (2003) served as the basis of Chapter 5 simulations.

3. Improved ice shedding modelling of iced cables: a comparison with experimental data on reduced-scale model

3.1 Introduction

As a follow-up on Kálmán's work (2007), the primary objective of this chapter is to introduce an improved ice failure criterion where the ice deposit is assumed a bilinear material and the failure criterion is based on maximum bending strains in the glaze ice element with assumed post-elastic constitutive material model. For easier reference in reporting the results, the author names this criterion as "strain criterion" and the previous criterion based on elastic maximum bending stress is referred to as "stress criterion".

3.2 Modeling consideration

The same three ice-shedding scenarios studied by Kálmán (2007) on the single level-span reduced-scale model are studied here, with ice thickness equal to 1, 2 and 4 mm, respectively. For easier retrieval of some response indicators and improved numerical processing, the models were created anew. A stainless steel cable with a diameter of 4.1 mm is used and the span length is set to 4 m with an initial sag-to-span ratio of 6%. Figure 3.1 shows the schematic iced cable span (part a) and three types of elements that are used in this model (part b) and are introduced in the following sections.

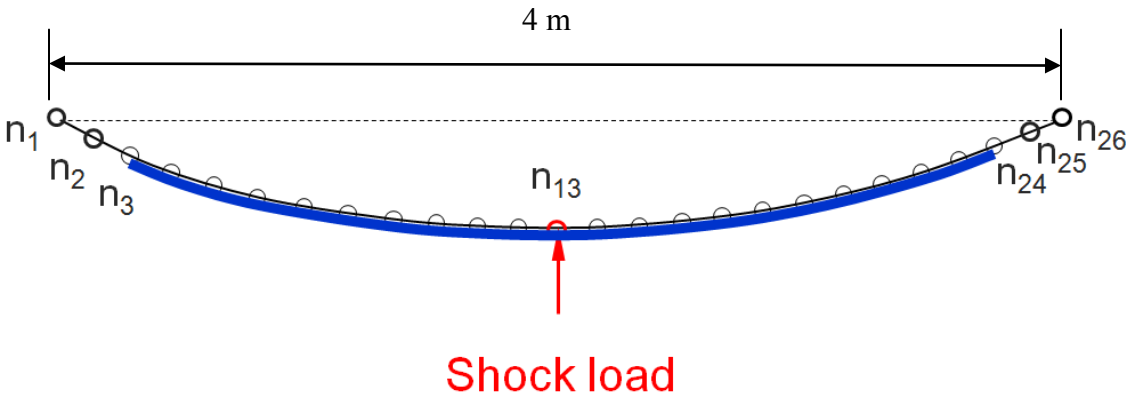

a) Schematic of the iced span

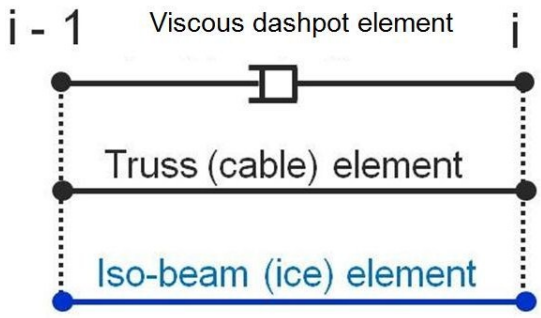

b) Iced cable model representation

Figure 3.1 Iced cable modeling approach

3.3 Bare cable model

The first step to simulate ice shedding correctly is to find an accurate model to represent bare cable behaviour. A comprehensive study was done by Kálmán (2007) to

investigate model sensitivity to mesh size, and the influence of support flexibility and cable tensional rigidity. As a conclusion of these sensitivities studies, a finite element mesh with 25 3-D two-node isoparametric truss elements is used for the bare cable analysis. This mesh size is also used in the iced cable analysis due to its satisfactory results in Kálmán (2007) and in the current study. Moreover, two cable material models have been used: a theoretical tension-only cable material with constant Young's modulus (Figure 3.2) and a more accurate multi-linear model (Figure 3.3) based on tensile tests on the cable specimen (Kálmán 2007). It is understood that the stresses induced in the cable material in the loading scenarios considered will remain below the elastic limit of 105 MPa corresponding to 0.004 strain. However, larger strain ranges typically need to be defined to accommodate equilibrium iterations in the numerical procedures.

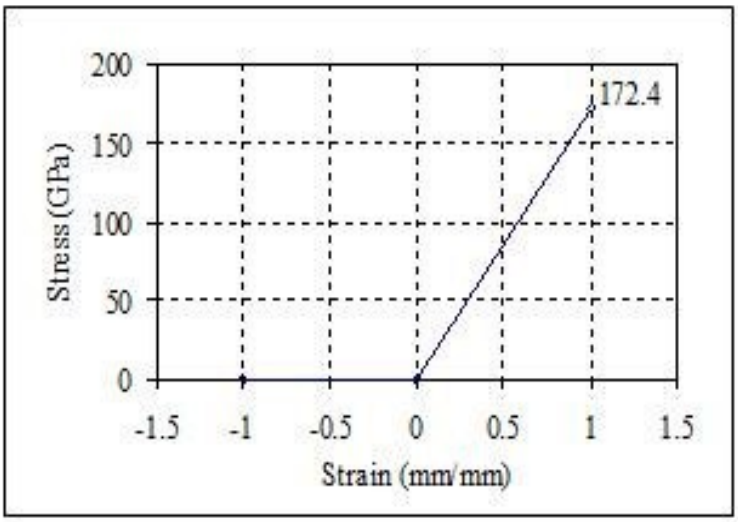

Figure 3.2 Tension-only elastic model (MAT-1) (Kálmán 2007)

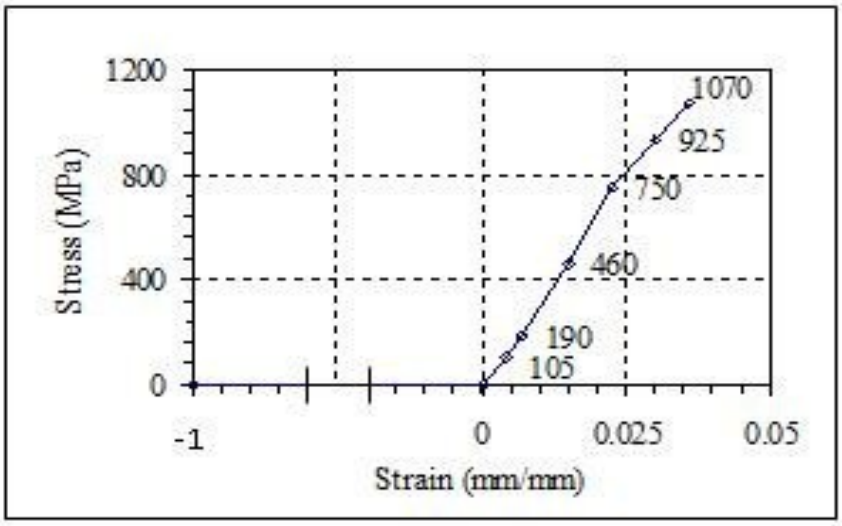

Figure 3.3 Multi-linear tension-only elastic model (MAT 2) (Kálmán 2007)

3.4 Iced cable model

Following the approach used in Kálmán (2007), accreted ice on the cable is modeled as separate 3-D two-node isoparametric beam elements with rectangular cross section in parallel to each cable element described in section 3.3, i.e. the beam connectivity is defined using the cable nodes. The choice of rectangular cross section is based on the fact that isoparametric beam elements are recommended to be used in large kinematic problems and since only rectangular cross sections can be considered for the materially nonlinear isoparametric beam element in ADINA, it is selected as the appropriate cross section. The second moment of area and cross-sectional area of the rectangular beam are set as equivalent to those of an idealized cylindrical round shape of accreted ice on cables to calculate its equivalent width (W) and depth (D). Due to limitations in droplet spraying trajectory in the CIGELE laboratory where the glaze ice deposits were formed, a short length of 30 cm at both ends of the cable remained without ice. This was reflected in the

numerical model by omitting two ice-beam elements at each cable end, for a total number of 21 ice-beam elements in the span (Kálmán 2007).

The ice deposit mass and the dimensions of the rectangular ice beam model are as listed in Table 3.1; they are inputted directly to define the stiffness and mass matrices of the isoparametric beam elements. Since ice is a complex material that can have highly variable mechanical behaviour depending on its microstructure, loading rate, temperature, etc. simplifications had to be made in the numerical material model. In this research we have used the mechanical properties of fine-grained fresh water ice due to the lack of more specific data on dense glaze ice under high strain rate. So for this study, ice is assumed as an isotropic elastic-plastic material, with the following elastic properties in the linear range of response: Young's modulus of 10 GPa, Poisson's ratio of 0.33 and normal yield stress of 2 MPa (Kálmán 2007). The same properties are used in tension and compression.

Table 3.1 Dimensions and mass of the ice beam elements

Ice-shedding scenario	Ice thickness	Cross-section of ice accretion (W x D)	
	T_{ice} [mm] (Mass per unit length)	W [mm]	D [mm]
1	1 (14.4 g/m)	6.36	2.52
2	2 (34.5 g/m)	7.86	4.87
3	4 (91.6 g/m)	11.06	9.20

Glaze ice failure modelling

Failure of the ice beam representing the glaze ice deposit accreted on the cable is modeled using the *element death upon rupture* option available in ADINA. The rupture of the ice-beam deposit (Figure 3.4) is defined in terms of a maximum allowable effective plastic strain (ε_p). Whenever this maximum strain criterion is fulfilled at any integration point of the ice-beam element, the *element death* is automatically activated for the remainder of the analysis, and the mass and stiffness contributions of the element are reset to zero. (Adina R&D Inc. 2008) In our application, this means the ice element is suddenly detaching from the cable.

The maximum allowable plastic strain is determined for each ice load scenario as per Equation 1 based on the assumption that the bending strains vary linearly on the cross section (Figure 3.4). It is further assumed that the ice deposit is centered on the supporting cable such that the neutral axis of the beam coincides with the cable centroidal axis. In the numerical simulations based on the ideal elastic-plastic ice material model, the ice-beam subjected to pure bending at rupture will yield from its interface at the cable surface ($\varepsilon_y=2*10^{-4}$) to the extreme top and bottom fibers where the total bending strain reaches $\varepsilon_y+ \varepsilon_p$. This idealized pure bending calculation only serves the purpose of getting a numerical value of the maximum strain in the ice beams. In reality, the ice deposit is highly stressed due to its compatibility of axial displacements with the conductor and the strain rupture criterion will be checked with the combined axial and bending effects in the ice beam.

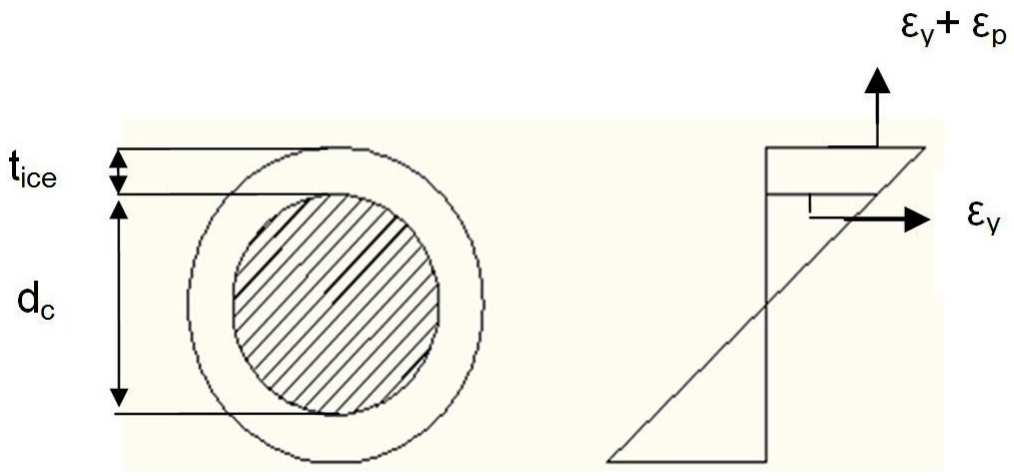

Figure 3.4 Iced-cable normal strain distribution at rupture

$$[1]\ \frac{d_c}{d_c + 2 * t_{ice}} = \frac{\varepsilon_y}{\varepsilon_y + \varepsilon_p}$$

3.5 Damping

Damping in cable structures is complex and difficult to account for in time-domain dynamic analysis. Furthermore, the effect of ice accretion on conductor damping has not been studied or results of such studies have not been published in the open literature. Peabody (2004) modelled both aerodynamic and internal damping in bare cables and confirmed that aerodynamic damping effects in still air conditions were small enough to be neglected in transient dynamic analysis following cable breakages. Considering that this study is concerned essentially with transient response following ice shedding, and based on the satisfactory results obtained in previous work (Jamaleddine *et al.* 1993, McClure and Lapointe 2003, Kálmán 2007), the aerodynamic damping is neglected and

only axial viscous damping of the cable is considered. Damping is modeled by using a lumped-parameter generic element option in ADINA (a nonlinear spring-mass-dashpot element) which allows modelling a viscous dashpot with prescribed constant in parallel with each cable element. The damping constant is set to represent an equivalent viscous damping of 2% critical (Lapointe 2003). Numerical damping is also used to filter out spurious high frequencies of the response due to finite element discretization; it is introduced using the Newmark integration method with parameters δ and α set to 0.55 and 0.3, respectively, relying on the work of McClure and Guevara (1994) on seismic analysis of tall guyed telecommunication masts.

3.6 Static analysis

The initial configuration of the iced cable is determined using the inextensible catenary equation to avoid the artificial stiffening effect of the isoparametric ice-beam elements on the initial static profile. In reality, this effect is also attenuated by the fact that ice accumulates gradually on the exposed spans as their profile adjusts. Two approaches were examined to calculate the deformed cable configuration. The first one considered a composite ice-cable section so that the mass per unit length will be a summation of that of ice and cable. After using the catenary equation to calculate the initial nodal point positions and cable axial strains, a static analysis of this initial profile in ADINA resulted in a relaxed final static profile accounting for cable-ice elasticity. In the second approach, the bare cable geometry and initial axial strains are defined using the inextensible catenary equation and static analysis proceeds to determine the cable's relaxed static position under self-weight. Afterwards, using the *element birth* option in ADINA, the ice-

beam elements are added and the final iced-cable profile is determined from static analysis. These two approaches lead to only slight differences in the results and the author decided to keep the first approach to be consistent with previous studies.

3.7 Dynamic analysis

Dynamic analysis starts from the final static profile obtained for the iced cable by using the *restart* option in ADINA following an external shock load which is applied to the cable mid span. The characteristics of the shock loads are presented in section 3.8. Incremental static analysis to determine the initial iced cable profile (see Section 3.6) is completed in 10 steps (set to 0.1 s each) so that dynamic analysis is started at time t = 1 s and continues for a total duration of 3 s. In dynamic analysis, the selection of the time step and the mesh size is based on adequate sampling of the generated wave in the cable as it goes through out the finite element mesh. After some numerical experiments and considering the previous time step selection by Kálmán (2007), it was found that a time increment of 0.25 ms was appropriate for the mesh selected, while finer time steps would be implemented automatically whenever required by activating the *ATS* (automatic time-stepping) option in ADINA. A lumped mass formulation is used. As mentioned in Section 3.5, the Newmark-β direct integration method is used, with the full Newton-Raphson iteration method for stiffness updates (Adina R&D Inc 2008, Bathe 1996).

3.8 Results

3.8.1 Comparison of numerical and experimental response

Figure 3.5 to Figure 3.10 compare the experimental results obtained at CIGELE (Kálmán 2007) with the time history results obtained from finite element analysis. Response values compared are the cable tension at the supports and mid-span displacement, as well as the rate of ice shedding (RIS) in the span. RIS is defined as the fraction of ice elements which shed to the total number of iced elements (n=21). The numerical simulation results are also presented for the two different ice failure criteria used in the study: the new maximum plastic strain and the maximum bending stress used by Kálmán. Figure 3.6, Figure 3.8 and Figure 3.10 also show the measured vertical shock loads applied to the iced span by the piston used in the experimental set-up: these shock loads define the external vertical (upward) point load which serves as input to the numerical model and is applied to the cable mid span node.

Figure 3.5d, Figure 3.7d and Figure 3.9d show that for each of the three ice thickness scenarios, the maximum cable jump caused by shedding effects is reasonably well predicted (5% to 10% differences with the experimental data) using either of the two ice failure models. However, the maximum plastic strain criterion leads to slightly smaller cable jump amplitudes due to the larger number of ice elements that remain on the cable as compared to the stress criterion. This is especially significant in the third scenario where ice elements are thicker and therefore heavier (23% underestimated compared to the experimental data).

The time history results of cable tension at the right support (Figure 3.1) indicate the consistency between the models using the two rupture criteria. Both sets show that the

thicker the ice deposits on the cable, i.e. the higher the bending stiffness of the ice-beam elements, the better the accuracy in maximum cable tension. It should be noted that differences are expected in the two numerical models and between these models and the physical test results in terms of both amplitude and time shift after the first peak (due to the point external load) has occurred. As soon as some ice elements are dropped off the cable, the three systems evolve in a slightly different manner. It is seen that for the third scenario with equivalent radial ice thickness of 4 mm, the maximum cable tension is underestimated by the numerical models. This may be related in part to the inherent bending stiffness of the real cable, which is neglected in the analysis.

As expected, the rate of ice shedding (RIS) obtained experimentally is different for each scenario. The results are summarized in Table 3.2, where "effective ice shedding" is defined to occur where ice elements completely detached from the cable, while "assumed ice shedding" also accounts for those elements that suffered extensive cracking (highlighted in grey in Figure 3.6, Figure 3.8 and Figure 3.10) but remained on the cable in addition to the detached elements. This "assumed ice shedding" definition introduced by Kálmán (2007) essentially serves the comparison between the numerical and experimental results in terms of the amount of ice deposit fracture due to excessive bending stresses. It is clear that in practice, it is the "effective ice shedding" condition - for which the ice deposit is dropped from the overhead line - that matters most for mitigation.

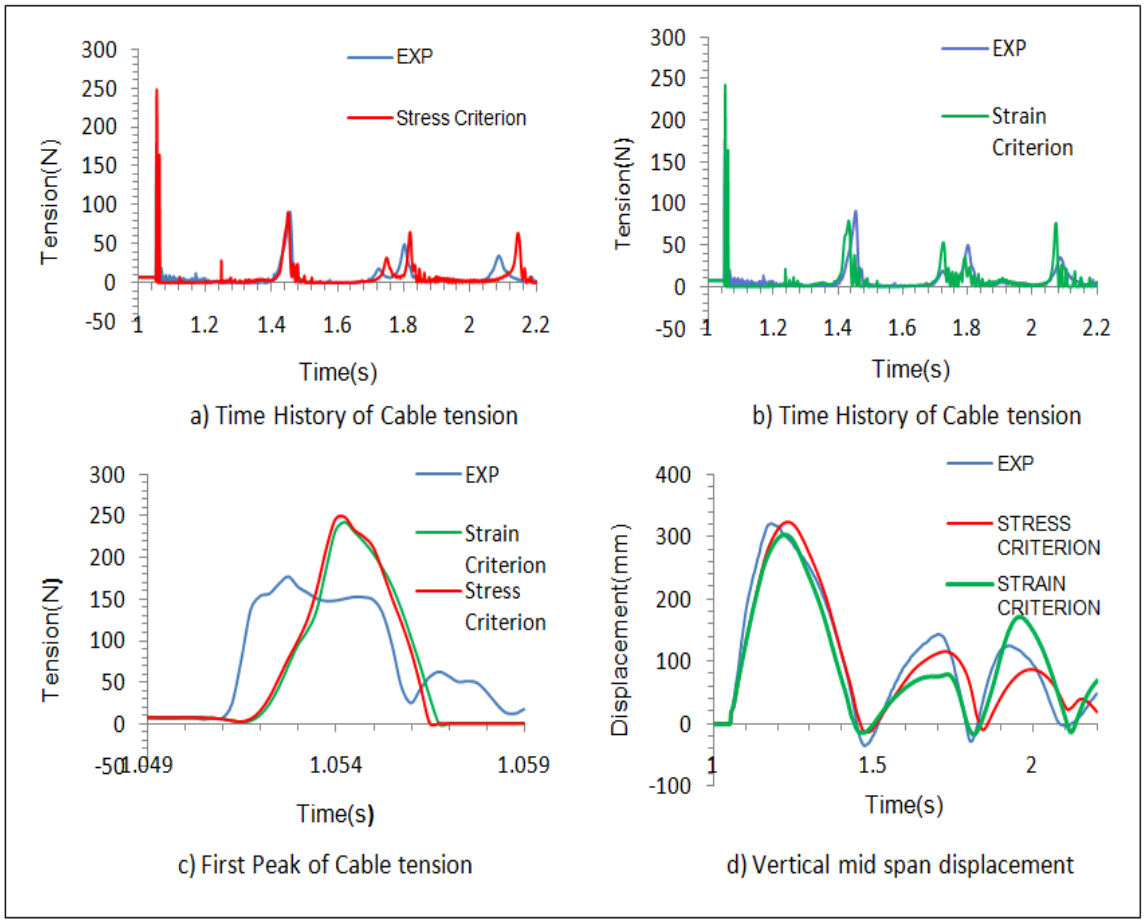

Figure 3.5 Numerical and experimental results of cable tension at support and cable jump at mid span for the 1st icing scenario (t_{ice}=1 mm)

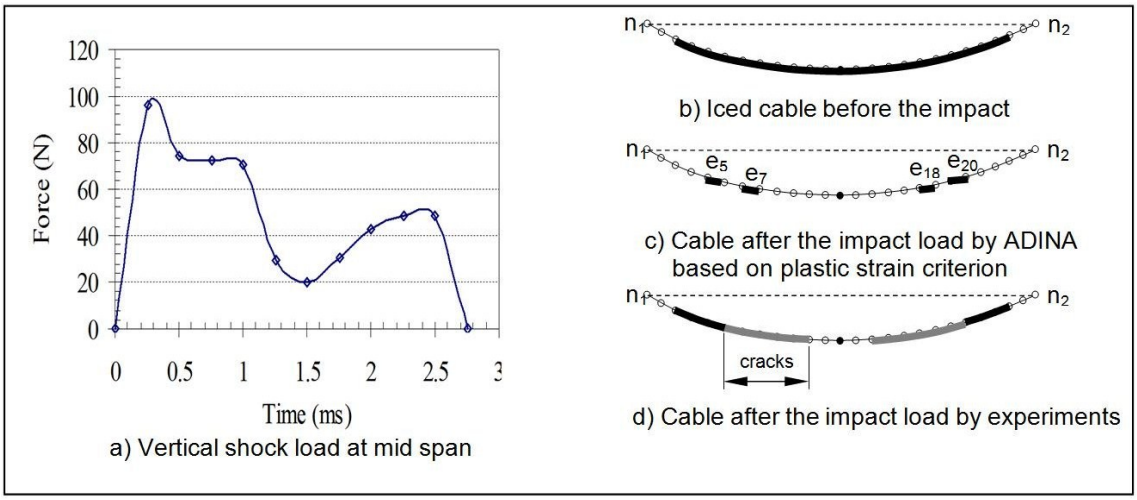

Figure 3.6 Impact load and final state of ice shedding obtained from ADINA models and experiments for the 1st icing scenario (t_{ice}=1 mm)

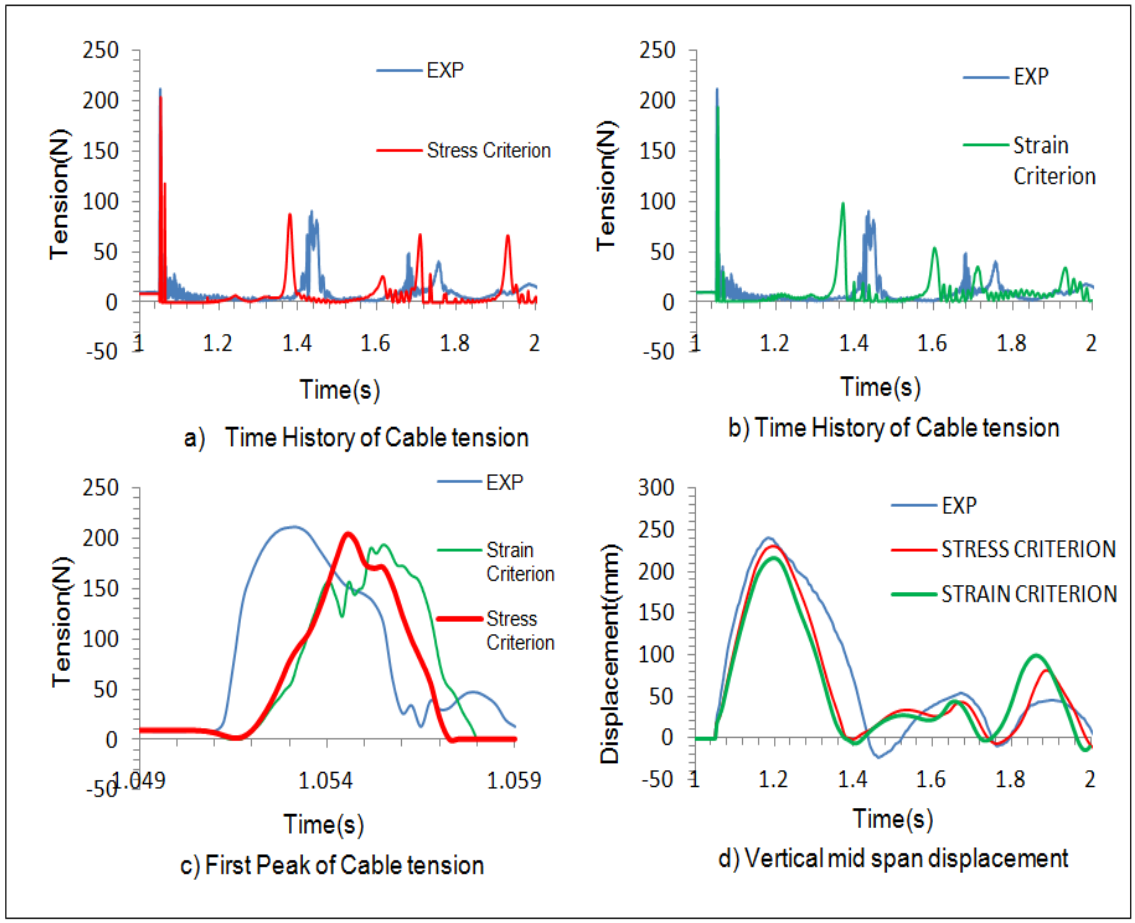

Figure 3.7 Numerical and experimental results of cable tension at support and cable jump at mid span for the 2nd icing scenario (t_{ice}=2 mm)

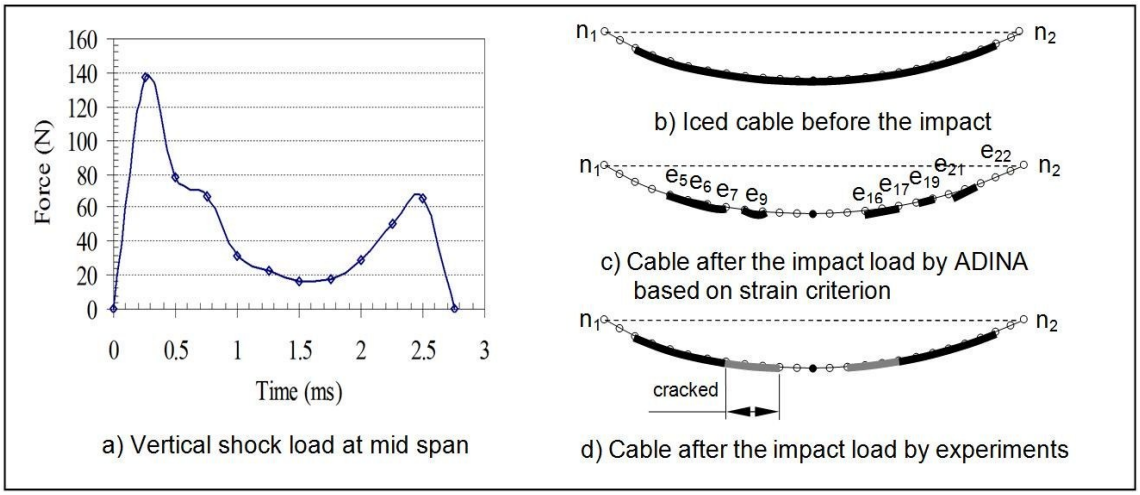

Figure 3.8 Impact load and final count of ice shedding obtained from ADINA models and experiments for the 2nd icing scenario (t_{ice}= 2 mm)

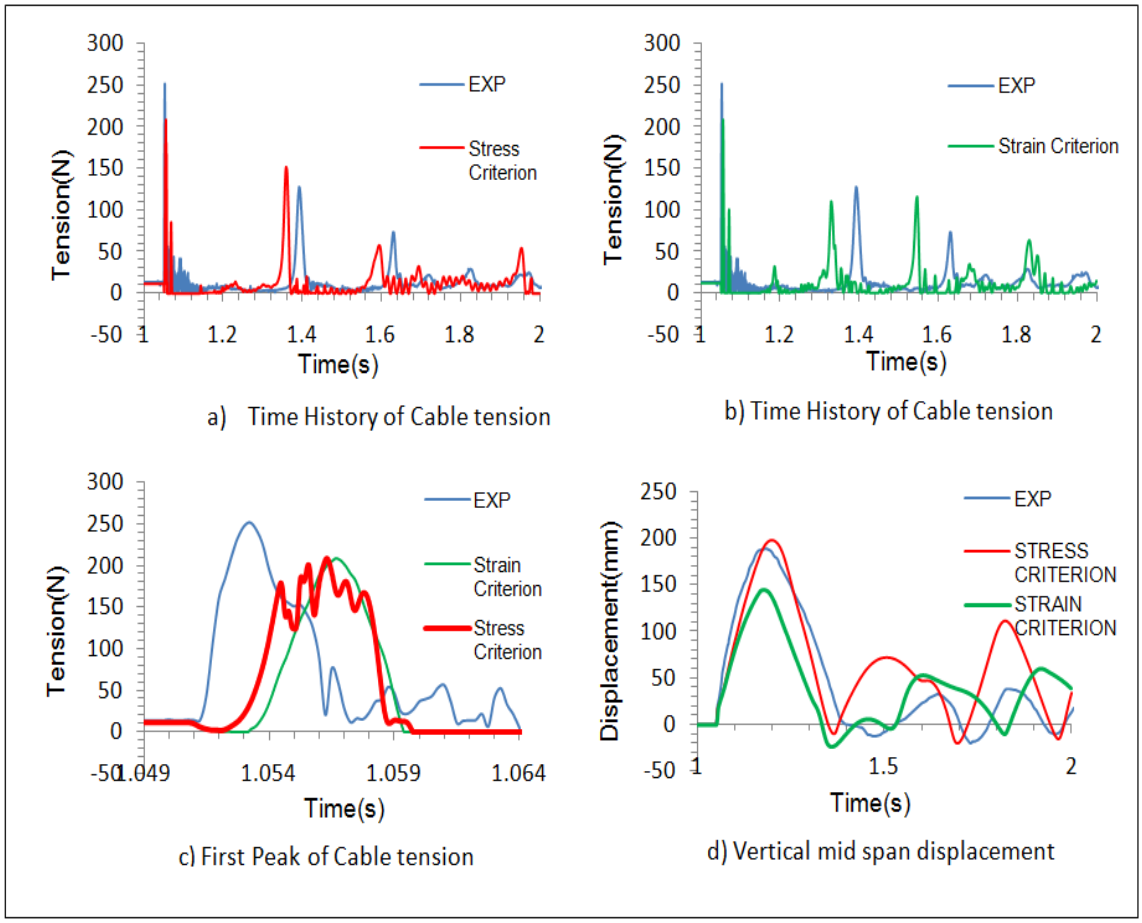

Figure 3.9 Numerical and experimental results of cable tension at support and cable jump at mid span for the 3rd icing scenario (t_{ice}=4 mm)

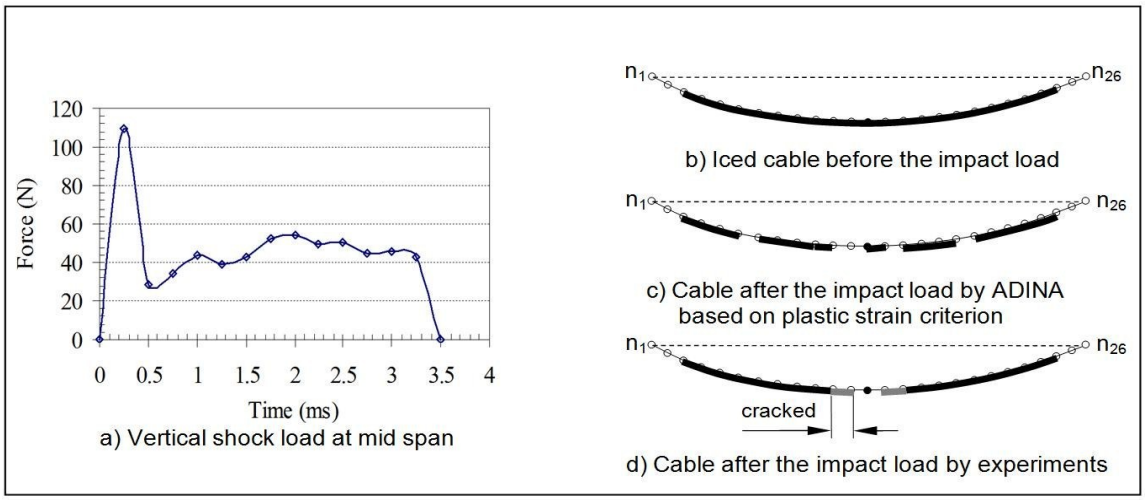

Figure 3.10 Impact load and final count of ice shedding obtained from ADINA models and experiments for the 3rd icing scenario (t_{ice}=4 mm)

It is seen in Table 3.2 that the R.I.S. values obtained by numerical simulations are largely overestimating the amount of effective ice shedding observed on the experimental model. These differences are reduced when comparing the numerical predictions with the assumed ice shedding rate. The results also indicate that the simulations based on the "maximum effective plastic strain" criterion in the ice beams have better predictive capabilities those using the maximum bending stress criterion.

Table 3.2 Rate of ice shedding (R.I.S.) obtained numerically and experimentally

Ice-shedding scenario	Ice thickness (mm)	R.I.S. by numerical simulations		R.I.S. by experiments	
		Strain criterion (%)	Stress criterion (%)	Effective (%)	Assumed (%)
1	1	81	95	19	71
2	2	57	81	19	48
3	4	24	62	10	19

We have a few explanations for the RIS discrepancies between the numerical simulations and the assumed RIS experimental results. First of all, the numerical simulations use the concentrated vertical piston force as the input without considering that there will be some localized distribution of this force at the physical loading point. The present model does not allow to study this effect since the cable mesh can accommodate loads only at nodal points. In the physical tests, both the ice deposits and the cable offer some bending rigidity to react to this localized effect, which is all the more amplified by the reduced scale of the model. There are of course other sources of energy dissipation

that are not accounted for in the model (at the supports, for instance) which may also explain the general trend observed in the simulations.

However, the effective RIS is of relevance and clearly, several of the ice elements assumed “dead” in the numerical simulations are in fact severely cracked deposits that remained attached to the cable. Since the adhesive strength of ice to the cable is not considered in the numerical models, the author believes that this is the main source of the modeling discrepancies. This had also been pointed out by Kálmán (2007). As exposed by Javan-Mashmool (2005, 2006), adhesive strength of ice may be difficult to characterize as it depends on many parameters such as loading rate, surface conditions and material, temperature, characteristic of substrate and surface energy. Experimental work to characterize the adhesive strength of glaze ice on overhead line conductors has been conducted recently at CIGELE by Javan-Mashmool *et al.* (2006) and other researchers. However, there is still a lack of knowledge on this topic. The next step in our model development is to combine the maximum plastic strain failure criterion presented in this study to an adhesive strength criterion.

3.8.2 Adhesive strength criterion

A small conceptual study was performed to observe the possibility of implementing adhesive criterion to our models. When the strain criterion is fulfilled at any integration point in one ice chunk element it is assumed to be fully cracked from the interface of ice and cable to the upper fibre of the ice deposit. However, in reality the ice deposit still remains attached to the cable unless the inertia force could overcome the adhesive force. Therefore, to model ice shedding phenomenon more properly there is a need to introduce a two-tier ice failure criterion which considers adhesive criterion in addition to strain criterion and the following equation should be satisfied:

Inertia force+ Ice chunk weight > Adhesive force

The author also tried to do a more quantitative analysis; however, due to the shortage of knowledge in adhesive force topic, the calculated parameters were seemed to be unrealistic. Thus, there is a need to do more investigation to quantify these terms accurately. Upon developing the analytical model, one can implement the adhesive force to the finite element model by using lumped elements (spring elements) where the stiffness could represent the adhesive force.

3.8.3 Effect of the variability of the yield strain in the ice beam at cable interface

One of the parameters which could affect the number of ice-beam elements remaining attached to the cable subsequent to a shock load in the numerical simulation is the value of the yield strain $\varepsilon_{y.}$ The value used in section 3.4 ($\varepsilon_y = 2*10^{-4}$) is not a very precise value because it varies with grain size, crystal structure and temperature for low deformation rates (Gow 1989 and Timco 1982) and it is rate-dependent at higher deformation rates. Therefore, the real value of ε_y should be considered with some variability around the value used in section 3.4. To observe the effect of different strain criteria at the ice-cable interface, different values of strain are introduced for first two scenarios of Table 3.2: ε_y+2%, ε_y+5% and ε_y+10%. The element numbers which remain on the cable after the shock load is applied are listed in Table 3.3.

Table 3.3 Effects of variability of yield strain of ice at cable interface

Ice-shedding scenario	Ice element numbers remaining on the cable		
	ε_y+2%	ε_y+5%	ε_y+10%
1	5,7,18,20	5,7,18,20	5,7,18,20
2	5,6,7,9,16,17,19,21,22	4,6,8,9,16,18,20,21,22	5,6,8,9,16,18,20,21,22

As it is seen in the result, having a larger strain at interface (even increased by 10%) is not beneficial in having more ice elements remaining attached to the cable as the RIS is not affected.

3.9 Conclusion

This numerical study has presented a new, improved failure criterion for glaze ice deposits intended for dynamic analysis of ice shedding effects on lines caused by the application of a shock load at mid span. The model was tested with experimental results obtained by Kálmán (2007) on a reduced-scale single span model. The proposed criterion, based on maximum effective plastic strain, yields more realistic predictions of ice fracture rates than a previous one based on maximum bending stress. However, both modeling approaches grossly overestimate the effective ice shedding rate. For the numerical models to be more accurate in predicting ice shedding, it is necessary to consider the adhesive strength of the fractured ice deposits that remain attached to the cable after the transient effects of the response are dissipated. The improvement of the prediction of ice fracture rates is the first step in the implementation of a two-tier ice rupture criterion that will also consider the adhesive strength of the fractured deposits.

4. Ice shedding simulations on real scale model of single span

4.1 Model details

In this chapter, the maximum plastic strain ice failure criterion model presented in chapter 3 and validated on a level single-span reduced-scale experimental model is applied to a real scale single span that has also been studied by Kálmán (2007). An ACSR (Aluminum Conductor Steel Reinforced) cable is used with the properties listed in Table 4.1. In section 4.2 an equivalent ice thickness of 10 mm is modeled as an iced beam, following the procedure described in Chapter 3. Furthermore, two different pulse loads applied at the mid span are represented by variation of load amplitudes (30 and 60 kN) while the duration and time history are kept constant (Figure 4.1). Initial sag-to-span ratio and span length are set to 5% and 300 m, respectively. 1500 elements are used to define the appropriate mesh size (Kálmán, 2007). Incremental equilibrium for initial static analysis is completed in 5 steps (set to 1 s each) so that dynamic analysis is started at time t = 5 s and continues for a total duration of 6 s. a time increment of 0.1 ms was appropriate for the mesh selected, while finer time steps are implemented automatically whenever required by activating the *ATS* (automatic time-stepping) option in ADINA.

In section 4.3 an equivalent ice thickness of 25 mm is modeled on the same cable. A pulse-load type with the amplitude of 60 kN is applied at mid span. The other model characteristics remain the same as in section 4.2. In fact, section 4.3 discusses the optimum mesh size to use in numerical ice-shedding simulations for real-scale conductors.

Table 4.1 Cable characteristics

Property	Conductor
Name Code	CONDOR
Type	ACSR
Diameter (mm)	27.8
Total cross-sectional area (mm^2)	455.1
Young modulus of the cable composite (GPa)	68.95
Mass per unit length (kg/m)	1.522
Weight per unit length (N/m)	14.93
Rated tensile strength (kN)	127

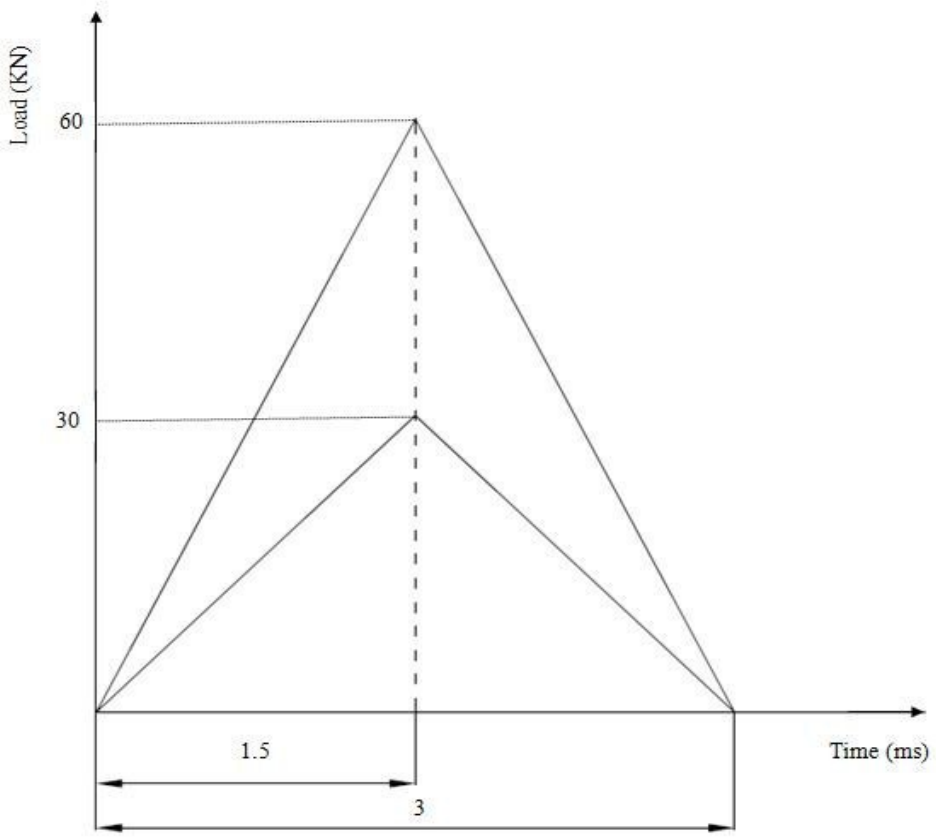

Figure 4.1 Pulse Load Characteristics

4.2 Comparison of stress and strain ice failure criteria

Figure 4.2 shows the schematic finite element model and a summary of the results is presented in Table 4.2. This table lists the number of ice elements remaining attached to the cable (n), the rate of ice shedding (RIS), the initial amplitude of the transverse wave (IWA), the maximum dynamic cable tension at mid span (MT) and at the support (MTS), as well as the maximum cable jump at the mid span (MD). Displacements are calculated with respect to the static profile of the fully iced cable.

As indicated in Table 4.2, the pulse load with 60 kN amplitude triggers 100% ice shedding in both failure criterion scenarios. However, the 30 kN pulse load carries less energy and predicts a RIS of 83% (252 elements remain attached) with the proposed plastic strain criterion, while only 49 elements remain attached when the stress criterion is used. The other results such as MT, MTS and MD are close in both ice failure criterion scenarios with slight differences; since as soon as different ice-beam elements drop off the span, each scenario evolves in a slightly different manner. However, in both ice failure criteria, a load of 60 kN generated additional tension in the cable at the excitation point that exceeded the rated tensile strength of the cable, which cannot happen in reality. Therefore, to avoid damaging the cable, it may be necessary in practice to apply successive lower amplitude shock loads at a given point along the span or at two or more points. Therefore, these simulations show that it is feasible to implement the new strain-based failure to real scale problems.

Also, for the strain criterion case with 30 kN pulse load, time history results of the cable tension at mid span and at support, displacement at mid span as well as vertical accelerations at mid span and at support are shown in Appendix A. The maximum

vertical accelerations at mid span and at support are around 4000g and -50g. The acceleration values at mid span are assumed to be spurious and not realistic. However, in numerical simulations, the inertia forces resulting from these unrealistic accelerations are forcing ice shedding. Further investigations are needed to resolve this problem in the numerical models.

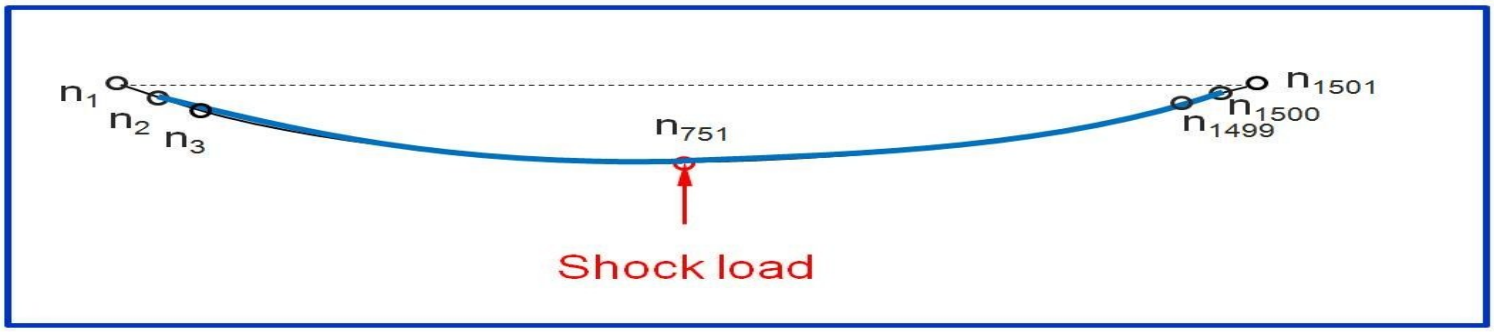

Figure 4.2 Finite element model

Table 4.2 Results of two ice-shedding scenarios of an ACSR conductor

Span (m)	load (kN)	stress criterion						strain criterion					
		n	RIS (%)	IWA (m)	MT (kN)	MTS (kN)	MD (m)	n	RIS (%)	IWA (m)	MT (kN)	MTS (kN)	MD (m)
300	60	0	100	0.24	131.8	57.2	0.803	0	100	0.22	131.6	56.9	0.805
	30	49	96.7	0.10	76.6	29.1	0.480	252	83.2	0.10	75.8	32.1	0.580

4.3 Finding the optimum mesh size for an iced span

This section discusses the optimum mesh size to use in ice-shedding simulations for real-scale conductors. The maximum plastic strain criterion is used in the models.

4.3.1 Eigenvalue and FFT analysis of the iced cable with 1500 elements

A 300-m CONDOR span with an equivalent ice thickness of 25 mm under an excitation of a pulse-load type with the amplitude of 60 kN at mid span is modeled to validate the proposed refined mesh size (1500 elements) in section 4.2. Therefore, the natural frequencies and mode shapes of the iced cable are calculated from the model and compared with the analytical solution (Irvine 1981); results of the first four modes are listed in Table 4.3 and the 1st asymmetric mode shape is illustrated in Figure 4.3.

Table 4.3 Natural frequencies and mode shapes

Mode	Finite element model (Hz)	Irvine's theory (Hz)
1st asymmetric	0.27	0.27
1st symmetric	0.39	0.38
2nd asymmetric	0.55	0.55
2nd symmetric	0.66	0.55

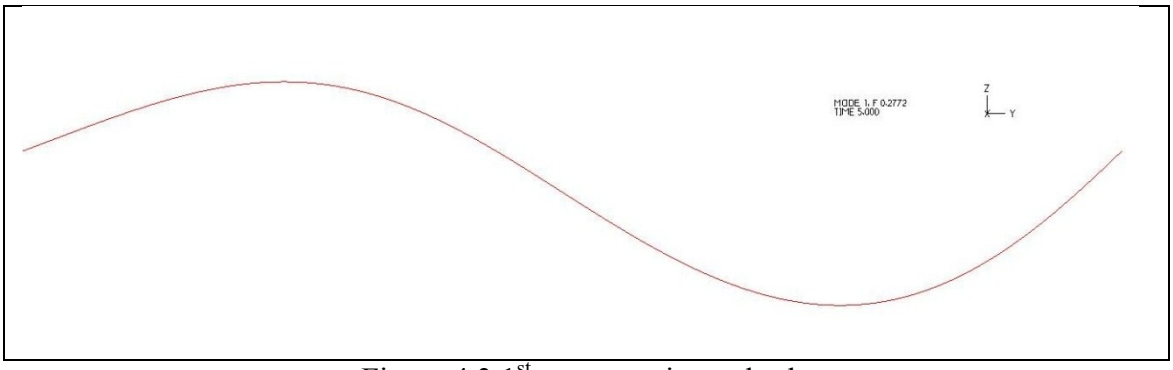

Figure 4.3 1st asymmetric mode shape

The frequencies are identical in all cases except for the 2nd symmetric mode; this discrepancy is explained by the fact that the iced-cable model comprises beams and truss elements and cannot assume that an exact catenary shape. The model was made anew by using an increased density truss elements with the same mesh size and the natural frequencies were the same as predicted with Irvine's theory.

Considering that 1500 elements make for a very fine mesh to capture the successive ice shedding of adjacent ice chunks, other coarser meshes are studied in this section to find out the optimum mesh size for the study. The first step is to study the frequency content of the cable response using FFT analysis on the 1500-element model.

Cable tension at the right support is illustrated in Figure 4.4: the maximum tension is 61.4 kN and it oscillates about its initial value. Figure 4.5 shows the FFT analysis of this cable tension time history. The dominant frequencies are at the low end of the spectrum (coinciding with the lowest few in Table 4.3) and there is another peak of 9.77 Hz. In fact, the shock load generates longitudinal waves (in addition to transverse waves) that propagate back and forth along the span at an approximate speed of 4.5 km/s (Main 1978). This fundamental longitudinal (axial) vibration of iced cable creates the high frequency oscillations of the cable tension (evaluated at 9.77 Hz).

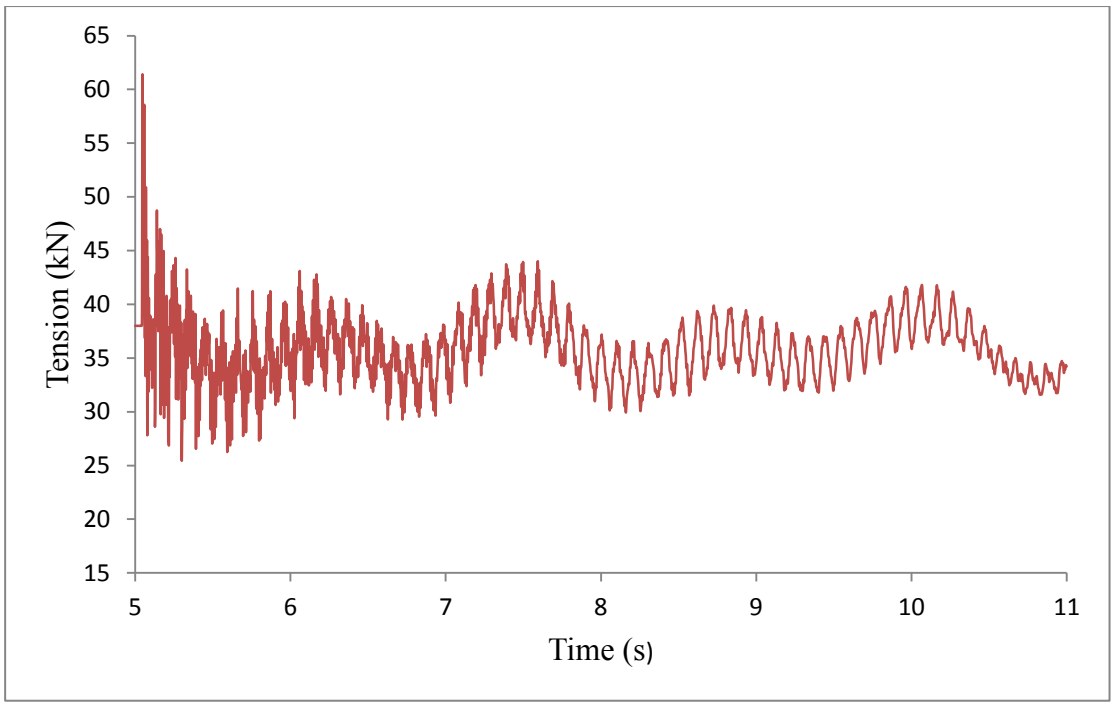

Figure 4.4 Cable tension at the right support

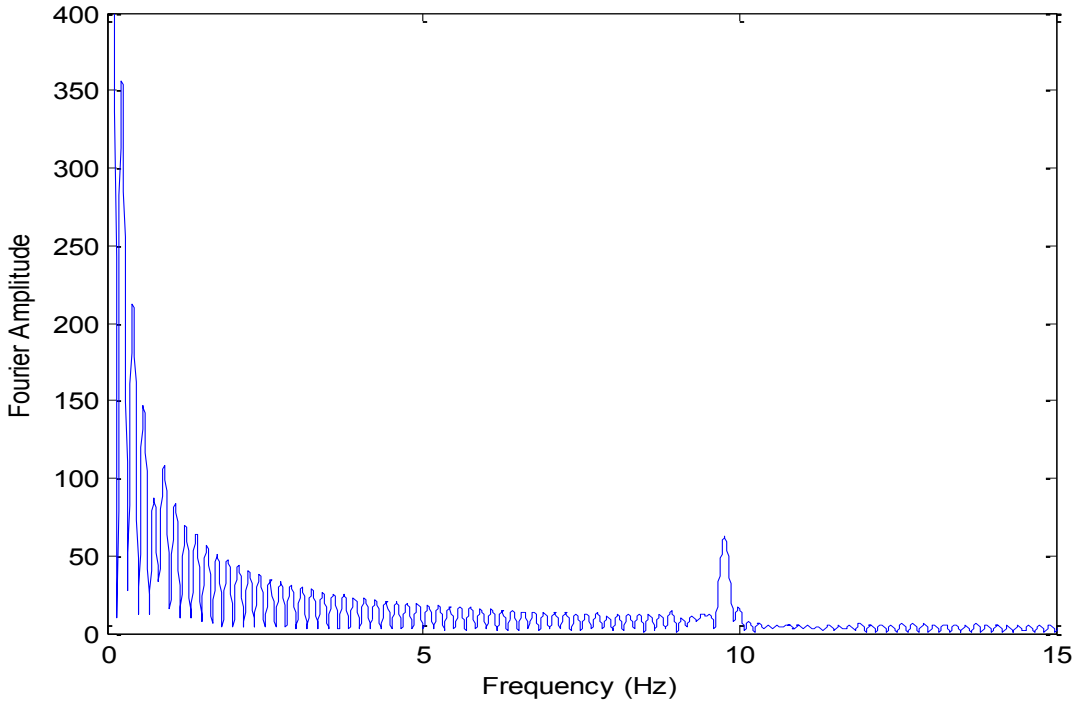

Figure 4.5 FFT analysis of cable tension at the right support

4.3.2 Eigenvalue and FFT analysis of the iced cable with 300 elements

Several scenarios with coarser mesh sizes such as 30, 100, 200, 300, 600 and 900 elements were studied to find out the optimum mesh size of a 300-m level span of CONDOR cable with an ice thickness of 25 mm. In conclusion, the 300-element case was chosen as optimum. This selection is based on different criteria such as: having mode shapes, frequencies up to 10 Hz and cable responses identical to that of refined mesh (1500 elements) and also having an acceptable level of bending stress (under 0.15 MPa) in the ice elements after the initial static analysis; i.e. in the range of the refined mesh which is under the yielding threshold value. The cable tension at the right-end support and the corresponding FFT function of this optimum mesh size are illustrated in Figure 4.6 and Figure 4.7, respectively. In addition, a comparison between refined mesh and optimum mesh frequencies is shown in Table 4.4.

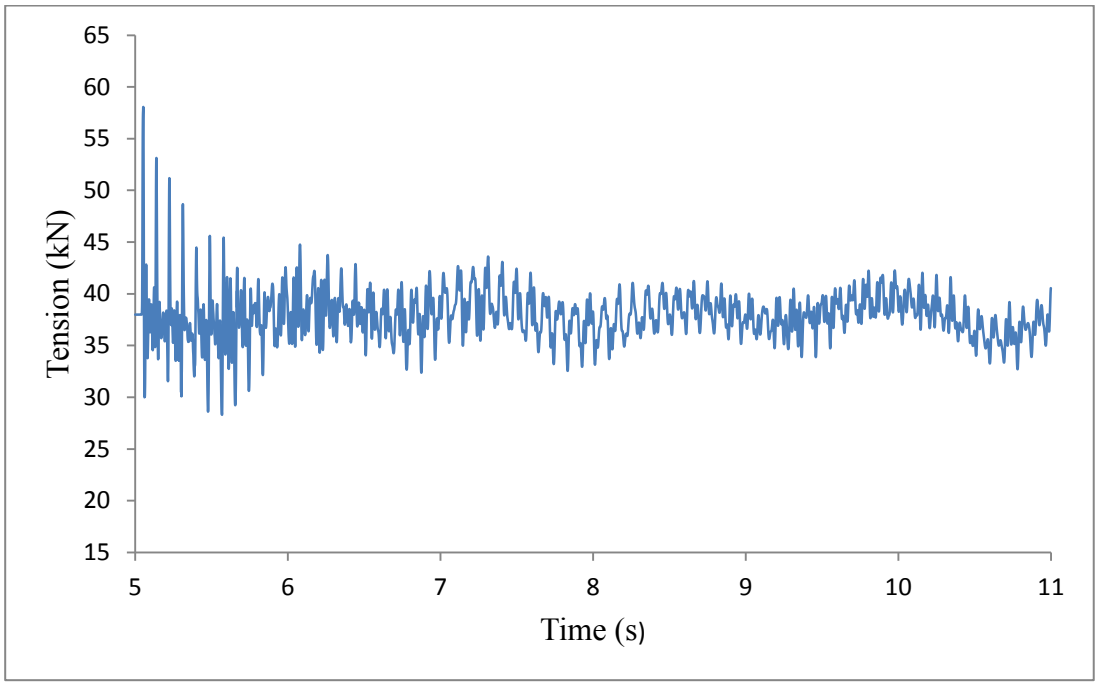

Figure 4.6 Cable tension at the right support

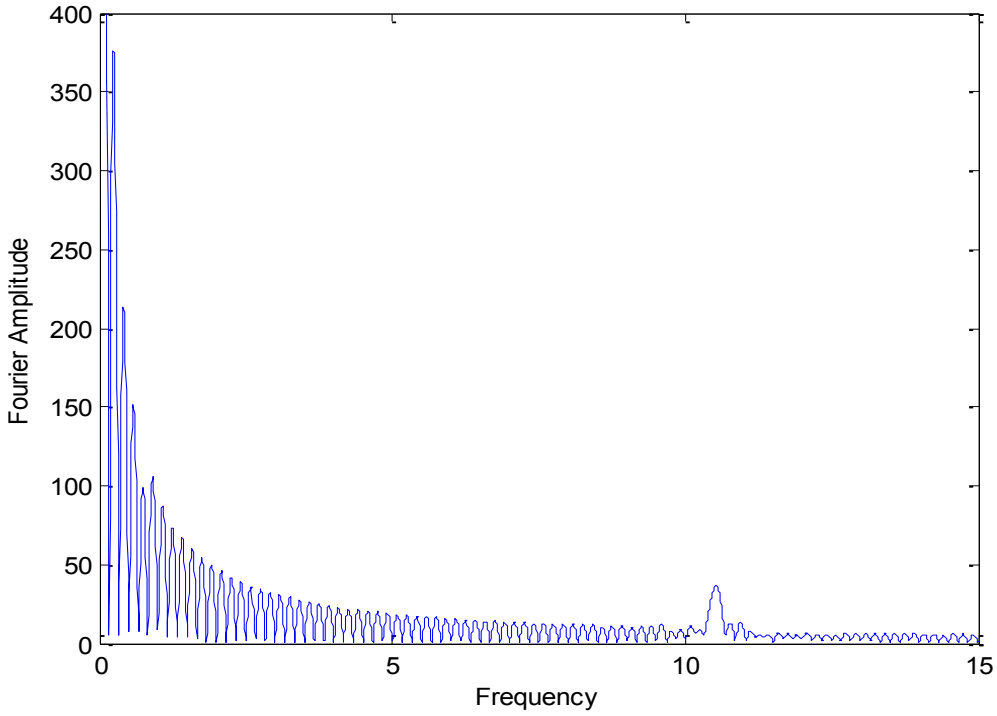

Figure 4.7 FFT analysis of cable tension at the right support

Table 4.4 Comparison of natural frequencies (in Hz) of 300 and 1500 element models

	Mesh size	
Mode	1500 elements	300 elements
1st asymmetric	0.27	0.27
1st symmetric	0.39	0.39
2nd asymmetric	0.55	0.55
2nd symmetric	0.66	0.66
	...	
33rd asymmetric	9.8	9.7
33rd symmetric	10.0	9.9

4.4 Conclusion

Numerical studies have shown that it is feasible to implement the new ice failure criterion based on maximum effective plastic strain to single-span real scale overhead lines. Furthermore, an optimum mesh size of a real scale iced conductor was found which will significantly reduce the computational efforts in a complex transmission line model with iced conductors.

5. Numerical simulations of a realistic line section subjected to cable ruptures

5.1. General considerations

Following the improved performance of the new failure criterion of the ice deposits based on the plastic strain limits discussed in preceding chapters, in this section the improved criterion is applied to a case study of a Hydro-Québec 120 kV two-circuit line section that failed during an ice storm event in the spring of 1997. The failure was due to conductor rupture in two phases and its dynamic effects have been modeled in details by Lapointe (2003). Photographs of damaged line section are shown in Appendix B. The objective of the present application is to determine whether the shock due to conductor rupture was sufficient to induce ice shedding in the spans adjacent to the breakage point.

As will be explained next, some adjustments are needed to Lapointe's model for the study of ice shedding effects. The line section model is composed of five suspension structures and two dead-end structures for a total of six spans. The dead-end structures are considered to be completely rigid. The broken conductors and dead end structures are shown in the Figure 5.1. The line conductors have been loaded with 25 mm of radial ice. Two types of suspension lattice steel towers (named BOC_3 and BOC_6) were modeled in details: Table 5.1 summarizes the main characteristics of the towers. Cable spans are numbered from left to right on Figure 5.1. Table 5.2 lists the span lengths and differences in elevation at cable suspension points.

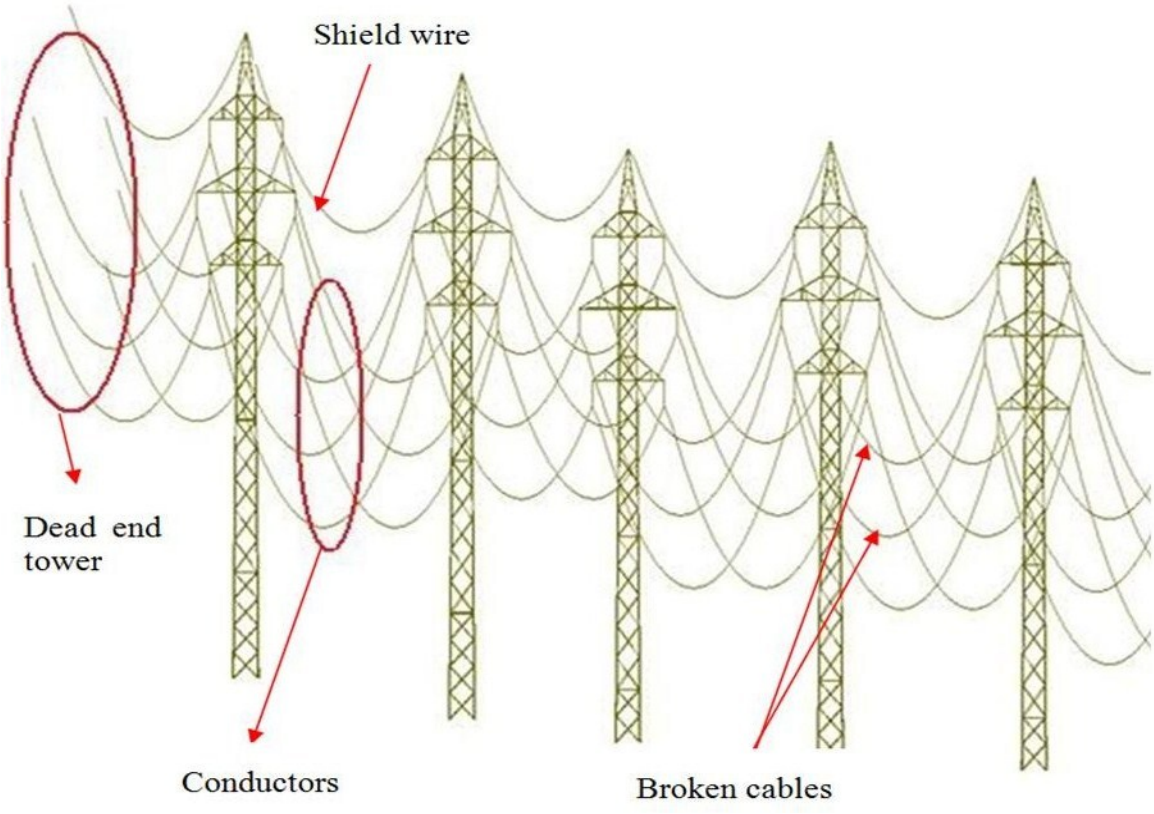

Figure 5.1 Line section modelled

Table 5.1 Suspension structures characteristics (Lapointe 2003)

Material	■ Steel: ACNOR G40.21 300 W ■ Density: 8125 kg/m^3 ■ Modulus of elasticity: 200E+9 Pa ■ Poisson ratio: 0.3
Members	■ Legs: Cold-formed equal-leg angle sections ■ Others: Hot-rolled angle sections
Assembly	■ Bolted connections
Structure height	■ BOC_3: 33.5 m ■ BOC_6: 36.5 m

Table 5.2 Span lengths and conductors suspension point elevations

Span	1	2	3	4	5	6
Length (m)	334.6	334.6	332.7	272.9	355.3	290.7
Δh (m)	0	-2	-4.5	1	-2	-2

The conductors are 54/7 CONDOR ACSR stranded cables. Shield wire and conductor properties are summarized in Table 5.3. The conductors are attached to the towers by insulator strings of 1.4 m in length and 40 kg in weight.

Table 5.3 Conductor and shield wire properties (Lapointe 2003)

	Conductor	Shield wire
Name	CONDOR	CDG12C
Type	ACSR	Galvanized steel stranded cable
Diameter (mm)	27.8	12.6
Area (mm^2)	455.1	96.5
Modulus of elasticity (MPa)	64500	178000
Mass per unit length (kg/m)	1.522	0.758
Weight per unit length (N/m)	14.93	7.44
Rated tensile strength (kN)	127	114
Initial horizontal tension (kN)	19.206	11.62

5.2 Previous studies and their limitations

Finite element modeling of transmission lines subjected to cable rupture was first done by Baenziger (1981) while more advanced techniques were introduced by McClure *et al.* (1987, 1989, 1991). The initial models were based on two-dimensions and McClure also studied three-dimensional models with realistic (yet approximate) modeling of supports. However, such 3D models were quite demanding on computational resources and further developments had to wait for more technological progress in Lapointe (2003) and McClure (2002, 2003). In three-dimensional models the torsional flexibility of suspension structures could also been taken into the account in simulations of line response to cable rupture in exterior phases. Ice shedding effects were not meant to be studied in these models and the ice loads were simply considered by using increased density cables. However, in this work, the objective is to simulate the progression of ice shedding in the iced cables adjacent to the ruptured cables. Separate modeling of the ice accretion following the procedure presented in Chapters 3 and 4 is therefore implemented in the line section model. To limit the computational effort, ice-beam elements have explicitly been considered in two spans adjacent to the ruptured cables, i.e. span#3 and 4, while ice in all the other spans is modeled using the increased density scheme. The improved failure criterion based on maximum plastic strain is used. The comparison between the results considering ice shedding with the previous ones from Lapointe (2003) is presented next.

5.3 Modeling the cable rupture

In this section, all the modeling considerations related to damping, static analysis, dynamic analysis, ice failure criterion and so on will be discussed, keeping in mind that the models are adapted from Lapointe (2003).

5.3.1 Modeling considerations

The line section comprises six conductors, one shield wire, 30 insulator strings, five suspension structures and ice-beam deposits in particular spans. The towers have been modeled in the same way as in Lapointe (2003). The same mesh of 30 increased density two-node isoparametric truss elements has been used to model all conductors and shield wires except in those two spans (#3 and 4) adjacent to ruptured cables were ice deposits are explicitly considered; they are shown in red in Figure 5.2. Based on the results discussed in Chapter 4, the mesh for these two spans comprises 300 two-node isoparametric truss elements and 298 3-D two-node isoparametric beam elements with rectangular cross section in parallel to each cable element are used to model the accreted ice on the conductors. In order to prevent spurious stiffening of the system caused by fixed rotational degrees of freedom at the suspension points, ice elements are omitted at each cable end.

Figure 5.2 is a simplified sketch of the three-dimensional model where the suspension structures are illustrated by simple stick structures. However, as it was shown in Figure 5.1, the detailed lattice towers have been modelled in ADINA. The X, Y and Z axes correspond to the transverse, longitudinal and vertical directions, respectively. The dead end structures are drawn with dashed lines and are represented by fixed nodes at the cable

attachment points. Starting from the left end of the line section, the suspension towers are numbered sequentially from #1 to #5.

Table 5.4 shows the equivalent density for bare and iced (increased density due to 25-mm thickness) conductor and shield wire. As mentioned before, except for those four conductor cables explicitly considered with ice-beam deposits, the rest of the conductors and shield wires are assumed with increased density throughout the analysis, which means that they will not be allowed to shed ice.

Table 5.4 Equivalent density for the cables

Cable type	Equivalent density (kg/m^3)	
	Conductor	Shield wire
Bare cable	3344	7859
Increased density due to ice	10966	34291

For the explicit ice-beam deposits the second moment of area and cross-sectional area of the rectangular beam are set as equivalent to those of an idealized cylindrical round shape with equivalent width (W) and depth (D) (Table 5.5).

Table 5.5 Dimensions and mass of the ice-beam elements

Ice thickness	Cross section of ice accretion (W x D)	
T_{ice} [mm] (Mass per unit length)	W [mm]	D [mm]
25 (3.73 kg/m)	71.55	57.66

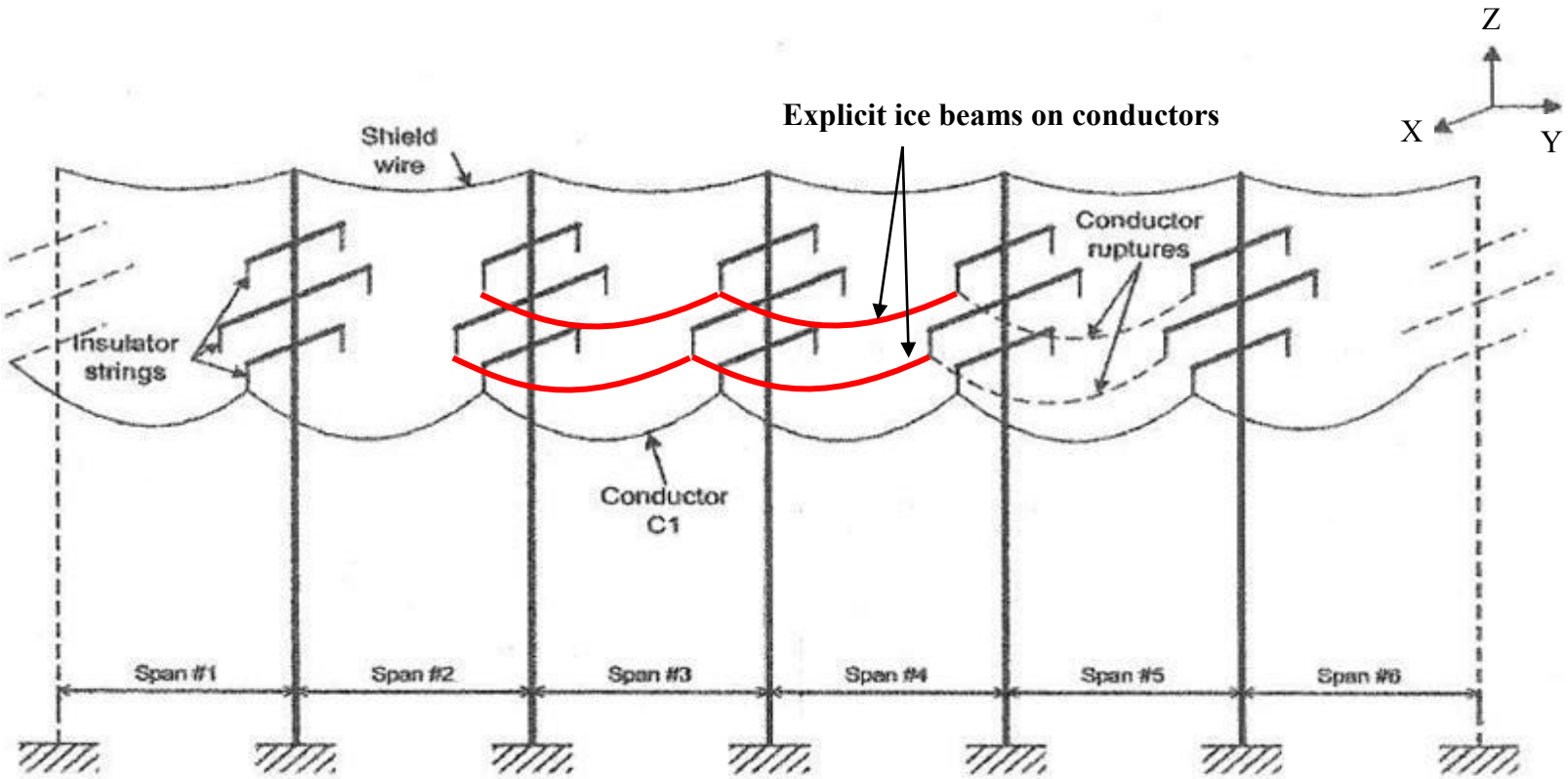

Figure 5.2 Detailed Model

Glaze ice failure modelling

Failure of the ice beam representing the glaze ice deposit accreted on the cable is modeled using the same procedure as in Chapter 3. The rupture of the beam ice deposit is defined in terms of a maximum allowable effective plastic strain (ε_p). Whenever this maximum strain criterion is fulfilled at any integration point of the ice beam element, the ice element detaches from the cable for the remainder of the analysis.

Damping

In this study, based on satisfactory results obtained in previous works (Jamaleddine *et al.* 1993, McClure and Lapointe 2003, Kálmán 2007) the aerodynamic damping is neglected and only axial structural damping of the iced-cable is considered. Damping is modeled by using a viscous dashpot in parallel to each cable element. The damping constant is set to represent an equivalent viscous damping of 10% critical (Lapointe 2003). This amount of damping is deemed to represent the effect of fractured ice deposits and likely exceeds the amount of internal cable damping that exists in the reality, however as it helps getting better and faster convergence of the dynamic analysis, it is the value used in this study. The damping constants are calculated from Equation 2 where ξ is the damping ratio, A the cross-sectional area, E the modulus of elasticity and μ is the mass per unit length of the cable (Lapointe 2003) and are given in Table 5.6. As it was explained in Chapter 3 numerical damping is also used to filter out spurious high frequencies of the response due to finite element discretization; it is introduced using the Newmark integration method with parameters δ and α set to 0.55 and 0.3, respectively (McClure and Guevara 1994).

[2] $C = 2\xi\sqrt{AE\mu}$

Table 5.6 Damping Constants

Ice thickness (mm)	Damping ratio (%)	Damping constant "c" (N*s/m)	
		Conductor	Shield wire
25	10	2421	1508

5.3.2 Static analysis

As mentioned before, the model combines two different types of iced-cable elements: the increased density 3-D truss cable and the explicit ice-beam element in parallel with the 3-D truss cable with bare density. In the first case, the bare cable geometric profile is calculated using the inextensible catenary equation. Then the resultant nodes are input in ADINA and the cable density is changed to its equivalent iced cable density. In the second case, the iced cable profile is first estimated using the inextensible catenary equation and then input in ADINA; this procedure decreases the level of initial stress in iced-beam elements and prevents their spurious shedding. A static analysis of this initial profile in ADINA results in a relaxed final static profile accounting for cable-ice elasticity. Finally, the deformed profile defines the position of the nodes connecting the ice-beam elements.

This two-step initial static analysis of the ice-beam/cable composite is highly nonlinear and getting convergence is cumbersome. In ADINA it is possible to define different degrees of freedom during consecutive static and dynamic analyses. Therefore, the Y and

Z rotational degrees of freedom (see Figure 5.2) are fixed for explicit ice-beam elements in static analysis to facilitate convergence. Also a force tolerance is specified as convergence criterion with FTOL=1000. However, to validate the quality of the equilibrium convergence, the final results of the output file were investigated and residual imbalances in the forms of ETOL (energy tolerance) and DTOL (Displacement tolerance) were found smaller than 10E-8 and 10E-6, which are acceptable limits.

5.3.3 Dynamic analysis

Dynamic analysis starts from the final static profile obtained for the iced cable by using the *restart* option in ADINA. Incremental equilibrium for static analysis is completed in 100 steps (arbitrarily set to 0.1 s each) so that dynamic analysis is started at time t = 10 s and continues for a total duration of 7 s. To be able to compare the results with those of Lapointe (2003), the same time increment of 1.5 ms was used and found appropriate for the mesh selected, while finer time steps would be implemented automatically whenever required by activating the *ATS* (automatic time-stepping) option in ADINA, as discussed in Chapter 3. Also to achieve high-frequency filtering of time history plots a smaller time step was implemented, as will be discussed in section 5.4. A lumped mass formulation is used. Energy and displacement tolerances are specified; the energy tolerance is assigned a value of ETOL=10E-8 and the displacement tolerance is DTOL=10E-5. All rotational degrees of freedom are activated for the explicit ice-beam elements in dynamic analysis.

5.4 Results

The results from nonlinear dynamic analysis using three-dimensional models and their comparison with Lapointe's results (2003) are discussed in this section.

5.4.1 General

Figure 5.3 identifies the different conductors labelled C1 to C6, and the different cross arm levels (CL) including the uppermost (CL_U), median (CL_M) and lowest (CL_L) cross arm pairs. The two broken conductors are C3 and C5, in span#5 (see Figure 5.2).

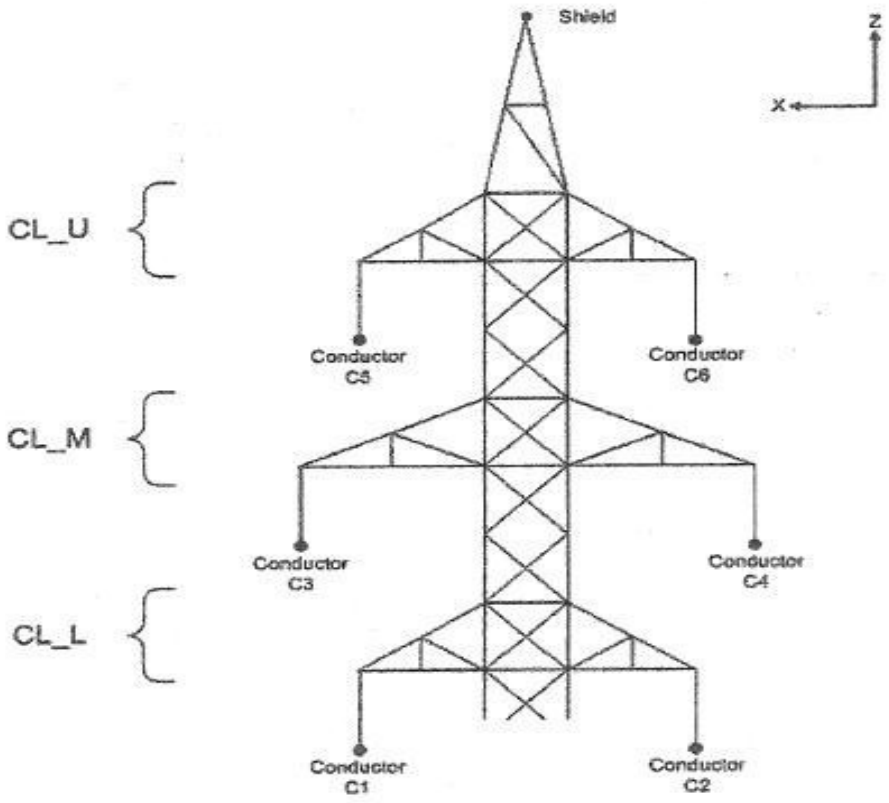

Figure 5.3 Conductors and cross arm levels (Lapointe 2003)

Following the cable ruptures, all explicit ice-beam elements are detached from the conductors in spans #3 and #4, i.e. the RIS (rate of ice shedding) is 100%. De-icing is almost instantaneous: it takes 131 ms to deice C3 conductor in span#4 (immediately adjacent to cable ruptures) and 133 ms to deice C5 conductor. In span#3, the values are 283 ms and 284 ms, respectively. The time taken by the shock wave in C3 and C5 to reach the fixed end on the left side (Figure 5.2) is 358 ms. As a result, the wave speed "c" is estimated at 5365 m/s.

5.4.2 Eigenvalue analysis

Performing eigenvalue analysis prior to any dynamic analysis is important since unrealistic natural frequencies and mode shapes are good trouble shooters. Therefore, eigenvalue analysis was conducted on this model in its final static configuration using the subspace iteration method in ADINA. Figure 5.4 shows the first mode with frequency equal to 0.14 Hz. Span 5 will receive the most effect under this frequency as it is the longest span and tower deformations do not contribute significantly. Figure 5.5 shows an example of an intermediate frequency mode (dominant in Span 3) with a value f = 0.64 Hz.

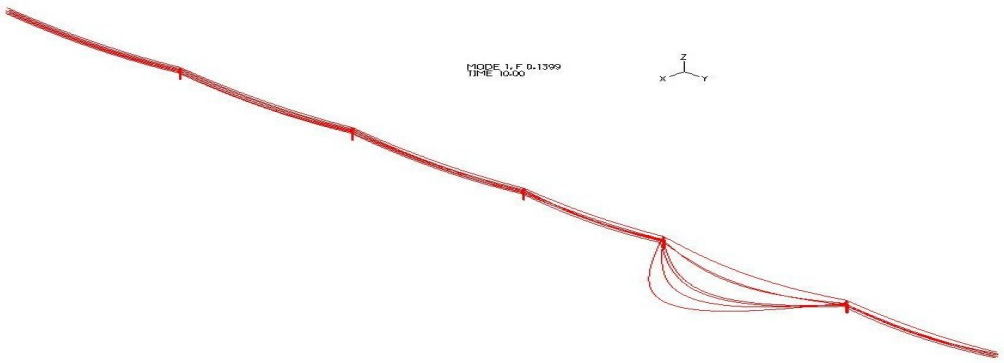

Figure 5.4 Mode one (the lowest frequency at 0.14 Hz)

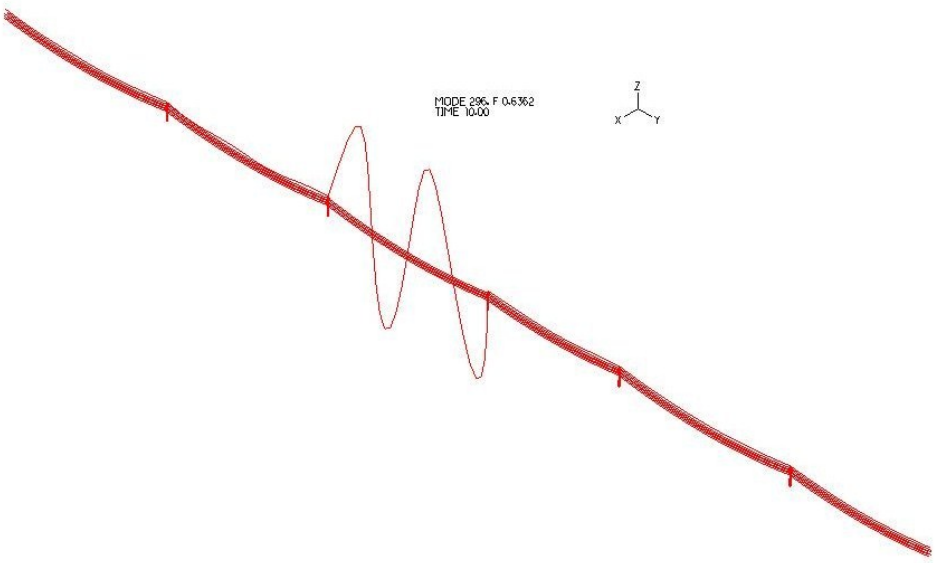

Figure 5.5 An intermediate frequency mode (0.64 Hz)

Figure 5.6 shows one of the high frequency modes with a value equal to 2.03 Hz. As it appears in the figure there are transverse shapes in all the spans and displacements in spans 3 and 4 have higher amplitudes. There is also a vertical motion in spans 3 and 4 which does not appear unless the ice beams are modeled. It should also be mentioned that the towers deflect significantly in this mode along the transverse direction.

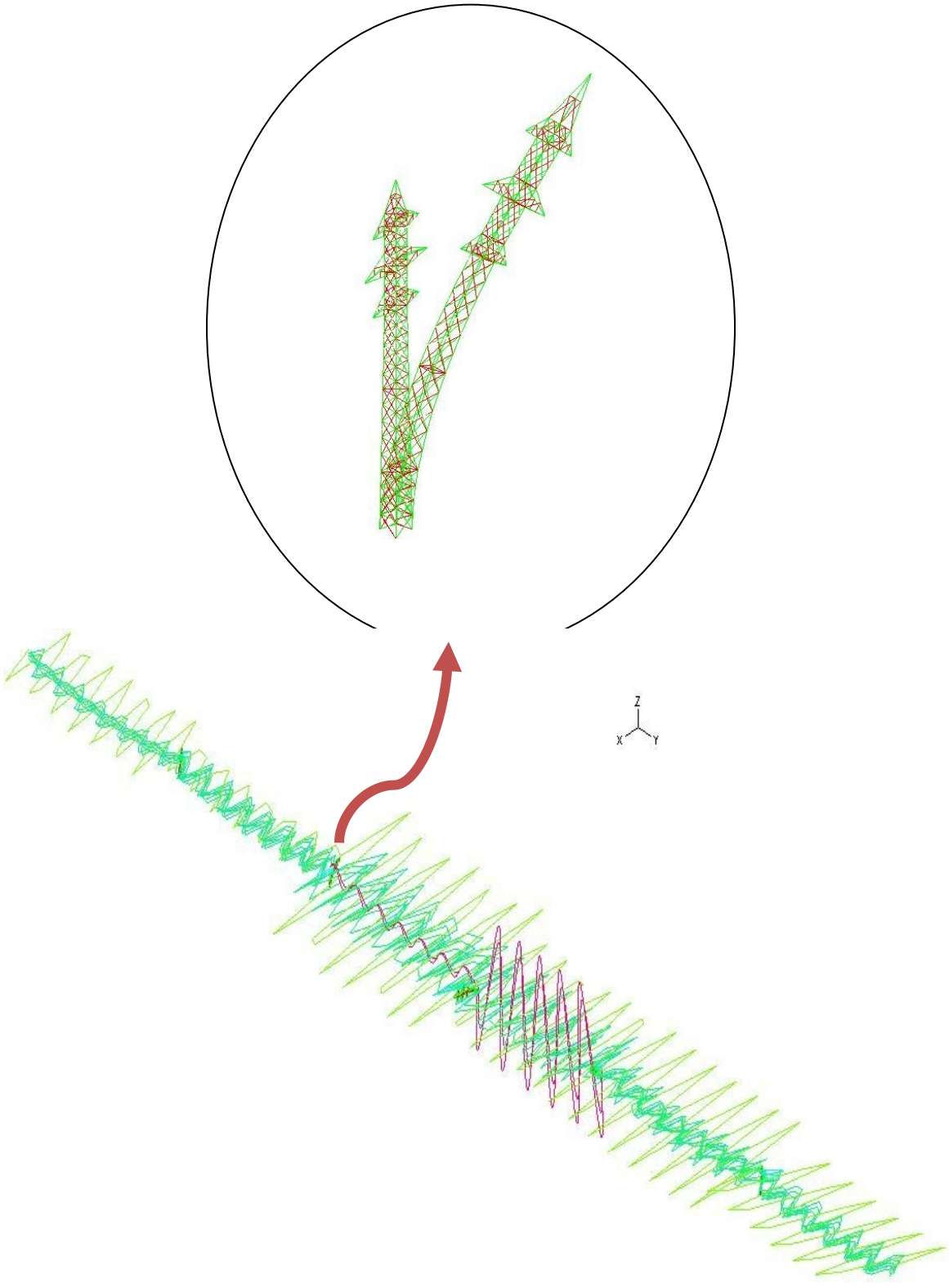

Figure 5.6 A high frequency mode (2.03 Hz)

5.4.3 Conductor and shield wire tensions

Cable tensions at all suspension points are tabulated in this section and compared with previous results obtained by Lapointe (2003). The same conductor and shield wire labelling convention is used in this study; a conductor element tension is referred to the tension calculated in the first conductor element located at the right of each suspension point. However, for the case of broken conductors C3 and C5 at structure#4, the tension refers to the elements at the left of the suspension point. For instance, the tension in conductor C2 at the suspension point Sp2 is referred to as the tension in conductor element Cond_C2_Sp2. The same procedure is repeated for shield wire elements. For example, at structure#2, the reported shield wire tension is referred to Shield_Sp2. The cables at the end structures are named deadend_R and deadend_L (right and left). Therefore, the tension in the conductor C3 at the leftmost anchor point is referred to Cond_C3_deadend_L.

Table 5.7 shows initial and peak wire tension values (T_1, T_{max}) as well as the time delay (t_d), i.e. the shock wave travel time to reach the point. The impact factor (IF) is the ratio of the maximum tension to the initial tension. For a more convenient comparison between the results, the values obtained by Lapointe are listed in parentheses beside the values generated in this study.

Table 5.7 Conductor and shield wire tensions

Element	t_d(ms)	T_1(kN)	T_{MAX}(kN)	IF
Conductor C1				
Cond_C1_deadend_L	385 (461)	53.5	62.9 (67.5)	1.2
Cond_C1_Sp1	265 (341)	53.6	58.5 (63.5)	1.1
Cond_C1_Sp2	126 (209)	53.6	62.1 (64.0)	1.2
Cond_C1_Sp3	75 (95)	52.8	57.9 (59.0)	1.1
Cond_C1_Sp4	3 (5)	53.3	63.2 (64.0)	1.2
Cond_C1_Sp5	2 (8)	52.3	57.2 (60.5)	1.1
Cond_C1_deadend_R	95 (98)	52.6	62.5 (64.0)	1.2
Conductor C2				
Cond_C2_deadend_L	389 (455)	53.5	60.6 (60.5)	1.1
Cond_C2_Sp1	269 (323)	53.6	56.4 (57.5)	1.1
Cond_C2_Sp2	157 (203)	53.6	59.7 (59.0)	1.1
Cond_C2_Sp3	68 (89)	52.8	55.7 (55.5)	1.1
Cond_C2_Sp4	2 (5)	53.3	59.9 (59.0)	1.1
Cond_C2_Sp5	2 (5)	52.3	55 (55.5)	1.1
Cond_C2_deadend_R	83 (95)	52.6	60.2 (59.0)	1.1
Conductor C3				
Cond_C3_deadend_L	358 (413)	53.5	86.9 (95.0)	1.6
Cond_C3_Sp1	238 (299)	53.6	77.8 (85.0)	1.5
Cond_C3_Sp2	134 (179)	53.6	62.2 (83.0)	1.2
Cond_C3_Sp3	51 (68)	52.8	52.8 (68.0)	1.0
Cond_C3_Sp4	0 (0)	53.3	51.0 (80.0)	1.0
Cond_C3_Sp5	0 (0)	52.3	78.8 (80.0)	1.5
Cond_C3_deadend_R	66 (71)	52.6	96.2 (95.0)	1.8
Conductor C4				
Cond_C4_deadend_L	382 (440)	53.5	63.6 (62.5)	1.2
Cond_C4_Sp1	260 (326)	53.6	57.0 (62.0)	1.1
Cond_C4_Sp2	155 (206)	53.6	62.3 (58.0)	1.2
Cond_C4_Sp3	68 (89)	52.8	57.0 (60.0)	1.1
Cond_C4_Sp4	2 (2)	53.3	62.1 (56.0)	1.2
Cond_C4_Sp5	2 (2)	52.3	55.6 (61.0)	1.1
Cond_C4_deadend_R	89 (95)	52.6	63.3 (56.5)	1.2

Conductor C5				
Cond_C5_deadend_L	358 (422)	53.5	101.1 (100.0)	1.9
Cond_C5_Sp1	241 (299)	53.6	76.3 (85.0)	1.4
Cond_C5_Sp2	133 (176)	53.6	65.6 (86.0)	1.2
Cond_C5_Sp3	51 (68)	52.8	52.8 (64.0)	1.0
Cond_C5_Sp4	0 (0)	53.3	62.2 (88.0)	1.2
Cond_C5_Sp5	0 (0)	52.3	77.0 (79.0)	1.5
Cond_C5_deadend_R	66 (71)	52.6	90.8 (100.0)	1.7
Conductor C6				
Cond_C6_deadend_L	383 (449)	53.5	67.4 (67.5)	1.3
Cond_C6_Sp1	263 (326)	53.6	59.2 (62.5)	1.1
Cond_C6_Sp2	151 (200)	53.6	65.6 (64.0)	1.2
Cond_C6_Sp3	66 (86)	52.8	58.7 (58.0)	1.1
Cond_C6_Sp4	2 (2)	53.3	66.1 (65.0)	1.2
Cond_C6_Sp5	2 (2)	52.3	57.7 (59.0)	1.1
Cond_C6_deadend_R	84 (92)	52.6	67.1 (67.0)	1.3
Shield wire				
Shield_deadend_L	401 (470)	38.1	54.5 (58.0)	1.4
Shield_Sp1	248 (338)	38.1	47.0 (48.0)	1.2
Shield_Sp2	154 (212)	38.3	60.8 (52.5)	1.6
Shield_Sp3	71 (85)	36.3	57.3 (54.0)	1.6
Shield_Sp4	2 (8)	38.3	78.5 (80.0)	2.0
Shield_Sp5	3 (8)	38.1	62.7 (64.0)	1.6
Shield_deadend_R	98 (100)	36.6	76.4 (80.0)	2.1

The general trend is the same as observed in Lapointe's study without ice shedding: broken conductors C3 and C5 have higher IF values than the intact conductor spans and higher tensions are simulated at the dead-end structures. The impact factors of the shield wires are very large since these cables are directly anchored to the towers, without any suspension length to increase their slack. However, of main interest here is the effect of ice shedding on the simulated response following cable breakage. The results indicate that

the tension and IF values in broken conductors C3 and C5 in Sp2, 3 and 4 have significantly decreased (by 20 to 35%). These elements are located in the spans where ice shedding was allowed to take place.

The time history plots of tension in intact (C1) and broken (C5) conductors generated in this study (Figure 5.7 a) are compared to those obtained by Lapointe (Figure 5.7 b).

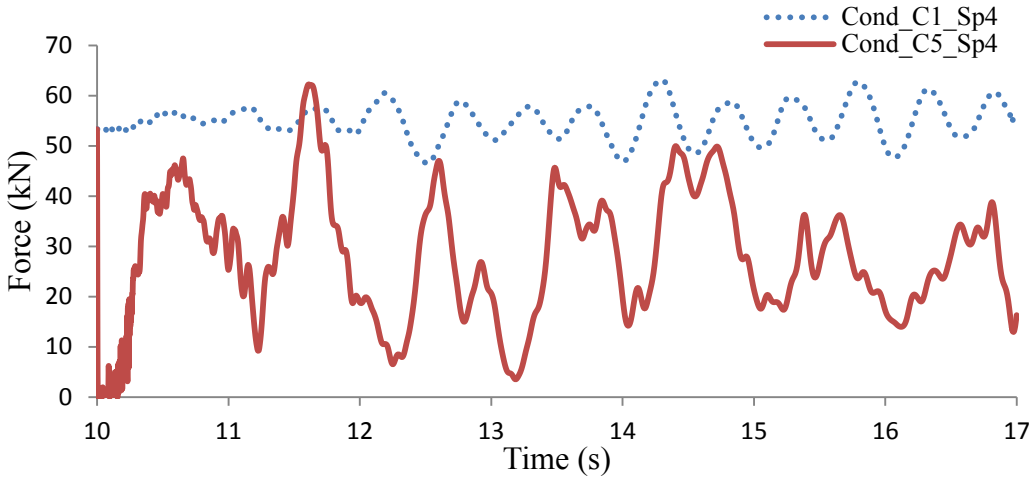

a) Current study with ice shedding in spans 3 and 4

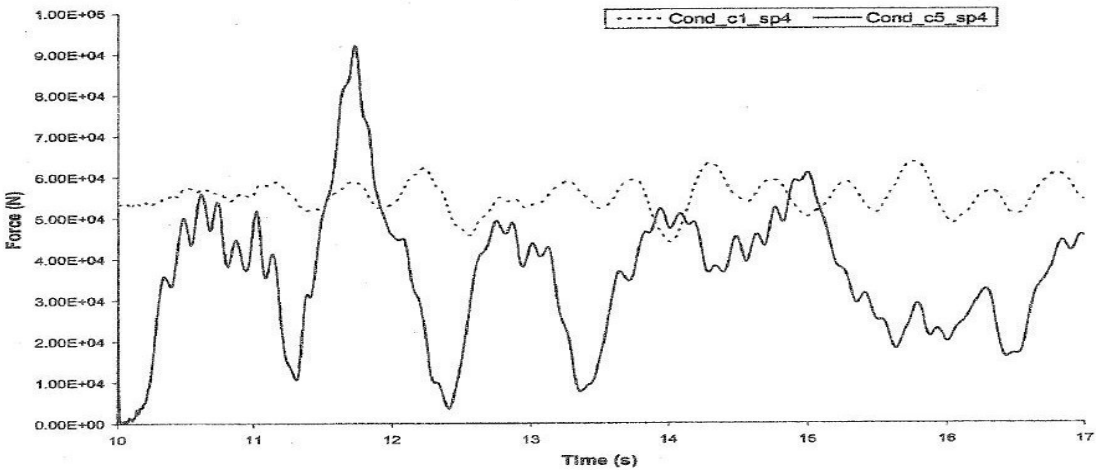

b) Previous study by Lapointe (2003)

Figure 5.7 Comparison of Tensions in Cond_C1_Sp4 and Cond_C5_Sp4

Both figures show the same trends. The time history plot of Cond_C5_Sp4 shows the initial conductor slackening following the rupture in Span 5, and then typical tension peaks, where the second peak is a maximum. The tension in Cond_C1_Sp4 oscillates around its initial value with an almost harmonic graph. The main difference between these two sets of results is the important reduction in the peak tension value of the broken conductor (Cond_C5_Sp4).

The tensions in the shield wires are large especially in the Shield_Sp4 and Shield_deadend_R. As an example, the time history plot of the tension in Shield_Sp3 is illustrated in Figure 5.8. The first peak has the maximum tension value. Also it should be mentioned that the maximum tensions do not exceed the cable rated tensile strength.

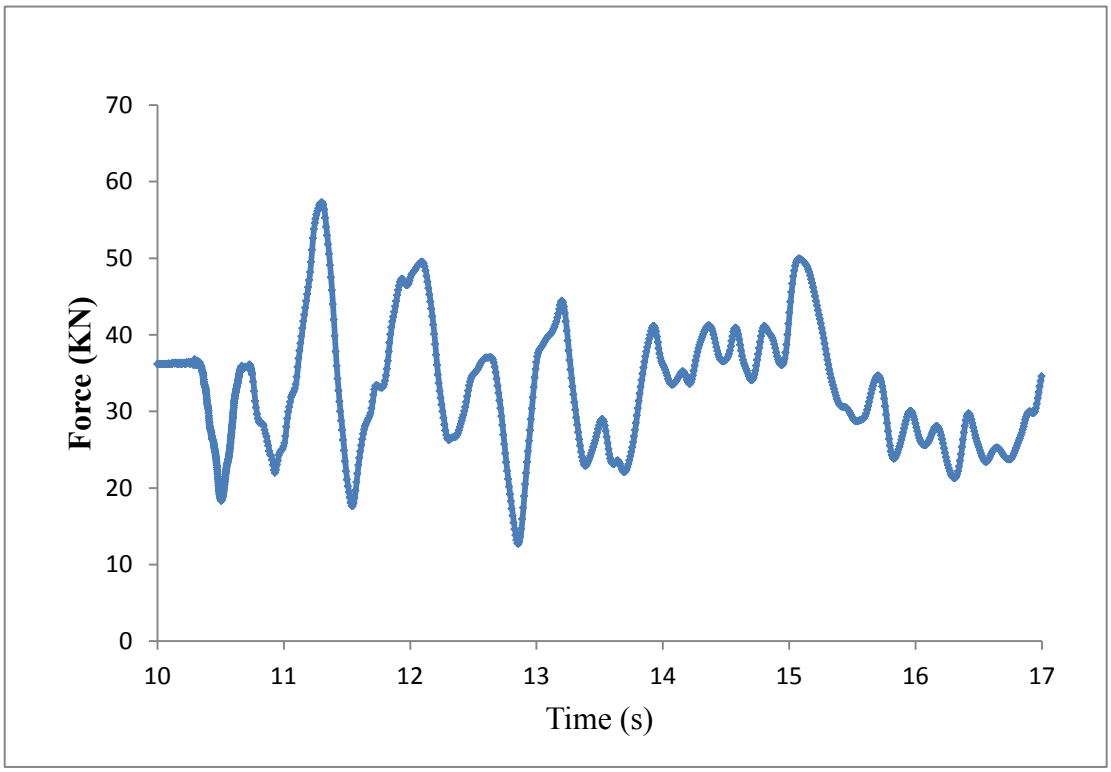

Figure 5.8 Tension in Shield_Sp3

5.4.4 Accelerations and displacements

To gain a better understanding of what causes ice shedding in a line subjected to cable rupture, accelerations and displacements has been monitored at different locations.

A) At mid span of broken conductor

Displacements and accelerations of a node at mid span#3 of conductor C3 are shown in Figure 5.9 and Figure 5.10, respectively. As expected the longitudinal displacement in Y direction is always negative and towards the left side of the line section following the cable ruptures. On the other hand, the vertical displacement in the Z direction oscillates around the final static profile and has a positive peak value (cable jump) of about 3 m.

Accelerations in Y and Z directions are significant, especially in the longitudinal direction of the sudden shock wave induced by cable breakage (Y axis). The time at which the ice element located at this mid span node detached from the conductor was found to coincide with the peak Y-acceleration time. Clearly, the ice shedding is caused by this very large peak in Y-acceleration. Although in practice, such acceleration is expected to be large, the author believes that the maximum peak value is over predicted by the finite model.

The conductor accelerations at mid span#1 of C3 and C5 (not shown here) have the same trend as in span#3. This suggests then that all the spans corresponding to the ruptured conductors C3 and C5 should experience complete ice shedding.

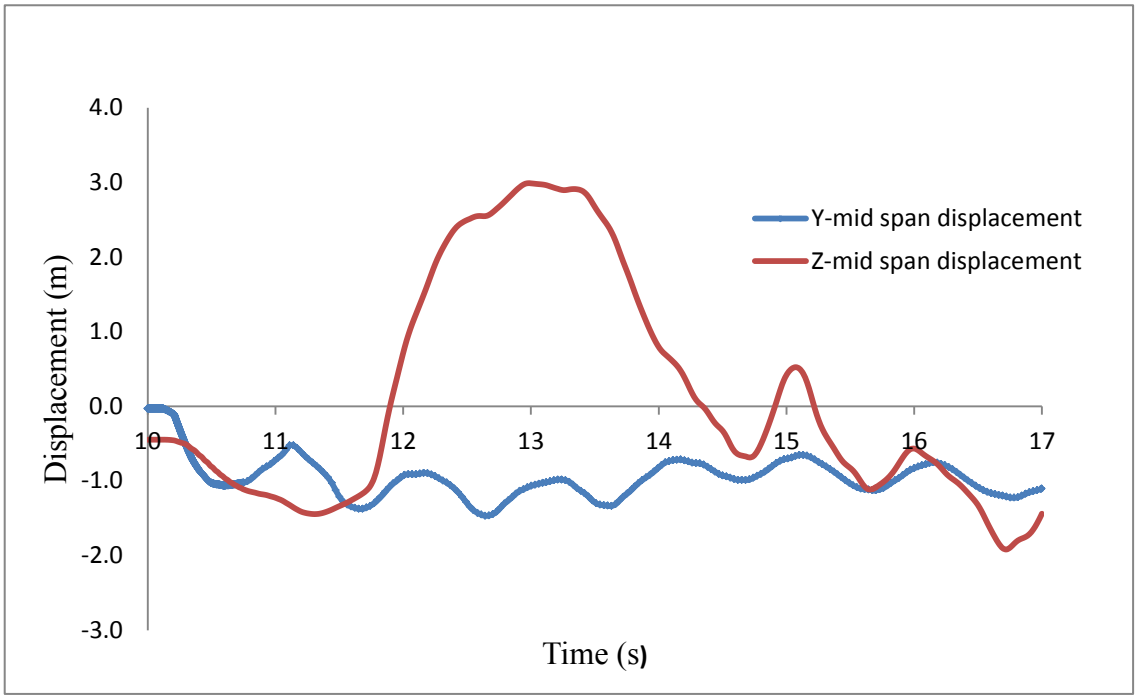

Figure 5.9 Displacement at mid span#3 of conductor C3

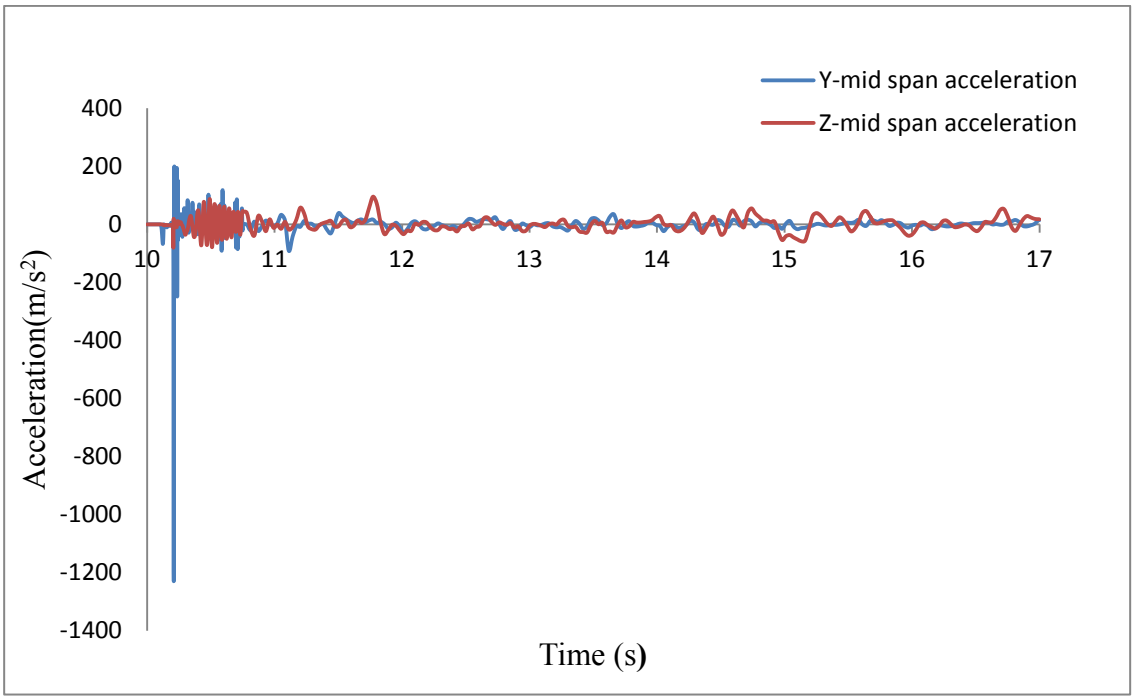

Figure 5.10 Acceleration at mid span#3 of conductor C3

B) Accelerations in intact spans

The time history plots of longitudinal (Y) and vertical (Z) accelerations of a node at mid span#1 of conductor C1 are illustrated in Figure 5.11. In this case, the trend is for the longitudinal acceleration to exceed the vertical, but the amplitudes are much smaller (all values are below 1 g) than in the spans of ruptured conductors. Therefore, ice shedding is not expected in intact spans even if explicit ice-beam elements were modeled.

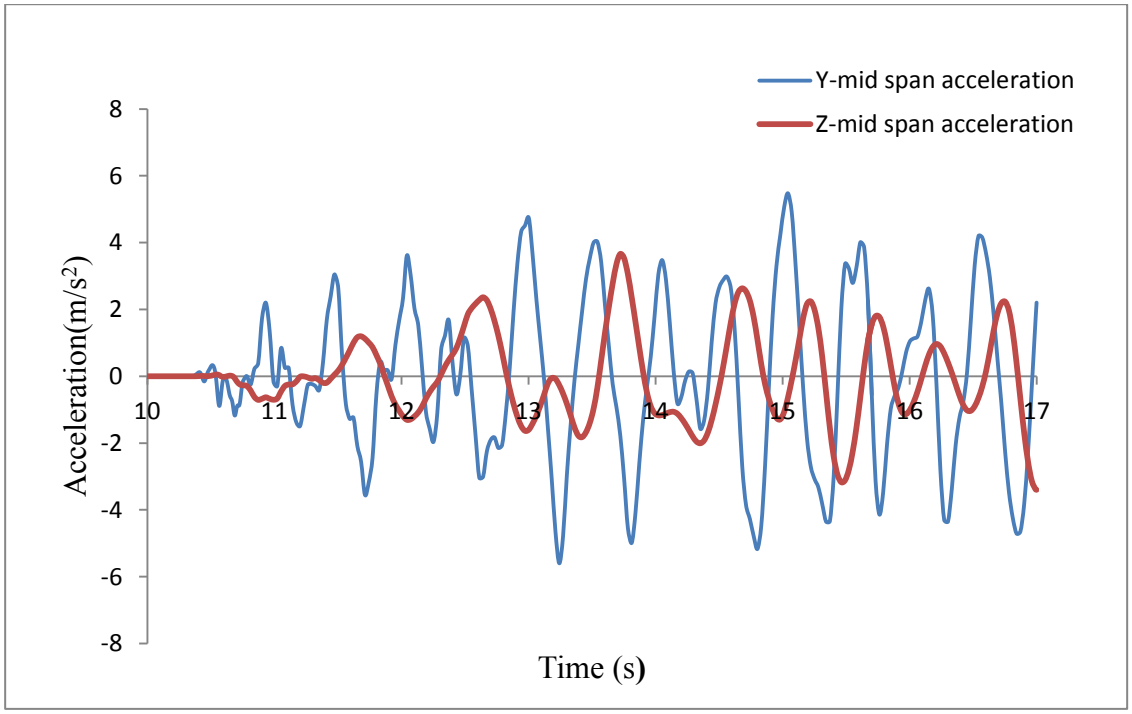

Figure 5.11 Accelerations at mid span#1 of conductor C1

C) Large accelerations in single span subjected to vertical impact load

To further investigate the source of the large initial accelerations predicted by the model of cable rupture, the single level span problem of Chapter 3 is revisited where the loading is specified as a vertical impact at mid span. Acceleration results of the 3rd ice shedding scenario at mid span and close to the supports in the Y and Z directions are illustrated in Figure 5.12 and Figure 5.13. Clearly, initial peak values are very large and of the same order as for the cable rupture problem (in the order of 100 g). Note that these large accelerations were predicted by the numerical model but were not measured in the physical tests.

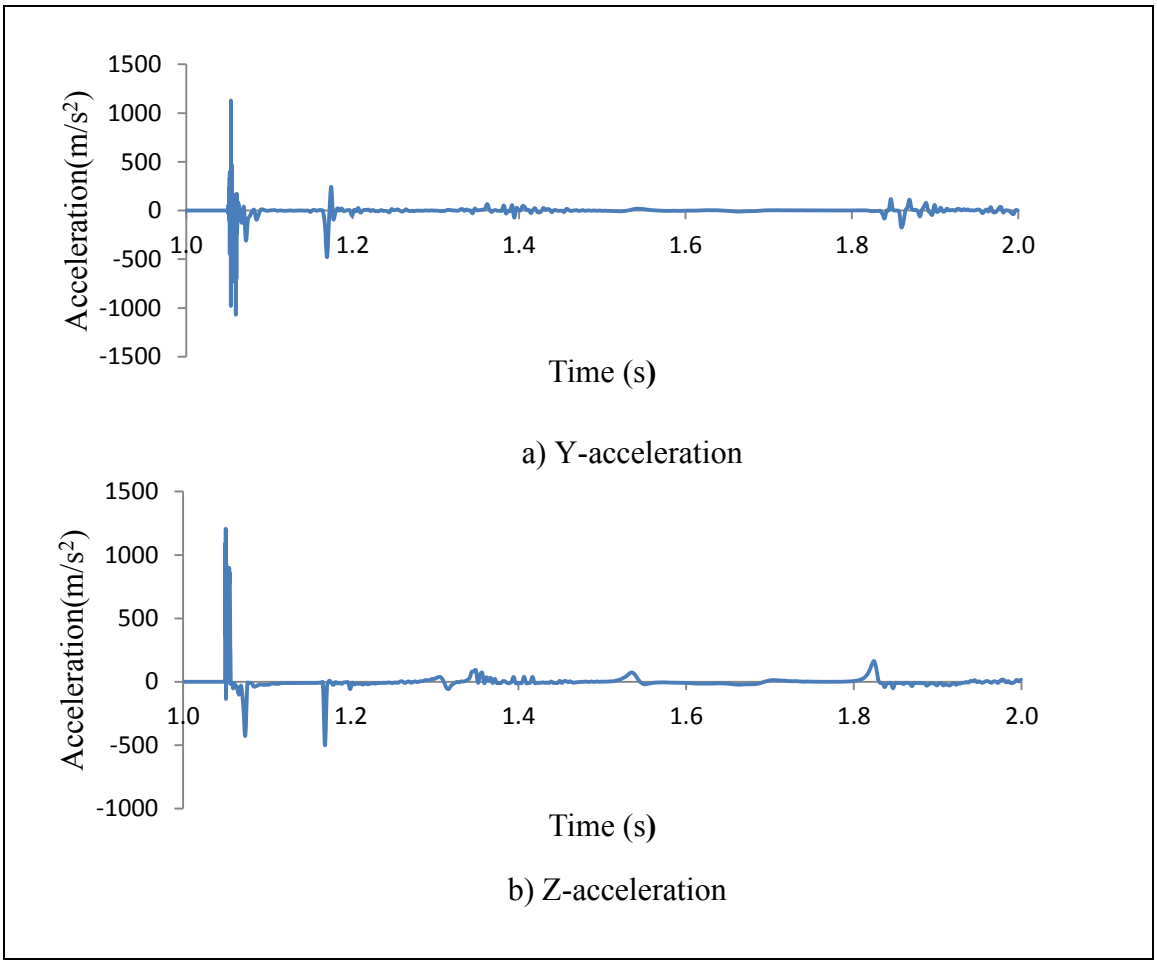

Figure 5.12 Accelerations at mid span in Y and Z directions

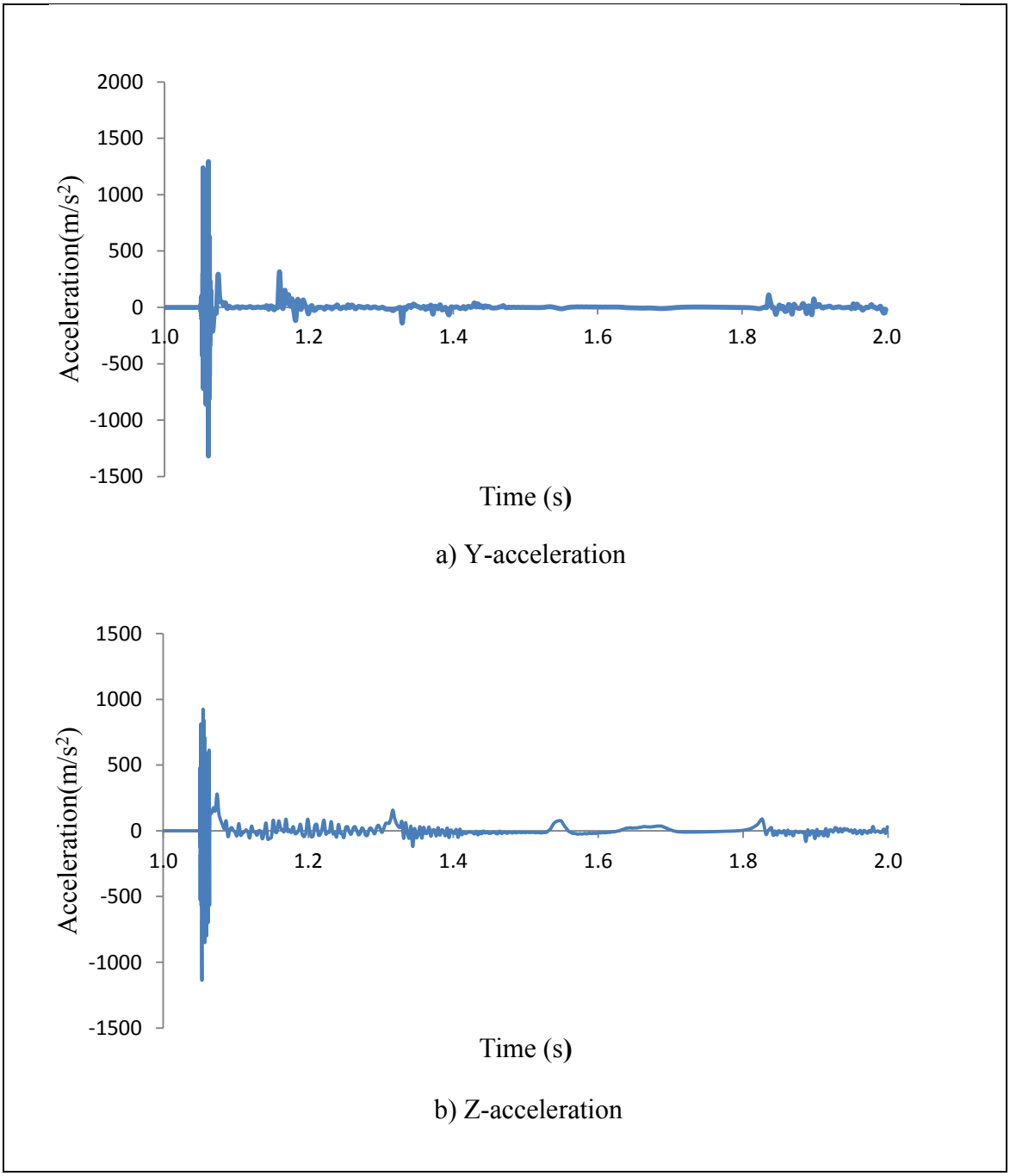

Figure 5.13 Accelerations close to the support in Y and Z directions

5.4.5 Insulator string tensions and rotations

Insulator string tensions and rotations (swing angles) obtained from the models are compared with the results in Lapointe (2003). To be able to compare the results, the same labelling convention is used in this study; all suspension points are labelled as Sp, for instance, all suspension points of structure#2 are labelled Sp2 followed by the appropriate conductor number. The initial tension force (T_1), the maximum tension force (T_{max}) and the impact factor (IF) are listed in Table 5.8. In addition, the maximum longitudinal rotation (θx Max) of the insulator strings is shown in the last column; the sign of this rotation agrees with the right-hand rule, i.e. a positive longitudinal rotation means the insulator swings toward the positive Y-axis direction. The results obtained by Lapointe (2003) are listed in parentheses.

Generally slightly larger insulator string tensions are obtained in the present study as compared to Lapointe's work (2003) which did not consider ice shedding. For the case of String_C3_Sp4 and String_C5_Sp4 the IF has decreased but overall ruptured conductors (C3 and C5) have larger tension values as compared to the intact conductors. And structure#5 is subjected to higher loads than structure#4.

Insulator strings attached to suspension structure#5 have higher rotations in the longitudinal direction if compared to Lapointe's results. However, those insulators located on structure#1 have lower rotations. Moreover, String_C3_Sp2 and String_C5_Sp2 have significantly higher rotations as compared to Lapointe's results (2003). As expected, longitudinal rotations have higher values in spans adjacent to ruptured conductors (C3 and C5) as compared to intact conductors.

Table 5.8 Insulator string tensions and rotations

Element	T1 (kN)	Tmax (kN)	IF	θx Max (degrees)
String_C1_Sp1	16.9	18.8 (19.5)	1.1	-5.4 (6.0)
String_C1_Sp2	17.0	20.8 (20.0)	1.2	8.1 (10.0)
String_C1_Sp3	14.1	16.9 (15.5)	1.2	-8.8 (-11)
String_C1_Sp4	16.1	19.2 (19.0)	1.2	19.4 (25.0)
String_C1_Sp5	16.1	19.0 (19.0)	1.2	-24.1 (-24.0)
String_C2_Sp1	16.9	17.9 (18.0)	1.1	-3.3 (-4.0)
String_C2_Sp2	17.0	20.0 (18.5)	1.2	4.6 (4.0)
String_C2_Sp3	14.1	16.7 (15.0)	1.2	-5.5 (-6.0)
String_C2_Sp4	16.1	20.8 (17.5)	1.3	7.4 (8.0)
String_C2_Sp5	16.1	18.0 (17.0)	1.1	-10.8 (-5.5)
String_C3_Sp1	16.9	29.1 (31.0)	1.7	-25.7 (-29.0)
String_C3_Sp2	17.0	30.0 (29.0)	1.8	-56.1 (-36.0)
String_C3_Sp3	14.1	25.8 (27.5)	1.8	-61.8 (-52.0)
String_C3_Sp4	16.1	50.8 (80.0)	3.2	-87.6 (-90.0)
String_C3_Sp5	16.1	77.0 (70.0)	4.8	99.2 (95.0)
String_C4_Sp1	16.9	18.2 (18.0)	1.1	-4.5 (-7.0)
String_C4_Sp2	17.0	20.0 (19.0)	1.2	5.6 (5.0)
String_C4_Sp3	14.1	15.6 (15.0)	1.1	-7.2 (-7.0)
String_C4_Sp4	16.1	19.1 (18.0)	1.2	9.4 (9.0)
String_C4_Sp5	16.1	18 (17.5)	1.1	-14.5 (-6.0)
String_C5_Sp1	16.9	28.2 (31.0)	1.7	-25.2 (-29.0)
String_C5_Sp2	17.0	28.9 (29.0)	1.7	-59.6 (-36.0)
String_C5_Sp3	14.1	35.7 (30.0)	2.5	-59.5 (-50.0)
String_C5_Sp4	16.1	63.1 (90.0)	3.9	-87.3 (-90.0)
String_C5_Sp5	16.1	78.0 (75.0)	4.8	94.1 (98.0)
String_C6_Sp1	16.9	19.0 (18.6)	1.1	-6.7 (-8.0)
String_C6_Sp2	17.0	21.0 (20.4)	1.2	8.8 (9.0)
String_C6_Sp3	14.1	18.0 (15.5)	1.3	8.3 (-10.0)
String_C6_Sp4	16.1	20.0 (19.3)	1.2	13.2 (15.0)
String_C6_Sp5	16.1	20.0 (17.7)	1.2	-19.9 (-10.0)

5.4.6 High-frequency filtering of time history plots

High frequencies are observed in the time history plots of all insulator strings of structure#5 and some of those located on the ruptured conductors such as String_C5_Sp3. These high frequencies are not realistic and appear to come from the numerical simulation of the mechanical shock caused by the conductor rupture. This hypothesis is examined next with a series of numerical experiments.

Fourier analysis of the time history in Figure 5.14 shows that the frequency content is normal below 25 Hz but the signal also contains high energy in the high frequency range between 70 and 600 Hz. Such high frequencies are associated with the modes of individual cable finite elements which are artificially generated by the shock load. This was confirmed by performing mode and frequency analysis on a few elements of the model in a separate ADINA file.

One of the ways to deal with these high frequency peaks is to eliminate them from the time history plots. For instance, tension at String_C3_Sp5 is illustrated in Figure 5.14 and the modified time history plot is shown in Figure 5.15 with a cut-off value of 25 Hz.

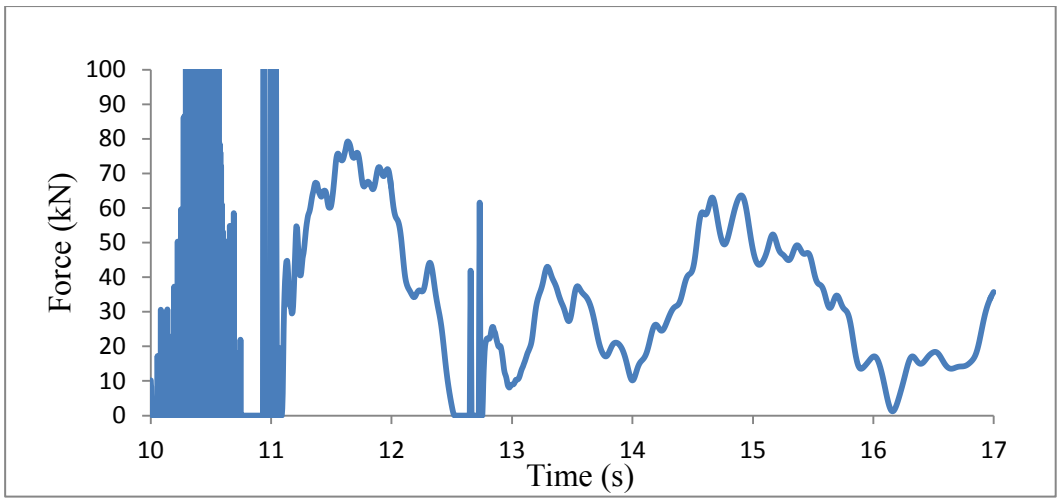

Figure 5.14 Tension at String_C3_Sp5 (raw data)

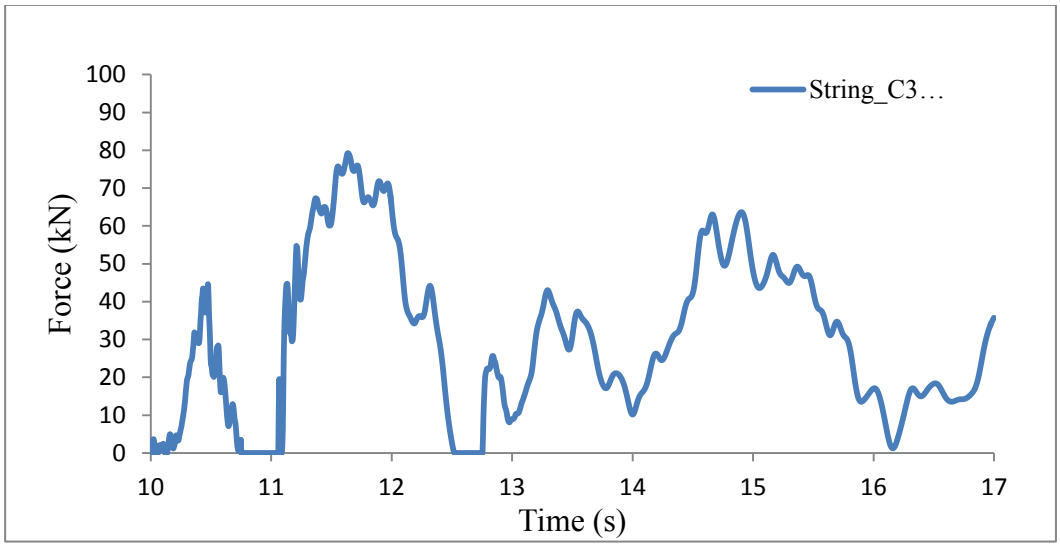

Figure 5.15 Tension at String_C3_Sp5 (filtered data)

Also Figure 5.16 shows tension at String_C5_Sp3 in which some high frequency peaks are observed after the cable becomes slack.

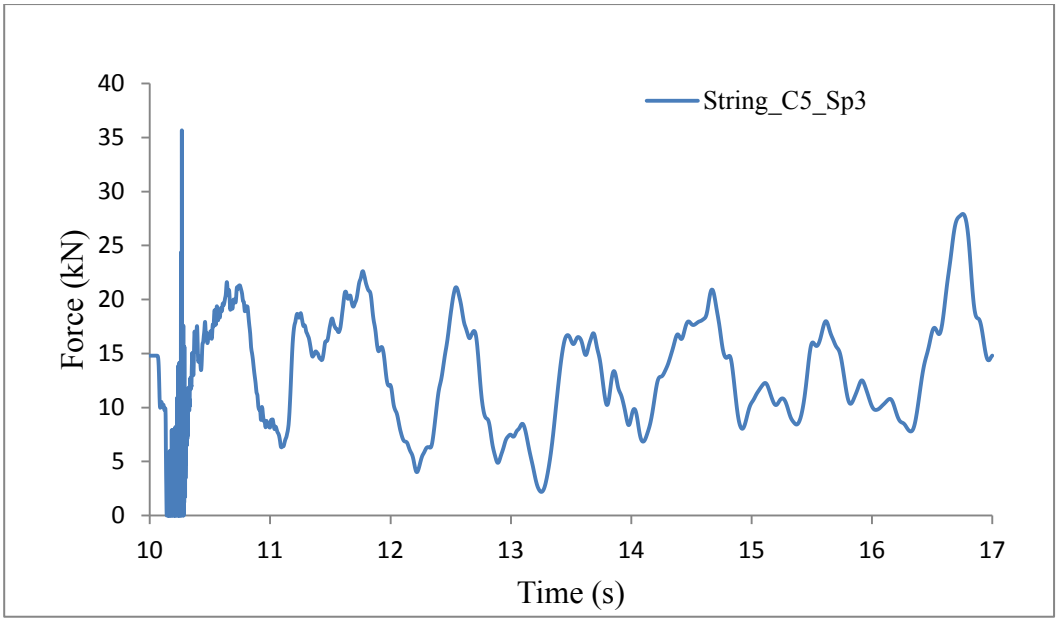

Figure 5.16 Tension at String_C5_Sp3

Cable rupture is investigated by seven different scenarios

To investigate the effects of different types of cable rupture assumptions and time steps, seven scenarios are studied in this section. In these scenarios four types of rupture assumptions are used: 1) all cable elements are omitted at once in the ruptured conductor span, 2) one cable element is omitted at the left side of the ruptured conductor span, 3) one cable element is omitted at middle of the ruptured conductor span, and 4) one cable element is omitted at the right side of ruptured conductor span. In addition, for each of these three rupture locations, two time step approaches are compared: one with the original time step of 1.5 ms, and the other with a smaller time step of 0.15 ms during the first second of dynamic analysis. Two response indicators are used to compare these scenarios: tension at String_C3_Sp5 and String_C5_Sp3.

Figure 5.17 to Figure 5.23 show that eliminating just one cable element instead of omitting all cable elements in a ruptured span improves the simulated tension time history plots and filters out most of the unwanted high frequencies. Moreover, implementing smaller time steps in the initial phase of the response has clear beneficial effects and leads to smoother plots and less spurious high frequencies. The best results are obtained for the 3rd (Figure 5.19) and 5th (Figure 5.21) scenarios. It should also be mentioned that in the 2nd scenario the analysis stopped after 5.2 s due to lack of convergence. However, the results obtained before that time were reasonable.

Despite the improved results obtained in the suspension string tensions, the accelerations in the ruptured conductors in all scenarios remained in the same range as before therefore improvement in this regard will require further investigations. To limit the amount of graphs presented in this chapter the corresponding acceleration plots are not presented.

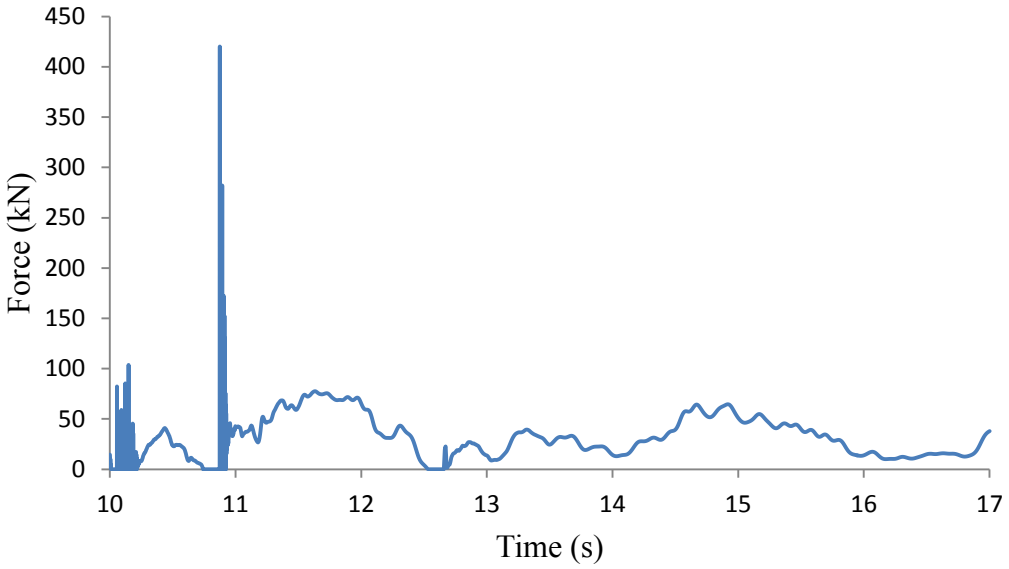

a) Cable tension at String_C3_Sp5

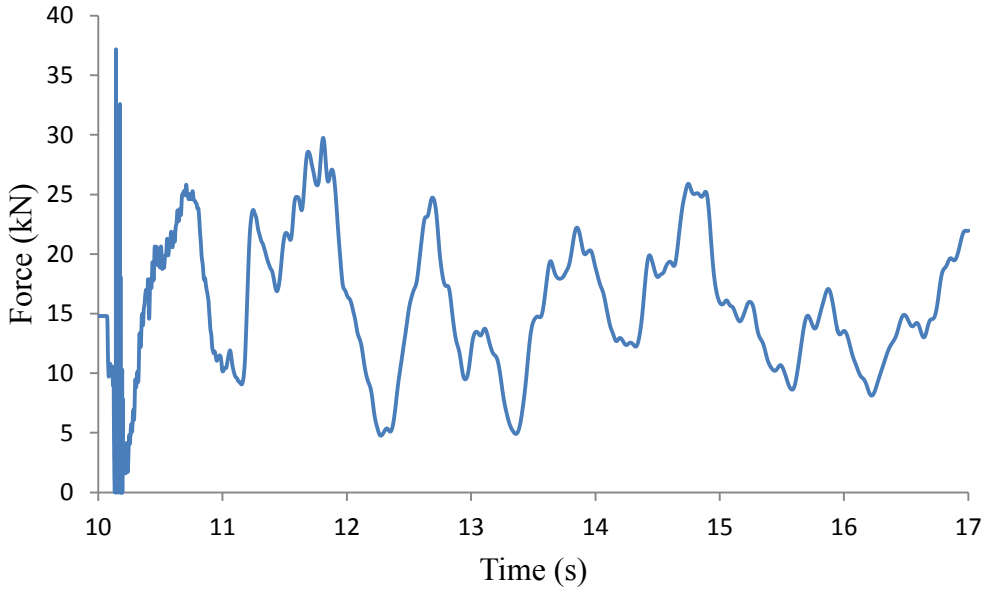

b) Cable tension at String_C5_Sp3

Figure 5.17 1st scenario: all elements omitted at once in ruptured conductor spans with smaller time steps

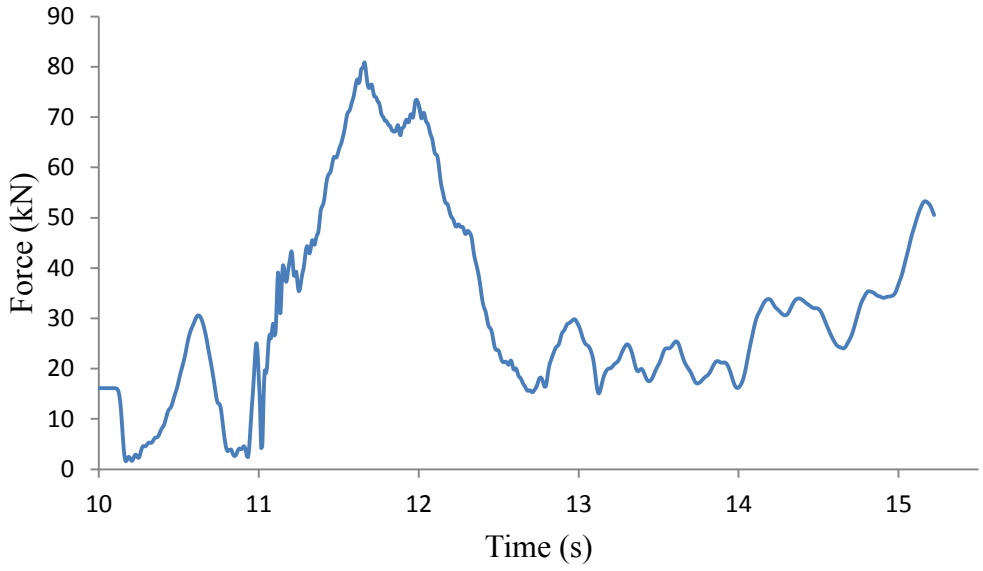

a) Cable tension at String_C3_Sp5

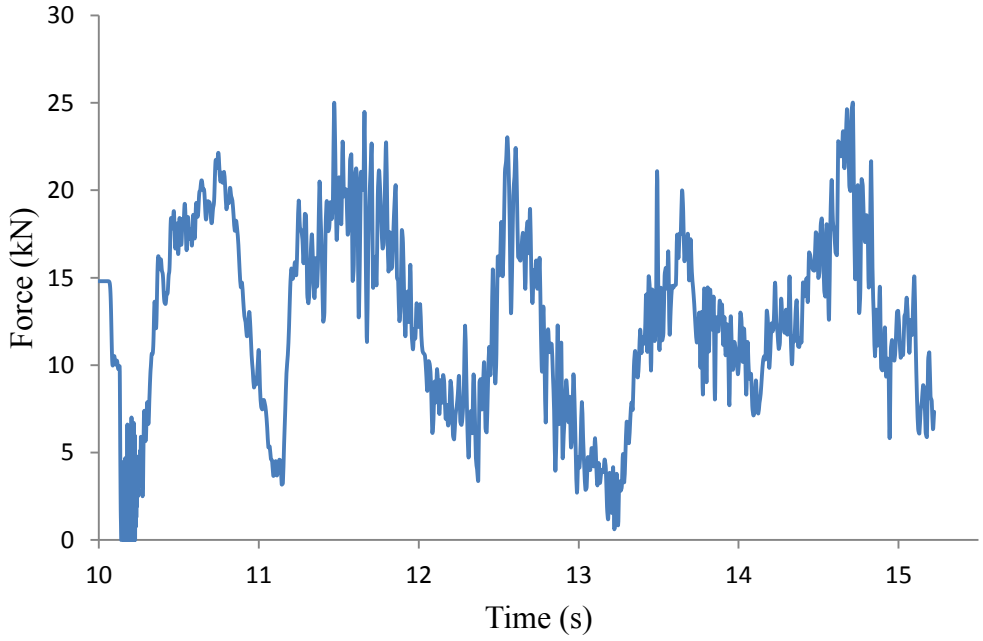

b) Cable tension at String_C5_Sp3

Figure 5.18 2nd scenario: one element omitted at the left side of the ruptured conductor span with original time steps

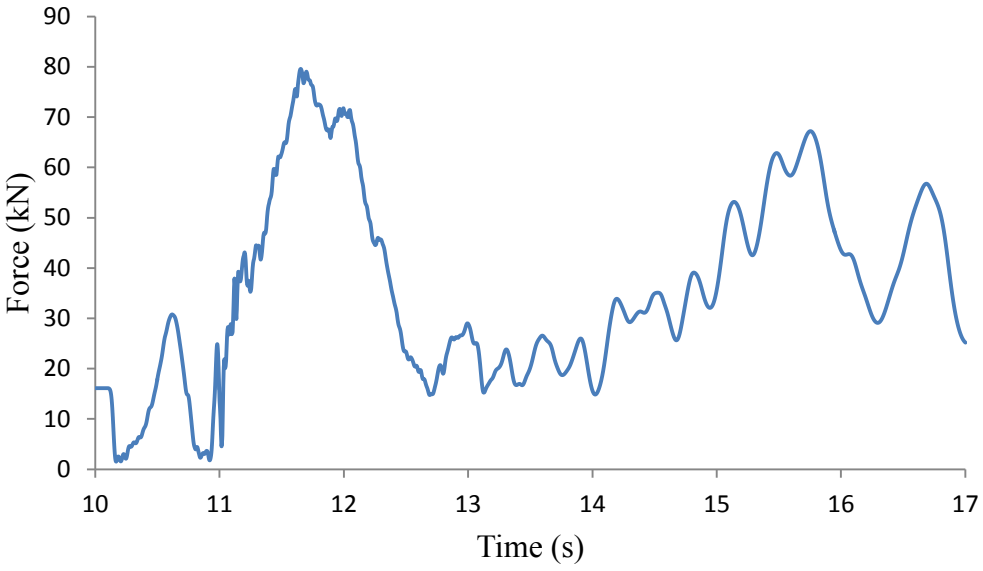

a) Cable tension at String_C3_Sp5

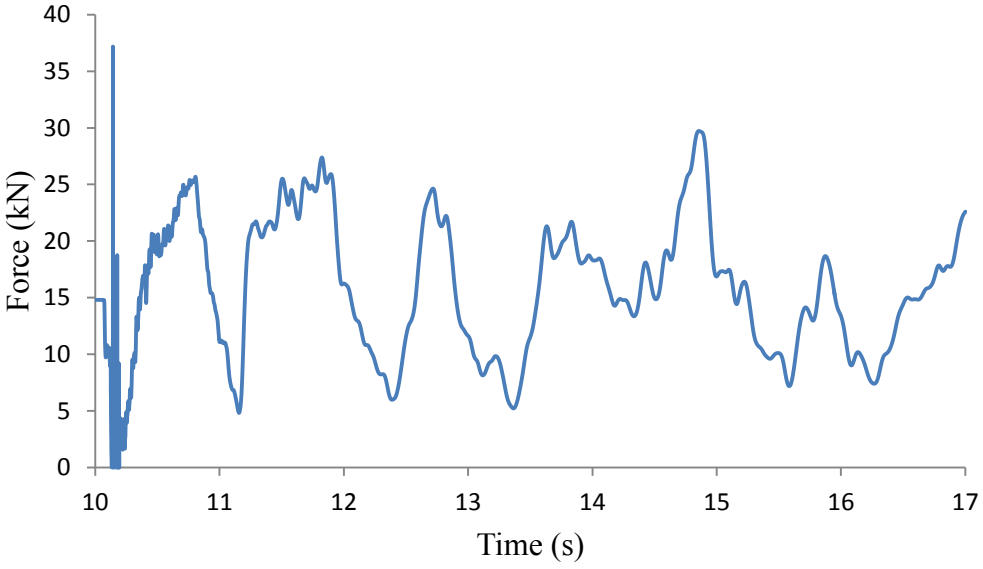

b) Cable tension at String_C5_Sp3

Figure 5.19 3rd scenario: one element omitted at the left side of the ruptured conductor span with smaller time steps

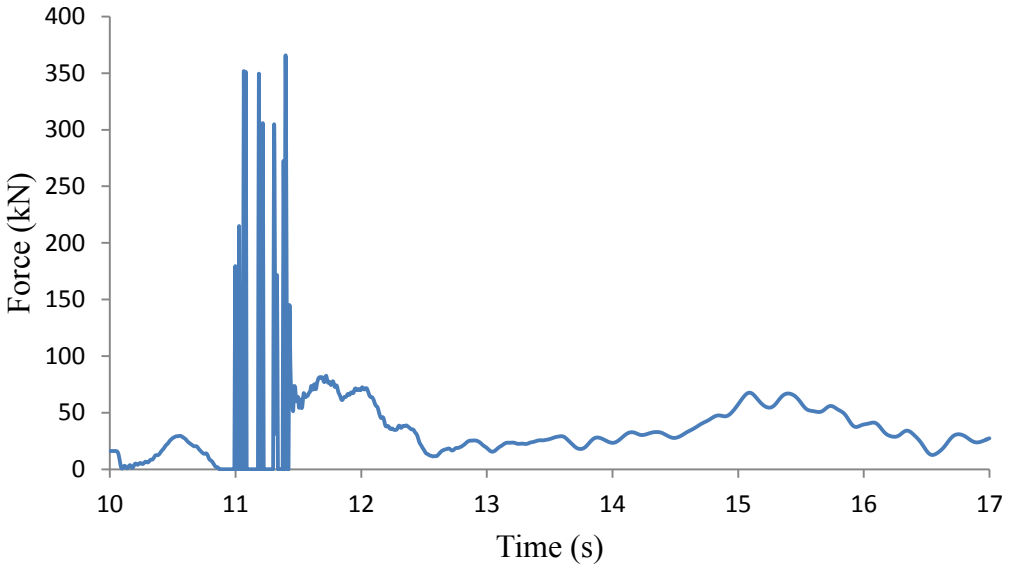

a) Cable tension at String_C3_Sp5

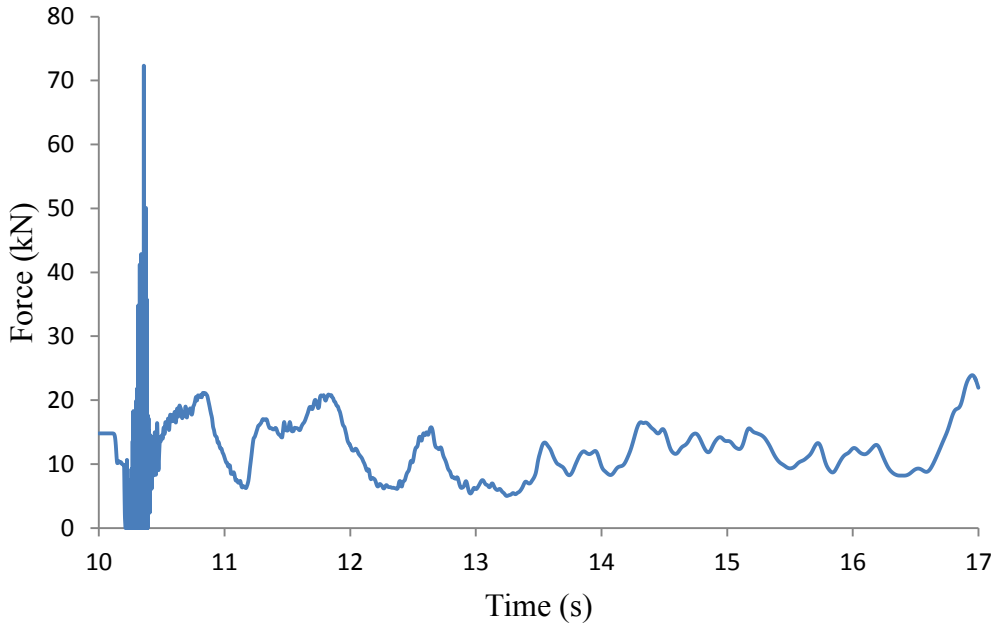

b) Cable tension at String_C5_Sp3

Figure 5.20 4th scenario: one element omitted at the middle of the ruptured conductor span with original time steps

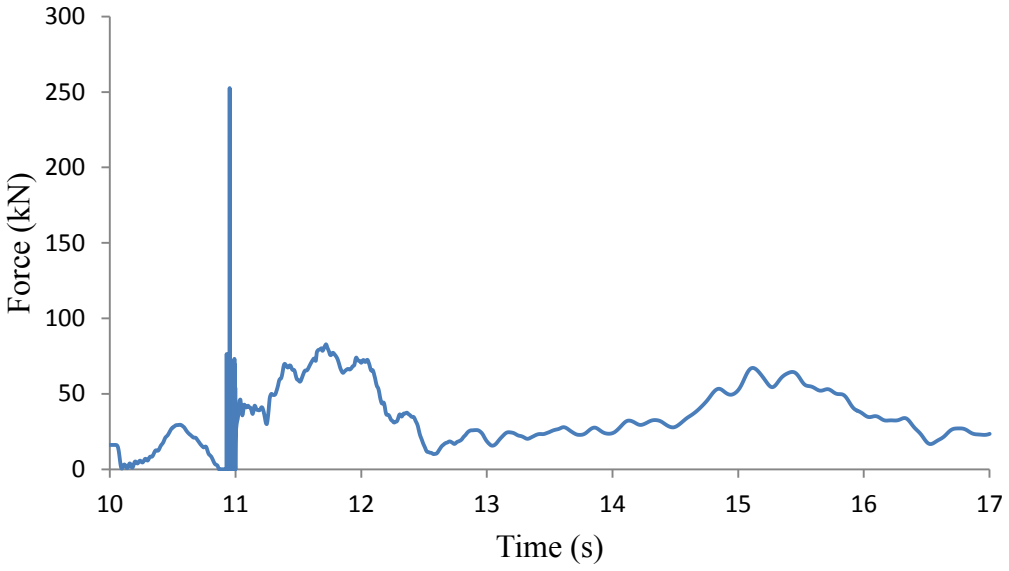

a) Cable tension at String_C3_Sp5

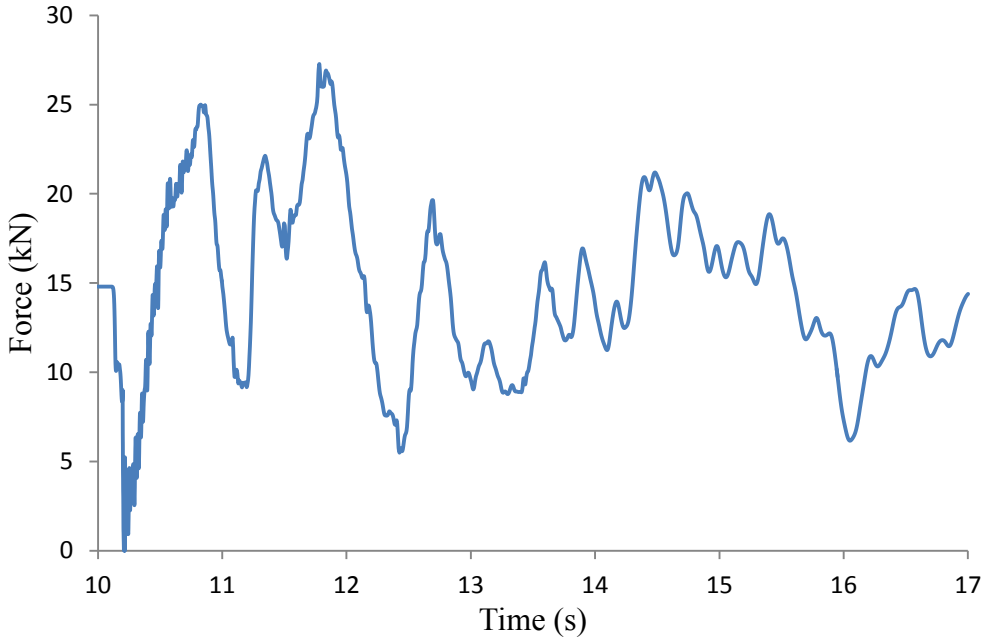

b) Cable tension at String_C5_Sp3

Figure 5.21 5th scenario: one element omitted at the middle of the ruptured conductor span with smaller time steps

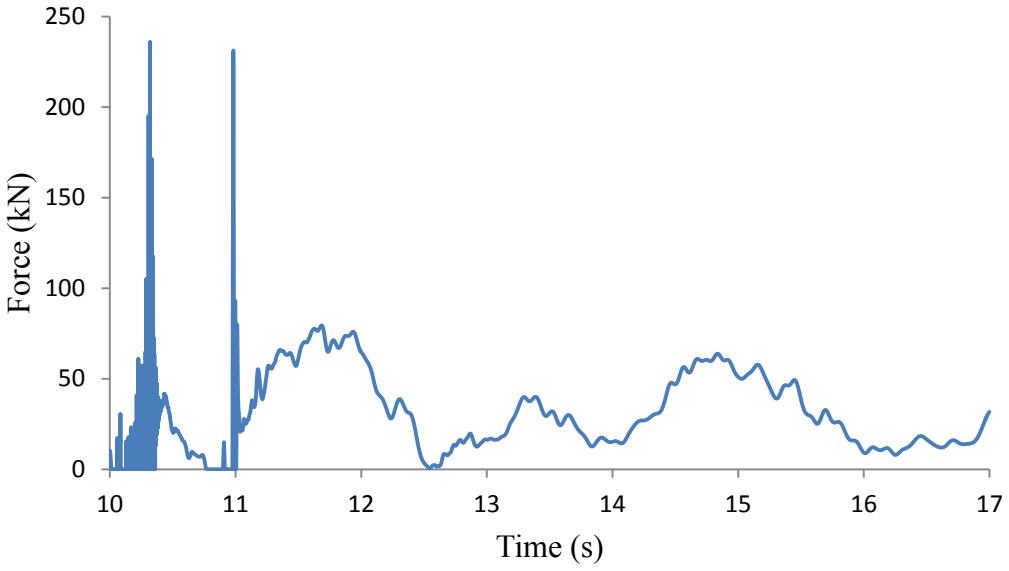

a) Cable tension at String_C3_Sp5

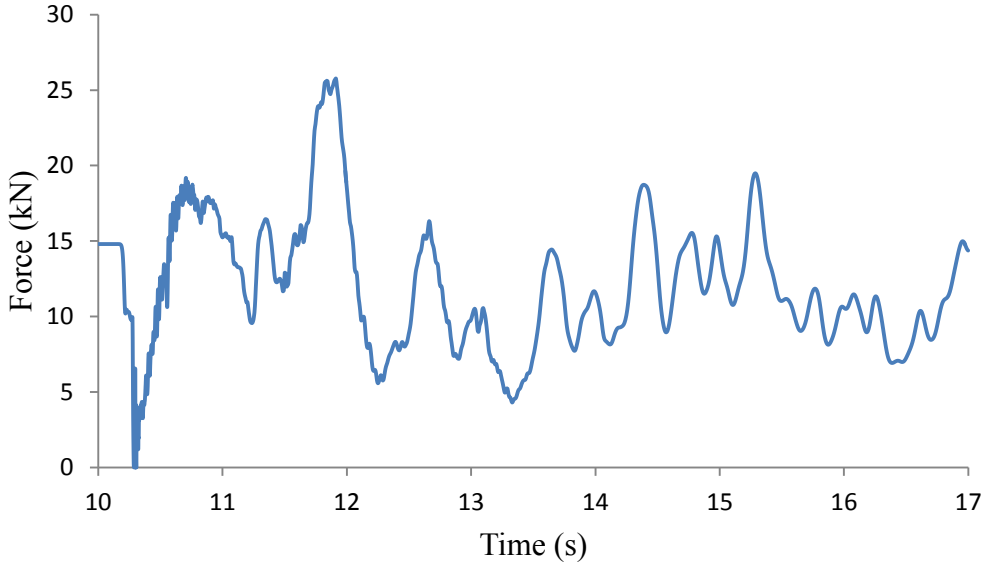

b) Cable tension at String_C5_Sp3

Figure 5.22 6th scenario: one element omitted at the right side of the ruptured conductor span with original time steps

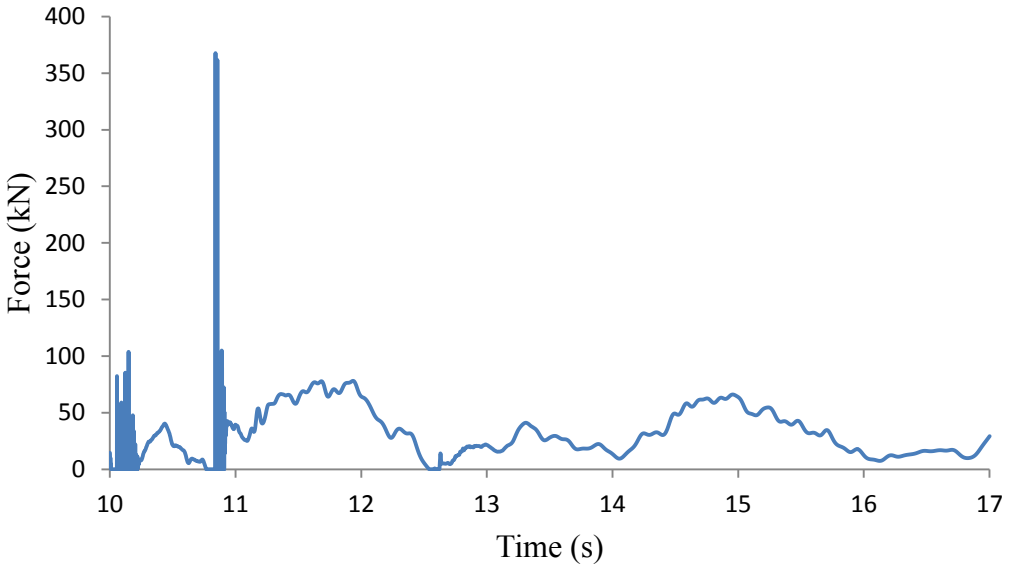

a) Cable tension at String_C3_Sp5

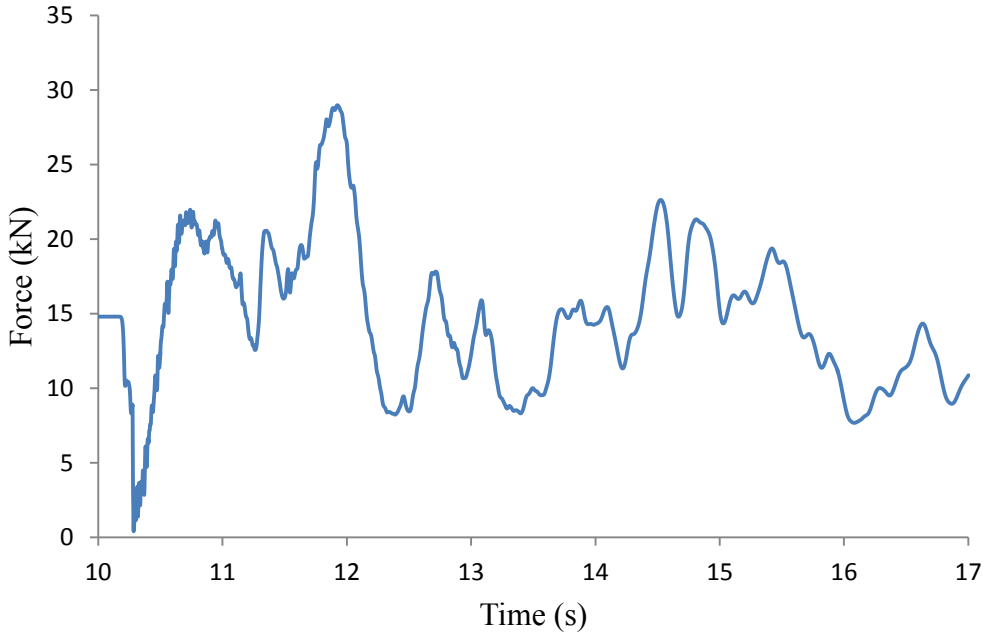

b) Cable tension at String_C5_Sp3

Figure 5.23 7th scenario: one element omitted at the right side of the ruptured conductor span with smaller time steps

5.5 Conclusion

This study shows the feasibility of implementing the new ice shedding criterion based on maximum effective plastic strain in complex transmission line section models. Moreover, considering ice shedding in the iced spans subjected to cable rupture is essential and influences the general dynamic response of the line. Overall, the results indicate that ice shedding following cable rupture tends to attenuate the dynamic response of the damaged line section in comparison to the results obtained by Lapointe (2003) where ice shedding was not modelled.

It was shown that ice shedding observed in the model was due to large accelerations (and resulting inertia forces) in the ice-beam elements. However the issue of over predicting these accelerations in the numerical models has not been completely resolved. However, encouraging results have been obtained to eliminate some spurious high frequency peaks observed in the time history of insulator string tensions, by using smaller time steps in the initial phase of the dynamic analysis and by changing the actual location of the conductor rupture, i.e. by omitting one element at the left side or the middle of the ruptured conductor span instead of omitting all the conductor elements at once.

More in-depth studies could be conducted with this application, namely by expanding the modelling of ice shedding to more spans with ice-beam elements.

6. Conclusion

6.1 General Conclusions

This research addressed the accurate numerical modelling of ice shedding phenomena in overhead transmission lines, when ice deposits on conductors are detached from the cable following an initial trigger such as a controlled shock load applied locally with a cable de-icing device, or uncontrolled shocks due to cable rupture. Accurate modelling of ice rupture before shedding then allowed the study its dynamic effects on line sections

First, an improved failure criterion for cylindrical glaze ice deposits was proposed and validated with experimental results obtained by Kálmán (2007) at CIGELE Laboratory of Université du Québec at Chicoutimi. The experiment consisted of accumulating glaze ice on a reduced-scale (4-m) single span of flexible metallic cable and then monitoring its response to the application of a shock load at mid span. The proposed ice deposit rupture criterion is based on maximum effective plastic strain. The study shows that it yields more realistic predictions of ice fracture rates than a previous criterion derived by Kálmán on the basis of maximum bending stress.

Following the successful application of the new ice failure criterion based on maximum effective plastic strain on the reduced scale model, the same modelling approach was applied to a single-span of 300 m of real overhead conductor. Also, an optimum mesh size to model ice deposits at the real scale was determined with a view to retain accuracy and significantly reduce the computational effort in a complex transmission line model with iced conductors.

Finally, the new ice shedding criterion was applied to a three-dimensional model of a real multi-span transmission line section that experienced conductor ruptures during an ice storm in 1997. It was confirmed that considering ice shedding in the iced spans adjacent to ruptured conductors is essential because these spans are forced to completely shed the ice after the failure shock, which influences the general dynamic response of the line. Moreover, it was shown that ice shedding observed in the model was due to the large pulse accelerations induced in the ice deposits. Overall, the results indicated that ice shedding following cable rupture tends to attenuate the dynamic response of the damaged line section in comparison to the results obtained by Lapointe (2003) where the dynamic effects of cable failure were modelled without the possibility of ice shedding.

6.2 Model limitations and suggestions for future work

The improvement in failure criterion for glaze ice deposits based on the maximum effective plastic strain is the first step in the implementation of a two-tier ice rupture criterion that will also consider the adhesive strength of the fractured deposits to model ice shedding phenomenon more properly. In fact, when the strain criterion is fulfilled at any integration point and the ice element is fully cracked, the net vertical inertia force applying on the element (including self weight) should overcome the adhesive strength between ice and cable to make ice shedding happen. To do so the second criterion should also be satisfied:

Vertical inertia force > Adhesive strength

Incorporating the adhesive strength criterion to the finite element model can be done by using lumped elements (spring elements) with prescribed maximum strength.

Currently, there is an ongoing research effort on this issue at CIGELE laboratory and further adhesive strength modeling developments will be the submit of future joint work at McGill and UQAC.

Also, as it was mentioned in Chapter 3 the proposed ice failure criterion is based on pure bending calculations. However, in reality the ice deposit is highly stressed in the axial direction due to its compatibility of axial displacements with the conductor and the strain rupture criterion will be checked with the combined axial and bending effects in the ice beam. Therefore, to have a more accurate analytical model of strain criterion one should consider both axial and bending portions of induced strain in the ice beams to set the strain limit. In addition, Gauss integration points have been used as the numerical integration method in this study and since the assumed iced cross section has a rectangular shape its integration points are located inside the cross section. However, the maximum strain due to axial and bending effects happens at the far most fibers of the cross section so it is recommended to use Newton-Cotes integration method instead where the integration points are located on the sides. Moreover, as this study deals with large kinematic motions, isoparametric beam elements with rectangular cross section have been used to model ice deposits since only rectangular cross sections can be considered for the materially nonlinear isoparametric beam elements in ADINA. However, one can try to model ice chunks by using Hermitian beam elements with pipe cross section but this may lead to shear locking problems in large kinematic motions.

In the iced line sections expanding the modelling of ice shedding to more intact and ruptured spans with ice-beam elements will help to capture the dynamic response of the line components more accurately.

The time histories of node accelerations have spurious high frequencies and are over predicted. Defining another type of damper, considering a different damping ratio or changing the parameters δ and α in the Newmark integration method could filter out spurious high frequencies of the response and resolve the problem associated with high accelerations in the numerical models.

Finally, the reduced-scale model possesses a high degree of sensitivity to the flexibility of the cable in use which does not exist in the real-scale line conductors. Unfortunately, no experimental results were available from full-scale test spans to verify cable acceleration predictions following shock loads.

References

ADINA R&D Inc. 2008. *ADINA Theory and Modeling Guide*, Watertown, MA, USA.

Baenziger, M. 1981. *Broken conductor loads on transmission line structures*. Ph.D. thesis, University of Wisconsin, Madison, Wisconsin.

Bathe, K.J. 2006. *Finite element procedures*, Prentice Hall, Upper Saddle River, NJ, USA.

CIGRE. 2006. 291, *Guidelines for meteorological icing models, Statistical methods and topographical effects*, Working Group B2.16, Task Force 03.

Commission scientifique et technique [Ice Storm 98, Nicolet Commission]. 1999. *Les aspects structuraux du réseau d'Hydro-Québec, chap. In Les conditions climatiques et l'approvisionnement en énergie*, Sector-based studies, vol. 3, book 2, chap. 1. Les Publications du Québec.

Druez, J., Nguyen, D.D., and Lavoie, Y. 1986. Mechanical properties of atmospheric ice. *Cold Regions Science and Technology*, 13(1): 67-74

Druez, J., Phan, C.L., Laforte, J.L., and Nguyen, D.D. 1979. The adhesion of glaze and rime on aluminum electrical conductors. Trans. *CESM*, 5: 215-220

Gow, A.J., and Ueda, H.T. 1989. Structure and temperature dependence of the flexural properties of laboratory freshwater ice sheets, *Cold Regions Science and* Technology, 16: 249-269.

Hawkes, I. and Mellor, M. 1972. Deformation and fracture of ice under uniaxial stress. *Journal of Glaciology*, 11 (61), 103–131.

Huschke R.E. 1959. *Glossary of meteorology*, Boston, MA, USA: American Meteorological Society.

Irvine H.M. *Cable structures*, Cambridge, MA, USA : MIT Press, 1981.

Jamaleddine, A., McClure, G., Rousselet, J., and Beauchemin, R. 1993. Simulation of Ice Shedding on Electrical Transmission Lines Using ADINA. *Computers and Structures,* 47(4/5):523-536.

Javan-Mashmool, M. 2005. *Theorical and Experimental investigations for measuring interfacial bonding strengh between ice and substrate*. maîtrise en ingénierie, UQAC.

Javan-Mashmool, M., Volat, C., and Farzaneh, M. 2006. A new method for measuring ice adhesion strength at an ice-substrate interface. *Hydrological Processes*, 20(4): **6**45-655

Jones, S.J. 1982. The confined compressive strength of polycrystalline ice. *Journal of Glaciology* 28 (98), 171–177.

Kálmán, T. 2007. *Dynamic Behaviour of Iced Cables Subjected to Mechanical Shocks*. Ph.D. Thesis, Faculty of Applied Sciences, Université du Québec at Chicoutimi, Canada.

Kálmán, T., Farzaneh, M., and McClure, G. 2007. Numerical analysis of the dynamic effects of shock-load-induced ice shedding on overhead ground wires. *Computers and Structures,* 85:375-384.

Kálmán, T., Farzaneh, M., McClure, G., Kollar, L.E., and Leblond, A. 2005. Dynamic behaviour of iced overhead cables subjected to mechanical shocks. *Proceedings of the 6th International Symposium on Cable Dynamics*, September 2005, AIM, Charleston, SC, USA, 339–346.

Kermani, M. 2007. *Ice shedding from cables and conductors*. Ph.D. Thesis, Faculty of Applied Sciences, Université du Québec at Chicoutimi, Canada.

Kermani, M., Farzaneh, M., and Gagnon, R.E. 2007. Compressive strength of atmospheric ice. *Cold Regions Science and Technology*, vol. 49, pp. 195-205.

Kermani, M., Farzaneh, M., and Gagnon, R.E. 2008. Bending Strength and Effective Modulus of Atmospheric Ice. *Cold Regions Science and Technology*, vol. 53, no. 2, 2008, pp. 162-169.

Lapoint, M. 2003. *Dynamic analysis of a power line subjected to longitudinal loads. Master*. Thesis, Department of Civil Engineering and Applied Mechanics, McGill University, Canada.

Leblond, A., Lamarche, B., Bouchard, D., Panaroni, B. and Hamel, M. 2005. Development of a portable de-icing device for overhead ground wires, *Proceedings of the 11th International Workshop on Atmospheric Icing of Structures*, Montreal, Canada, 399-404.

Leblond, A., Montambault, S., St-Louis, M., Beauchemin, R., Laforte, J-L. and Allaire, MA. 2002. Development of new ground wire de-icing methods, *Proceedings of the 10th International Workshop on Atmospheric Icing of Structures*, Brno, Czech Republic, 9-6.

Lima and Amil. 2006. *Centrifugal adhesion test data sheet*. Report #: 2006-CAT-02, Test#: CAT17, Université du Québec à Chicoutimi.

Main, I.G. 1978. *Vibrations and waves in physics*, Cambridge, UK: Cambridge University Press.

McClure, G. 1989. *Interactions dynamiques dans les lignes aériennes de transport d'électricité soumises aux bris de câbles*. Ph.D. thesis, École Polytechnique, University of Montreal, Montreal.

McClure, G., and Guevara, E.I. 1994. Seismic behaviour of tall guyed telecommunication towers. *Proceedings of the IASS-ASCE International Symposium 1994*, Atlanta, Georgia, 24-28 April, 259-268.

McClure, G., and Lapointe, M. 2002. Computing electric power line response to exceptional dynamic loads. The Ninth International Conference on Computing in Civil and Building Engineering, Taipei, Taiwan, 3-5 April, 345-348.

McClure, G., and Lapointe, M. 2003. Modeling the structural dynamic response of overhead transmission lines. *Computers and Structures*, 81:825–834.

McClure, G., and Tinawi, R. 1987. Mathematical modeling of the transient response of electric transmission lines due to conductor breakage. *Computers and Structures*, 26(1/2):41–56.

McClure, G., and Tinawi, R. 1989. Comportement dynamique des lignes aériennes de transport d'électricité dû aux bris de câbles. I. Modélisation mathématique (Dynamic behaviour of aerial power lines subjected to cable breakages Part I. Mathematical modelling), Canadian Journal of Civil Engineering, 16(3): 335-353.

McClure, G., and Tinawi, R. 1989. Comportement dynamique des lignes aériennes de transport d'électricité dû aux bris de câbles. II. Problèmes numériques associés à la modélisation mathématique (Dynamic behaviour of aerial power lines subjected to cable breakages Part II. Numerical difficulties related to the mathematical modelling), Canadian Journal of Civil Engineering, 16(3): 354-374.

McClure, G., and Tinawi, R. 1991. Nonlinear transient dynamic behaviour of electric transmission lines subjected to cable breakage. Proceedings of the 1991 CSCE Annual Conference, Vancouver, 28-31 May, Vol. II, 72-81.

Peabody, A.B. 2001. Transmission Line Longitudinal Loads – A Review of Design Philosophy. *Structural Engineering Series No*. 2001-02, McGill University, Montreal.

Peabody, A.B. 2004. *Applying shock damping to the problem of transmission line cascades*. Ph.D. thesis, Department of Civil Engineering and applied Mechanics, McGill University, Montreal, Canada.

Petrenko, V.F. and Whitworth, RW. 1999. *Physics of Ice*. Oxford University Press: Oxford.

Poots G. 1996. *Ice and snow accretion on structures*, Taunton, Somerset, England: Research Studies Press.

Raraty, L.E., and Tabor, D. 1958. The Adhesion and Strength Properties of Ice. *Proceedings of the Royal Society of London. Series A, Mathematical and Physical Sciences*, 245(1241): 184-201.

Roshan Fekr, M., and McClure, G. 1998. Numerical Modeling of the Dynamic Response of Ice Shedding on Electrical Transmission lines. *Atmospheric Research,* 46: 1-11.

Sayward J.M. 1979. *Seeking low ice adhesion*. Special Report AD-A071-040, US Army Regions Research and Engineering Laboratory, Hanover, NH.

Schulson, E.M. 1990. The brittle compressive fracture of ice. *Acta Metallurgica et Materialia* 38 (10), 1963–1976.

Schulson, E.M. and Canon, N.P. 1984. The effect of grain size on the compressive strength of ice. *IAHR Ice Symposium*, Hamburg, pp. 109–117.

Timco, G.W., and Frederking, R.M.W. 1982 Comparative strength of fresh water ice, *Cold Regions Science and Technology*, 6: 21-27.

Volat, C., Farzaneh, M. and Leblond, A. 2005. De-icing/anti-icing techniques for power lines: current methods and future direction. *Proceedings of the 11th International Workshop on Atmospheric Icing of Structures*, Montreal, Canada, 323-333.

APPENDIX A - Cable tension, displacement and acceleration graphs

Time history results of some response indicators from section 4.2 are presented in Figure A.1 to Figure A.5. The following indicators are shown: Cable tension at mid span and at support, displacement at mid span, vertical acceleration at mid span and quarter point.

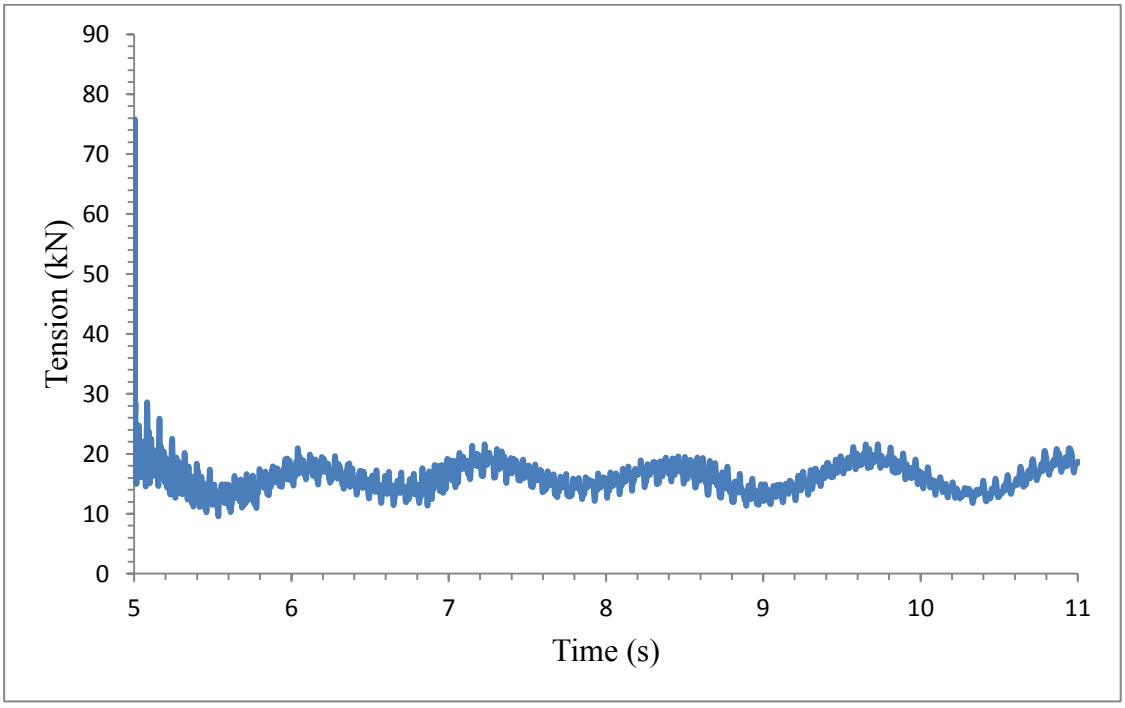

Figure A.1 Cable tension at the mid span

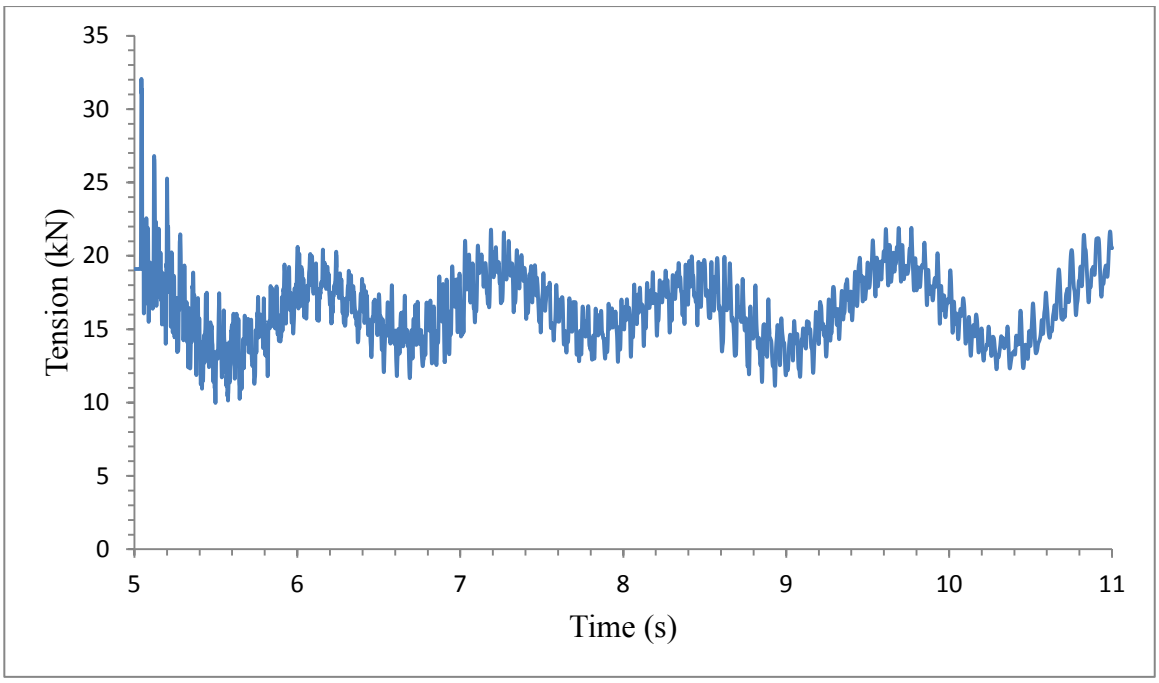

Figure A.2 Cable tension at the support

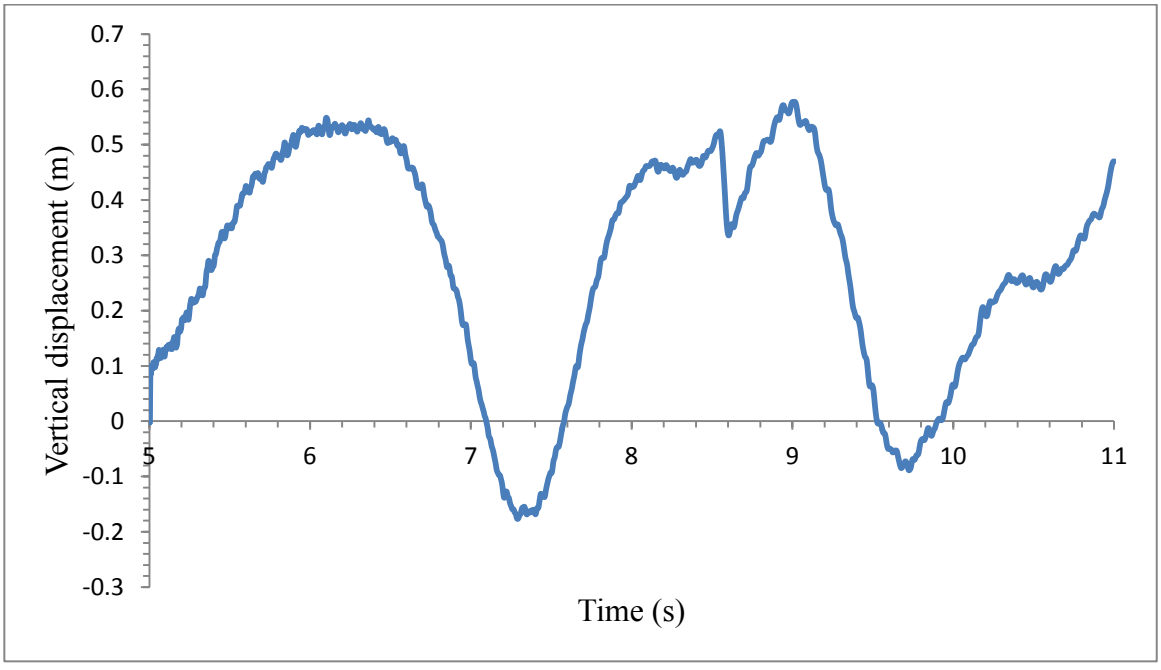

Figure A.3 Cable displacement at mid span

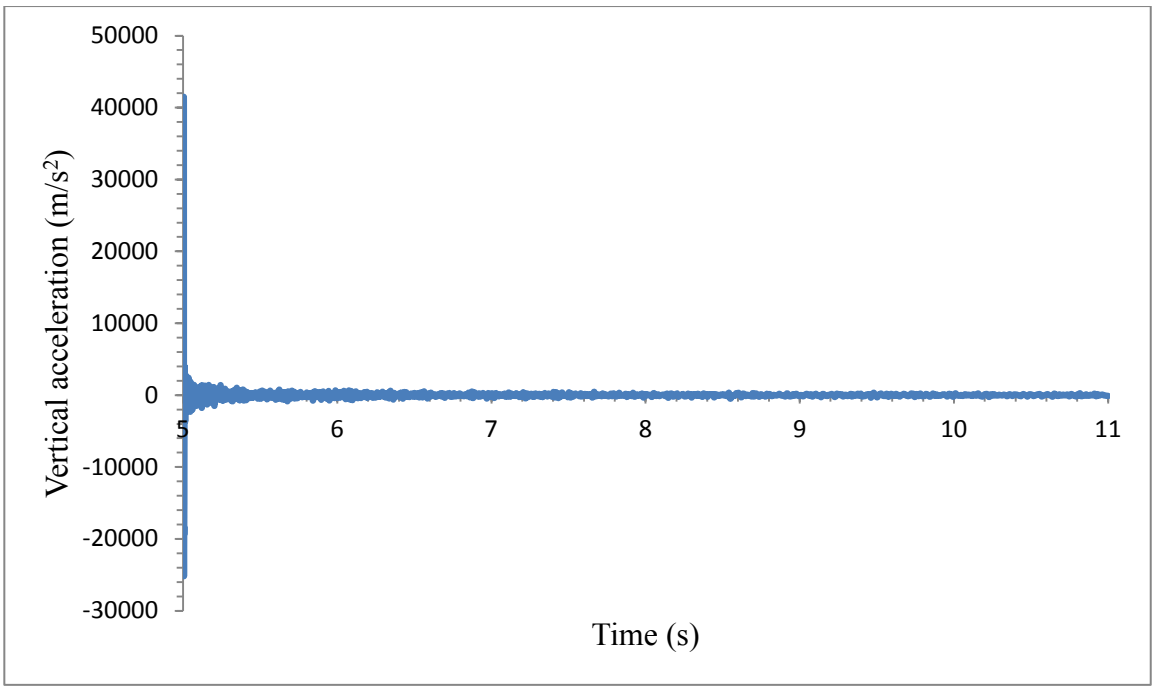

Figure A.4 Vertical acceleration at mid span

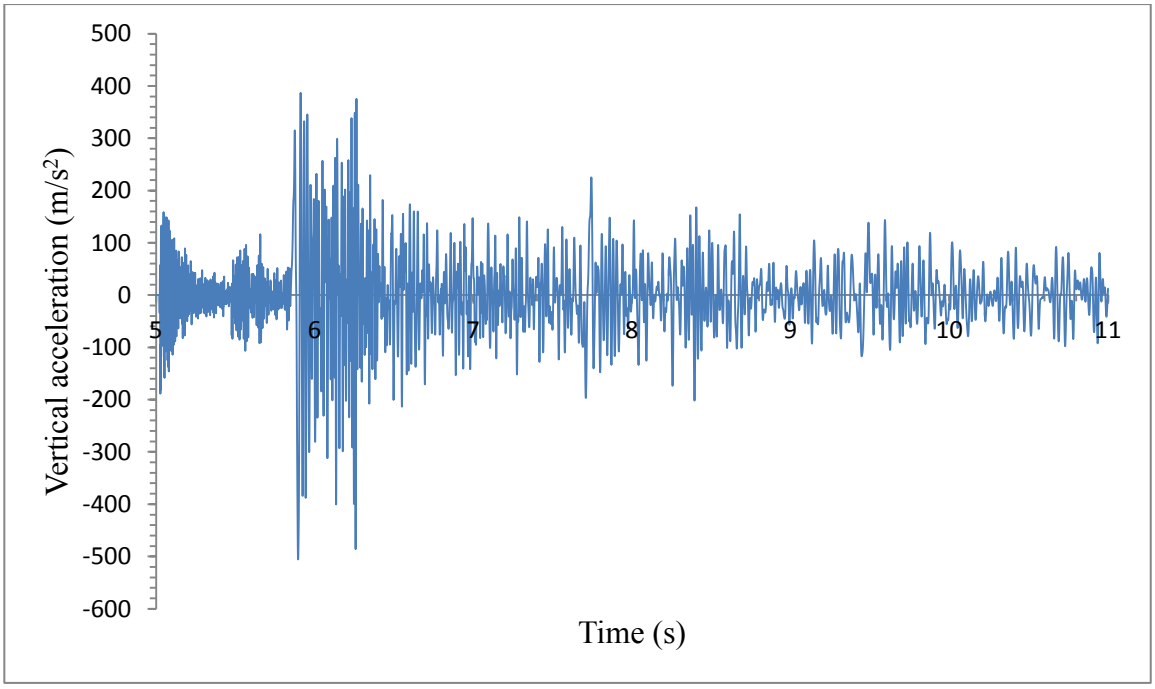

Figure A.5 Vertical acceleration at quarter span

APPENDIX B – Photographs of damaged line section in Chapter 5

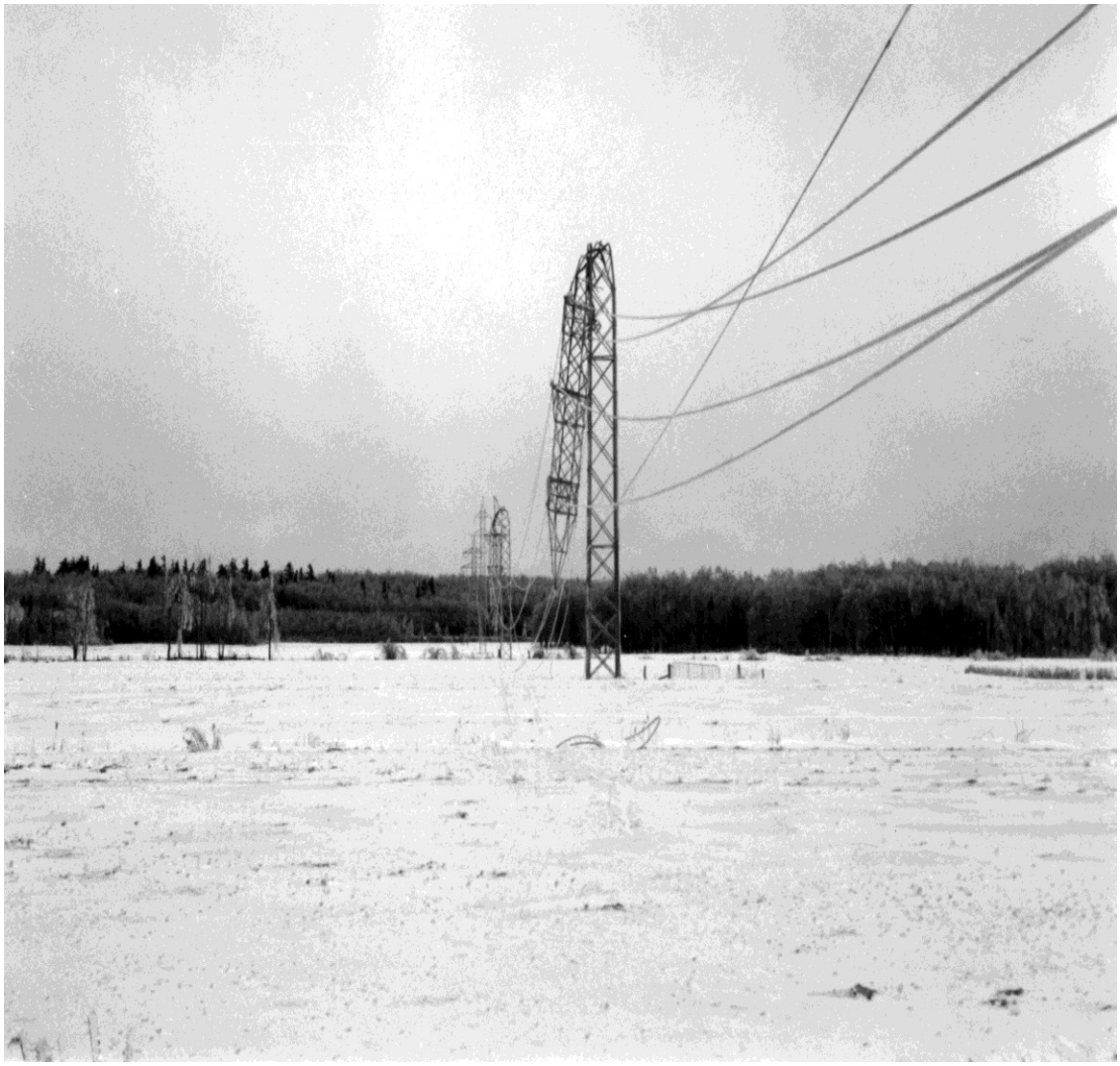

Figure B.1 Overall view of the line section failure with two rupture conductors (Source: Hydro-Québec)

Figure B.2 Close-up view of damage at suspension tower#3 (Source: Hydro-Québec)

Figure B.3 Close-up view of damage at suspension tower#4 (Source: Hydro-Québec)